

MATHEMATICAL MODELING OF WAVE-CURRENT INTERACTIONS IN
MARINE CURRENT TURBINES

by

Amit J. Singh

A Thesis Submitted to the Faculty of
The College of Engineering and Computer Science
in Partial Fulfillment of the Requirements for the Degree of
Master of Science

Florida Atlantic University

Boca Raton, Florida

May 2012

UMI Number: 1517858

All rights reserved

INFORMATION TO ALL USERS

The quality of this reproduction is dependent on the quality of the copy submitted.

In the unlikely event that the author did not send a complete manuscript and there are missing pages, these will be noted. Also, if material had to be removed, a note will indicate the deletion.



UMI 1517858

Copyright 2012 by ProQuest LLC.

All rights reserved. This edition of the work is protected against unauthorized copying under Title 17, United States Code.



ProQuest LLC.
789 East Eisenhower Parkway
P.O. Box 1346
Ann Arbor, MI 48106 - 1346

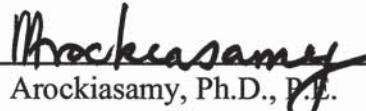
MATHEMATICAL MODELING OF WAVE-CURRENT INTERACTIONS IN
MARINE CURRENT TURBINES

by


Amit J. Singh


This thesis was prepared under the direction of the candidate's thesis advisor, Dr. Madasamy Arockiasamy, Department of Civil, Environmental and Geomatics Engineering, and has been approved by the members of his supervisory committee. It was submitted to the faculty of the College of Engineering and Computer Science and was accepted in partial fulfillment of the requirements for the degree of Master of Science.

SUPERVISORY COMMITTEE:

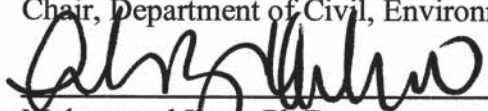

M. Arockiasamy, Ph.D., P.E.
Thesis Advisor

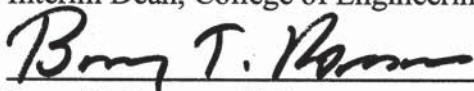

Howard P. Hanson, Ph.D.

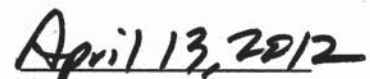

Chaouki Ghemai, Ph.D.


Yan Yong, Ph.D.


Panagiotis D. Scarlatos, Ph.D.
Chair, Department of Civil, Environmental and Geomatics Engineering


Mohammad Ilyas, Ph.D.
Interim Dean, College of Engineering and Computer Science


Barry T. Rosson, Ph.D.
Dean, Graduate College


Date

ACKNOWLEDGEMENTS

The work presented herein has been supported financially by the Southeast National Marine Renewable Energy Center (SNMREC) and the author gratefully acknowledges the support. The author would like to thank Susan Skemp, Executive Director, and Dr. H.P. Hanson, Scientific Director for the constant encouragement.

The author wishes to express his sincere thanks to his thesis advisor Dr. M. Arockiasamy, Professor and Director, Center for Infrastructure and Constructed Facilities, Department of Civil, Environmental, and Geomatics Engineering, for his excellent guidance, suggestions, and constant review in all stages throughout the course of this work. Grateful acknowledgements are due to Dr. Yan Yong and Dr. Chaouki Ghenai for their interest, encouragement, and manuscript review. The author expresses sincere appreciation to Ben Oliver, Lin, and Rammone Bartlett from the Department of Ocean and Mechanical Engineering for their graceful assistance in using the ANSYS software.

Finally, I am most grateful for the support, affection, and encouragement from my parents, family and friends throughout the course of the research.

ABSTRACT

Author: Amit J. Singh

Title: Mathematical Modeling of Wave-Current Interactions in Marine Current Turbines.

Institution: Florida Atlantic University

Thesis Advisor: Dr. M. Arockiasamy

Degree: Master of Science

Year: 2012

The concept of marine current turbines was developed by Peter Fraenkel in the early 1970s. Ever since Fraenkel's efforts to modify and test the technology, several worldwide agencies have been exploiting the technology to retrofit the marine current turbine to their particular application. The marine current turbine has evolved from generating a few kilowatts to a few gigawatts. The present study focuses on a megawatt sized turbine to be located offshore the coast of Ft. Lauderdale, Florida. The turbine is to be placed in a similar location as a 20 kW test turbine developed by the Southeast National Marine Renewable Energy Center (SNMREC) at Florida Atlantic University, Dania Beach FL. Data obtained from the SNMREC is used in the mathematical model. ANSYS FLUENT is chosen as the CFD software to perform wave-current interaction simulation for the present study. The turbine is modeled in SolidWorks, then meshed in ANSYS ICEM CFD, then run in FLUENT. The results obtained are compared to

published work by scholarly articles from Fraenkel, Barltrop and many other well known marine energy researchers. The effects of wave height on the turbine operation are analyzed and the results are presented in the form of plots for tip speed ratio and current velocity.

MATHEMATICAL MODELING OF WAVE-CURRENT INTERACTIONS IN
MARINE CURRENT TURBINES

CHAPTER 1	1
1.1 Background.....	1
1.2 Scope of the Thesis	2
1.3 Environmental Impacts	3
1.4 Computational Fluid Dynamics (CFD) Analysis.....	4
1.5 Structure of the Report.....	6
CHAPTER 2	7
2.1 Introduction.....	7
2.1.1 Short Term and Long Term Effects on Wind Turbines	7
2.2 Marine Current Energy Resource	8
2.3 Power Extraction.....	12
2.3.1 Admiralty Inlet ocean current data analysis.....	13
2.3.2 Metaocean Data for Southeast Florida.....	16
2.4 Marine Current Extraction Technologies.....	21
2.5 Power from Marine Current Turbines.....	27
2.6 Rotor Blade Types	35
2.6.1 Axial Flow Rotor Blade Design.....	36
2.7 Hydrodynamics	37
2.7.1 Wind Turbine Operation Modeling Using CFD	37
2.7.2 Marine Turbine Operation Modeling Using CFD.....	41
2.7.3 Wave Current Interactions	41
CHAPTER 3	44
3.1 Introduction.....	44
3.2 Flow Characteristics.....	45
3.3 Computational Fluid Dynamics	47

3.4	Basics of Fluid Flow in ANSYS FLUENT.....	48
3.5	Multiphase Flow	49
3.5.1	The VOF Model.....	54
3.5.2	The Mixture Model.....	74
3.5.3	The Eulerian Model	74
3.6	The Finite Element Method	75
3.7	Blade Element Momentum Theory.....	76
3.8	Principles of Similitude.....	77
CHAPTER 4.....		78
4.1	Introduction.....	78
4.2	Physical Properties of Fluids.....	79
4.3	Fluid Flow in Marine Current Turbines	84
4.3.1	Compressible or Incompressible flow.....	85
4.3.2	Laminar and Turbulent Flow	86
4.4	Modeling the Rotor Blade and Hub using SolidWorks	87
4.5	Creation of Domain and all its Entities using ANSYS ICEM CFD.....	91
4.5.1	Blade Geometry Manipulation.....	91
4.5.2	Computational Fluid Domain.....	92
4.5.3	Multiphase Domain.....	93
4.6	Meshing the Domain and Blade.....	99
4.6.1	Mesh Type Selection.....	99
4.6.2	Multiphase Mesh Setup.....	100
4.7	CFD Simulation using ANSYS FLUENT	106
4.7.1	Multiphase Flow CFD.....	106
CHAPTER 5		109
5.1	Introduction.....	109
5.2	Mesh Verification and Grid Independence	110
5.3	Turbulence Study	111
5.4	Turbine Performance.....	112
5.4.1	Thrust Analysis	114
5.4.2	Torque	120
5.4.3	Power	125

5.4.4	Power Coefficient	128
5.4.5	Cavitation.....	130
CHAPTER 6		132
6.1	Summary	132
6.2	Conclusions.....	134
6.3	Future Work	135
REFERENCES		137

LIST OF FIGURES

Figure 1.1- A diagrammatic representation of the 20 kW turbine.....	3
Figure 2.1- Marine Currents in the Vicinity of the United States (University of Texas Libraries 2006).....	11
Figure 2.2- Visualization of two possible turbine and anchor technologies (Hammerfest Storm AS 2006; Gulfstream Energy Incorporated 2006).	13
Figure 2.3- Admiralty ocean current data collected at 14:02:32 08-Apr-2009 (Northwest National Marine Renewable Energy Center[NNMREC], University of Washington Branch: Tidal Energy).....	14
Figure 2.4 – The average current velocity profile for approximately twenty minutes of data collection. Intervals were chosen and data values were picked off of the above chart using the colored key for current velocity.....	15
Figure 2.5 - Raw velocity data showing current profile of the mean velocity with respect to ocean depth.....	18
Figure 2.6- Peak wave heights near the Southeast Florida region showing wave heights offshore the coast of Ft. Lauderdale and Miami. (NOAA National Weather Service).....	19
Figure 2.7- Peak wave periods near the Southeast Florida region showing the wave periods offshore the coast of Ft. Lauderdale and Miami. (NOAA National Weather Service).....	20

Figure 2.8- Model turbine during trials in the IFREMER tank.	22
Figure 2.9- IFREMER free surface hydrodynamic water tunnel located in Boulogne-sur-Mer, France.	23
Figure 2.10- Thrust coefficient comparison (theoretical and experimental data) at a mean speed of 0.79 m/s (Maganga et al., 2009).	24
Figure 2.11- Measured power for a homogeneous flow and a flow with a flow gradient (Maganga et al. , 2009).	25
Figure 2.12- Normalized thrust for turbulence intensity levels of 8% and 25% at a mid-depth location (Maganga et al., 2009).	26
Figure 2.13- Measured power for both turbulence intensity rates of 8% and 25% at a mid-span location (Maganga, et al., 2009).	27
Figure 2.14- Control volume for the idealized actuator-disk theory.	30
Figure 2.15- Actuator Disk Theory.	31
Figure 2.16- Power Coefficient for an ideal Betz model wind turbine.	33
Figure 2.17- Theoretical maximum power coefficient.	33
Figure 2.18- Typical turbine performance from real devices.	34
Figure 2.19- Two types of rotor blade configuration.	36
Figure 2.20- S809 Aerofoil section.	38
Figure 2.21- UAE turbine blade constructed in Rhinoceros CAD.	38
Figure 2.22- Measure Torque Output comparing the results between CFD and experiment.	39
Figure 2.23- Measured power output comparison between CFD and experiment.	40

Figure 2.24- Torque distribution calculated from the measured angular induction factor.	40
Figure 2.25- Thrust and Torque curves in still water at 200r/min.	42
Figure 2.26- Thrust and torque curves in $H = 150mm$ and $f = 0.50Hz$ at 150 r/min.	42
Figure 2.27- Effects of wave frequency on mean torque and thrust when rotor rotates at (a) 90 r/min and (b) 127 r/min.	43
Figure 3.1- Multiphase flow regimes available in ANSYS FLUENT (ANSYS, Inc., 2010).	52
Figure 4.1- CTD Instrument setup onboard the Ocean Power preparing to collect data for temperature and salinity (Leland, 2009, p. 32).	81
Figure 4.2- Temperature-depth plot from the data collected by the CTD instrument offshore the coast of Ft. Lauderdale, Florida.	82
Figure 4.3- Salinity-depth plot from the data collected by the SNMREC using the CTD instrument offshore the coast of Ft. Lauderdale, Florida.	83
Figure 4.4- Density profile computed using online calculator using salinity, temperature, and ocean depth data.	84
Figure 4.5- Comparison of average, maximum, and minimum current velocity profiles along the depth of the ocean offshore the coast of Ft. Lauderdale, FL.	85
Figure 4.6- Cross-sectional curves obtained from the National Renewable Energy Laboratory (NREL).	88
Figure 4.7- Completed blade formed from building lofted base from imported cross-sectional curves.	89
Figure 4.8 - Pitch angle of blade on model set at 15°	90

Figure 4.9- Completed rotor blade showing tri-blade setup connected to a center hub with face fillets.....	91
Figure 4.10- Repaired blade showing the location of curves only along the edges of the surfaces in the geometry	92
Figure 4.11- Repaired rotor blade in ICEM CFD showing the global y-axis (the axis of rotation of the turbine).....	93
Figure 4.12- Sketch showing the dimensions of the multiphase computational domain used in the model	94
Figure 4.13- Geometry layout of the full computational domain showing position of blade along the $y - axis$	95
Figure 4.14- Multiphase computational domain for “INLET.A” part setup.....	96
Figure 4.15- Multiphase computational domain for “INLET.W” part setup.....	96
Figure 4.16- Multiphase computational domain for “OUTLET.A” part setup.....	97
Figure 4.17- Multiphase computational domain for “OUTLET.W” part setup.....	97
Figure 4.18- Multiphase computational domain “SYMMETRY” part setup.....	97
Figure 4.19- Separate bodies created for the two phase computational domain: "BODY.A" (top) for the air phase and "BODY.W" (bottom) for the water phase.	98
Figure 4.20- Initial mesh quality used for simulation of the multiphase domain model.	102
Figure 4.21 - Delaunay mesh detail for multiphase setup.	104
Figure 5.1- Grid Independence Study Performed so as to obtain convergence of Thrust and Pressure on the Turbine.	110

Figure 5.2- Velocity Distribution along the Length of the Direction of Flow. The Turbine Plane of Rotation is Located at Position = 0.	112
Figure 5.3 - Marine Current Turbine Performance based on Rotor Diameter. (Fraenkel P. P., 2004).	114
Figure 5.4- Comparison of Simulated Thrust vs. Tip Speed Ratio.....	115
Figure 5.5 - Comparison of Simulated Thrust with Current Velocity.	116
Figure 5.6 - Thrust vs. Current Velocity in Still Water at 200 rpm. (Barltrop, Varyani, Grant, Clelland, & Pham, 2007).	117
Figure 5.7 - Thrust vs. Current Velocity in $H=0.15m$, $f=0.50Hz$, at 150 rpm. (Barltrop, et al., 2007).....	118
Figure 5.8 - Thrust Coefficient vs. Tip Speed Ratio comparing the Still Water Flow to Flow with Waves.	119
Figure 5.9- Thrust coefficient power moment. (Maganga, et al. , 2009).....	120
Figure 5.10 - Torque Generated vs. Tip Speed Ratio.	121
Figure 5.11 - Torque Generated vs. Current Velocity Comparing the Still Water Model to the Models with Waves.	122
Figure 5.12- Torque vs. Wave Height.	123
Figure 5.13 - Generated Torque based on Constant Frequency of (a) 0.625 Hz and (b) 0.833 Hz with Varying Wave Height. (Barltrop, et al., 2007).....	124
Figure 5.14 - Power vs. Current Velocity Comparing the Maximum Efficiency Values to the Current Model Data.	125
Figure 5.15- Power vs. Tip Speed Ratio showing Results from the Current Model and a Turbine of its Size at Maximum Efficiency.	127

Figure 5.16- Power Coefficient vs. Tip Speed Ratio.....	128
Figure 5.17 - Power Coefficient vs. Tip Speed Ratio. (Lee, et al., 2011).....	129
Figure 5.18 - Power Coefficient vs. Tip Speed Ratio. (Hartwanger & Horvat, 3D Modeling of a Wind Turbine Using CFD, 2008).....	130

LIST OF TABLES

Table 2.1- Relative power density of marine currents compared to wind and solar sources.....	28
Table 3.1- Surface tension of water in contact with air based on water temperature. (engineeringtoolbox.com).....	65
Table 5.1- Generated Power vs. Current Velocity.....	126
Table 5.2- Generated Power vs. TSR.....	127

NOMENCLATURE

a	axial flow induction factor	ν	kinematic viscosity of water at 20 °C
A	aerofoil area	Ω	rotational speed of the rotor
c	chord length; celerity or phase velocity	λ	tip speed ratio
c_l	lift coefficient	ϕ	angle between incident flow and the chord
c_d	drag coefficient	ϕ_w	phase angle of wave
c_m	moment coefficient	ρ	water density
C_p	power coefficient	μ	kinematic viscosity
C_T	thrust coefficient		
d	water depth		
D	diameter of the rotor		
H	wave height		
k_w	wave number		
L	wave length		
M	bending moment		
n	rotational speed (rev/s)		
P	power		
Q	torque		
R	radius of rotor		
Re	Reynolds number		
T	thrust		
T	wave period		
u	wave particle velocity in horizontal direction		
v	wave particle velocity in vertical direction		
U	free stream velocity		
U_c	current speed		
zr	instantaneous vertical position of centroid of blade section with respect to rotor axis		
α	angle of attack		
β	inclination of local chord to rotor plan (i.e., blade twist plus pitch angle, if any)		
θ	incident angle of current		
θ_w	incident angle of wave		

CHAPTER 1

INTRODUCTION

1.1 Background

The concept of marine current turbines was initially developed by Peter Fraenkel who founded an internationally recognized renewable energy consultancy company, IT Power Ltd. His main focus was water current technology, along with hydropower and wind, and he is responsible for inventing the fundamental patents and is owned by Marine Current Turbines (MCT). As early as the 1970s, Peter was testing a current turbine that he designed, which was later used on the Nile in Sudan. The turbine was used to pump water for irrigation. In the 1990s Peter built the world's first tidal turbine with rotor blades 3.5 meters in diameter. The first turbine generated 15 kilowatts during the summer of 1994 using the cold currents of Corran Narrows in Loch Linnhe, Scotland. As a result of more funding from European countries in the late 1990s and early 2000s, Peter and his company were able to create a larger scale technology known as the SeaFlow project in Devon, United Kingdom, and now the SeaGen in Northern Ireland (Marine Current Turbines Limited, 2011).

The ocean currents around the world possess a tremendous amount of energy flux which can be successfully harnessed by marine current turbines. In order to ensure that

these turbines are adequately designed to be efficient, some types of full scale tests must be carried out. Due to the high density of seawater as compared to air, marine current turbine blades experience a much higher pressure distribution than that of wind turbines. However, the principal concepts remain the same when computing the forces, pressures and bending moments on the blades in both marine current and wind turbines. Over the years, modeling a full scale marine current turbine seemed impractical due to the large blade diameters. Computational Fluid Dynamics (CFD) studies have made this analysis much easier. By using computer simulated marine current and turbine operation, accurate results on blade forces, pressures and bending moments can now be calculated easily. CFD software has been used to carry out simulations on smaller turbines or portions of large turbines under still water conditions. However, the present study uses ANSYS FLUENT to carry out a full scale numerical simulation on a complete three-bladed rotor subjected to combined wave and current effects.

1.2 Scope of the Thesis

Florida is faced with an energy crisis with respect to capacity, supply, cost, emissions, and stability. The waters offshore the coast of Ft. Lauderdale can provide a good source of clean, reliable, locally renewable energy by using marine current turbines to harness this power. As a result, Florida Atlantic University's Center for Ocean Energy Technology endeavored to design, fabricate, deploy and operate an experimental small scale turbine. This 20 kW Ocean Current Turbine Testbed (OCTT) is an open-blade axial flow horizontal underwater turbine driven by a 3 m diameter 3- blade rotor (Figure 1.1).

It is intended to operate in the open ocean near the core of the Florida current, offshore Ft. Lauderdale. This turbine is not intended to be a scaled prototype of a commercial model, but it is intended to be an experimental system to assess technology, identify gaps, investigate and collect data about potential environmental impacts, and provide a foundation for commercial and policy development (Driscoll, et al., 2009).

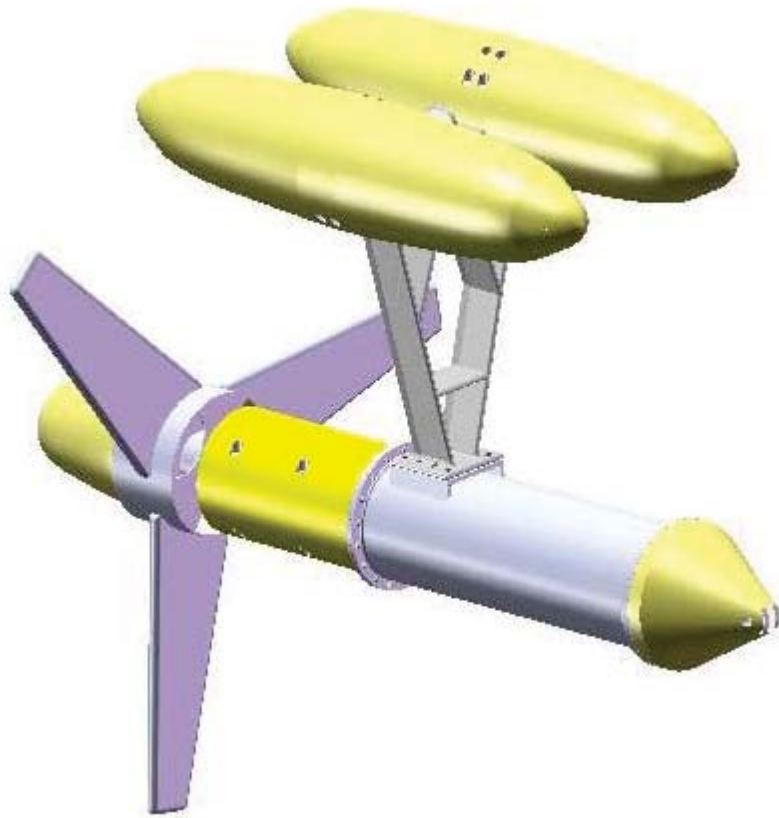


Figure 1.1- A diagrammatic representation of the 20 kW turbine.

1.3 Environmental Impacts

SeaGeneration (Kyle Rhea) Ltd recognizes the importance of protecting the marine life near the waters of a marine current turbine. The proposed location for the

SeaGen Kyle Rhea project near Scotland is the home for many mammals such as cetaceans, seals, otters, basking sharks, as well as species of flora and fauna. As a result, SeaGen Kyle Rhea has implemented an environmental study to be completed in the summer of 2012. This study examines the possible impacts of the turbine on the marine life by utilizing a number of experts in marine mammals, fisheries, landscape, coastal processes, birds, benthic ecology, underwater noise and navigation. The results of this study will be published in a public Environmental Statement so that the SeaGen Kyle Rhea turbine array can be properly licensed. Currently, SeaGen's turbines rotate at approximately 14 rpm, which is deemed slow enough to be unlikely to pose a threat to man or wildlife. Thus far, no significant impact is seen on the marine environment at Strangford Lough.

1.4 Computational Fluid Dynamics (CFD) Analysis

The computational methods most widely used for horizontal axis marine current turbines are Blade Element Momentum (BEM) theory and Computational Fluid Dynamics (CFD). The main focus of using the CFD method in this study is to improve the accuracy and precision of results by using fine enough mesh quality. The mesh quality is chosen based on the geometry so that individual tetra-hedral elements are within close proximity of each other near the leading and trailing edge of the turbine blades and near the roots.

The results from the CFD model is used to discuss and analyze the changes in thrust, power and torque in the marine current turbine when operating in still water as

compared to the actual sea condition with waves. The analysis gives the user the ability to understand how different wave heights will affect the turbine performance characteristics.

The study will utilize a turbine designed by the National Renewable Energy Laboratory (NREL). The 43.2 m diameter turbine rotor is modeled using a 3D Computer Aided Design (CAD) tool, SolidWorks. The modeled turbine is drawn to scale based on geometric curves obtained from NREL and connected to a user defined generic hub. The 3D part is then meshed using ANSYS ICEM CFD. ICEM CFD is a geometric mesh generation tool designed to repair, analyze and mesh the solid rotor blade with tetrahedral volume meshing elements. A computational domain is also created and meshed to simulate the water and air regions of this model. The entire mesh setup is imported into ANSYS FLUENT where the CFD analysis is done followed by parametric studies to determine the effects of the waves with the current on the marine current turbine.

1.5 Structure of the Report

The proposed study is presented in the following six chapters:

Chapter 1 presents an insight into the background and introduction to the present study.

Chapter 2 provides literature review including the wind energy correlation, marine current energy resource, resource extraction technologies, power from marine currents, and the overview of the CFD method.

Chapter 3 discusses the transient, incompressible, and laminar fluid flow including flow characteristics, CFD, ANSYS FLUENT basics, the finite element method, blade element momentum theory and the principles of similitude.

Chapter 4 describes the creation of a three dimensional model, meshing the model, creation of an adequate computational domain, and multiphase fluid flow simulation.

Chapter 5 presents the results of mathematical modeling of the rotor blades subjected to wave heights and current velocities.

Summary, conclusions and future work are presented in Chapter 6.

CHAPTER 2

LITERATURE REVIEW

2.1 Introduction

Wind energy extraction techniques have evolved significantly over the last two decades. Wind energy converters were known to be less than 20 meters in diameter in the past and capable of generating about 100 – 200 *kilowatts (kW)* of electricity in rated winds. Today, these devices have diameters in excess of 65 meters, producing over 1 *Megawatt (MW)* of power with electricity generation prices of less than \$0.04/*kWh* in good wind sites (Winterstein, Fitzwater, Manuel, & Veers, 2001). This chapter presents the literature review with a focus on marine current turbines.

2.1.1 Short Term and Long Term Effects on Wind Turbines

When predicting the loads on a wind turbine, two orthogonal blade-root moments are analyzed: “flap-wise moment” (out of plane rotation) and “edgewise moment” (in the plane of rotation). These moments contribute directly to the random stress cycles that occur within the lifetime of the turbine. Using time histories of the moments, the fatigue-load spectra are calculated based on short-term and long-term effects (Winterstein, Fitzwater, Manuel, & Veers, 2001).

Short-term effects are described by quasi-stationary wind conditions over a duration of 10 *minutes*. A quasi-stationary wind condition refers to one in which the average wind speed, V , and turbulence intensity, I , are constant. These short-term effects are associated with respective statistical moments of the bending moment ranges that are present. These statistical moments are related to the average wind speed and turbulence intensity; hence, the short-term range distribution can be predicted for any combination of wind conditions.

Long-term effects are predicted by performing summation of the short-term effects over the input conditions for the joint annual moment distribution. This study offers a 95% confidence level on the distribution of long-term loading based on a limited data set.

One of the main concerns in analyzing the potential of marine current turbines is the possible occurrence of drag due to cavitation. Cavitation occurs when turbulence is created by the formation of air bubbles around the turbine blades, causing a substantial decrease in efficiency. Other concerns include preventing marine growth buildup, corrosion control, and ensuring reliability of the system. Some devices have been manufactured to tap into the vast capacity of marine current generated power. One of these devices is located in Lynmouth and is called the SeaFlow Project.

2.2 Marine Current Energy Resource

Marine current energy generation follows the basic principles used for wind turbines. Over the years, extensive research has been conducted to achieve a practical and cost-effective large-scale system designed to harness the kinetic energy from marine

currents all over the world. Land-based forms of renewable energy are faced with restrictions due to land use. Making use of the ocean currents creates the opportunity for harnessing power without the harmful effects on the environment or human activities (Fraenkel P. L., Power from marine currents, 2002).

The main sources of marine energy are waves, currents and ocean thermal energy. Other means of harnessing power from the ocean involves indirect means such as offshore wind turbines. The main focus of the study presented by Fraenkel P. L. (2002) is to analyze the generation of power from marine currents so that there will be less reliance on fossil fuels or nuclear power. In order to harness this power efficiently, numerous studies have been carried out to analyze the turbine operation under different wind, wave, and current conditions. Using marine current turbines, power generation is more secure due to the consistent velocities and flux through most current streams around the world. One disadvantage in using this form of renewable energy is the cost associated with implementing the technology and maintaining the equipment. However, the power output is significantly higher when compared to an equivalent sized land-based wind device.

Marine currents are primarily driven by heating of the waters near the equator due to wind and solar effects (U.S. Department of the Interior, 2006). The currents that result are quite constant in magnitude and direction, as opposed to tidal currents, which change direction. Figure 2.1 shows examples of existing marine currents such as the Gulf Stream, Florida Straits Current, and California Current. While the California Current has relatively slow speeds and shifts direction periodically, the Florida Straits Current starts about 8 km offshore the coast of Miami, and sustains relatively large speeds over significant distances in relatively unchanging patterns. Although marine currents tend to

be concentrated at the surface, significant current continues at depths below ships' drafts. Marine current speeds tend to be less than wind speeds due to the significantly large amount of kinetic energy needed to move a body of water. Water is also about 835 times denser than wind, so the energy contained in a *12-mph* flow of water is equivalent to that contained in a mass of moving air at *110-mph*. As a result of the significant energy potential in marine currents, turbine technology that utilizes this untapped reservoir is reasonably justified.

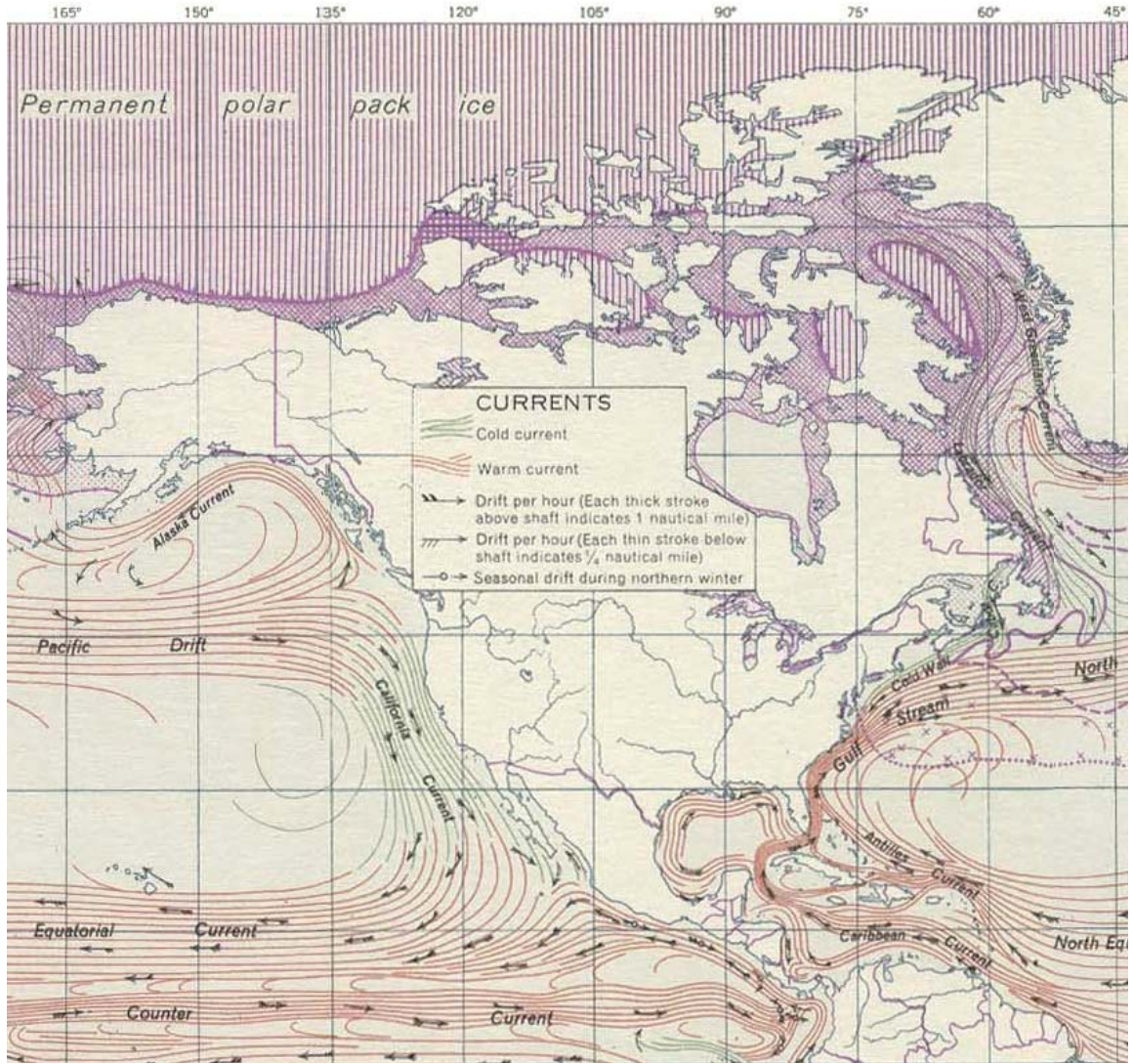


Figure 2.1- Marine Currents in the Vicinity of the United States (University of Texas Libraries 2006).

The total worldwide power available from marine currents has been estimated to be approximately 5,000 GW, which translates to an optimum power density of 15 kW/m^2 . Near the surface, the Florida Straits Current has an extractable energy density of about 1 kW/m^2 of flow area. The Gulf Stream possesses 21,000 times more energy than Niagara Falls in a flow that is 50 times the total flow of freshwater in the world. This

translates to an electrical supply in Florida that is 35% of its needs (U.S. Department of the Interior, 2006).

2.3 Power Extraction

Marine current turbines capture the energy from a stream of water through the processes of hydrodynamic lift or drag. They operate under the same concepts as wind turbines which use aerodynamic lift or drag to harness power. Therefore, marine current turbines require much of the same hardware as wind turbines such as rotor blades, a generator, and a method of power transportation from the energy conversion device to the electrical grid.

Turbines may either be horizontal axis or vertical axis, depending on which type of rotation is desired. The device requires a supporting fixture, cables, or anchors in order to keep the turbine from becoming unstable. Some applications use concentrators (shrouds) around the blades to increase the flow and power output from the turbine. In large areas where powerful current are present, it becomes lucrative to create clusters of marine current turbines or a turbine 'farm' (U.S. Department of the Interior, 2006). Figure 2.2 shows two different anchoring methods used by Gulfstream Energy Incorporated.

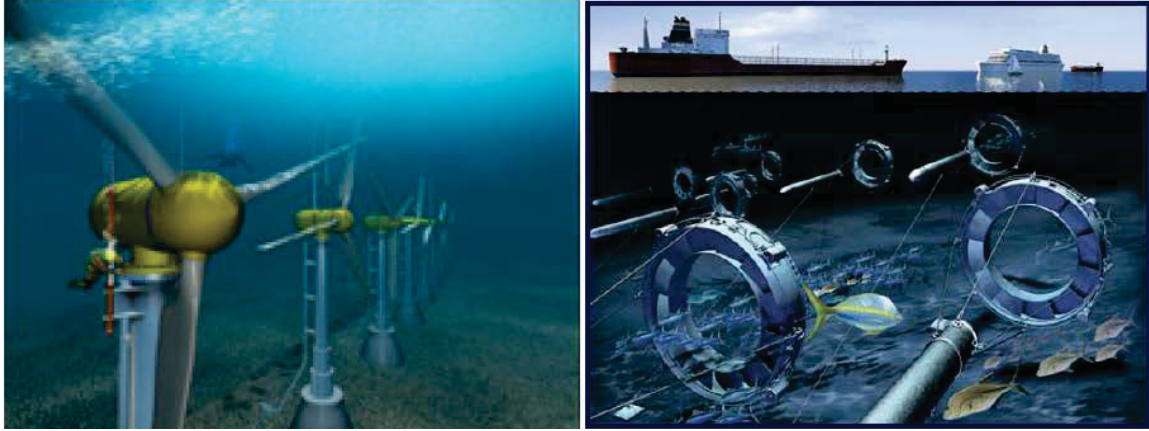


Figure 2.2- Visualization of two possible turbine and anchor technologies (Hammerfest Storm AS 2006; Gulfstream Energy Incorporated 2006).

2.3.1 Admiralty Inlet ocean current data analysis

Metaocean data was acquired from the Northwest National Marine Renewable Energy Center (NNMREC). The data was compiled by a team from the University of Washington Branch: Tidal Energy. The data was collected using an Acoustic Doppler Current Profiler (ADCP). An ADCP uses sound waves to record current velocities with respect to depth. The ADCP data was collected for the Admiralty Inlet at various locations throughout the year 2009. During the month of April, several sets of data were collected for durations of about 20 *minutes*. These data sets measured the magnitude of both horizontal and vertical velocities, as well as the velocity direction with respect to depth. As seen in Figure 2.3, the ADCP data is collected up to a depth of 80 *meters*, close to the seabed.

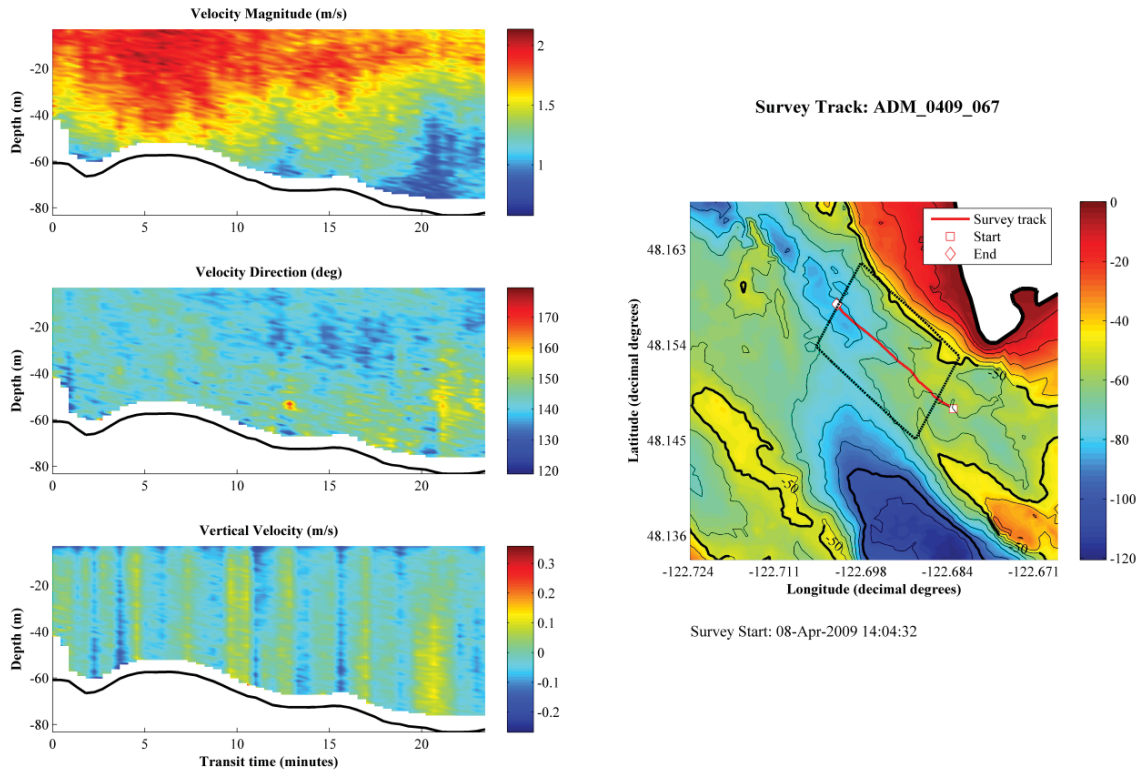


Figure 2.3- Admiralty ocean current data collected at 14:02:32 08-Apr-2009 (Northwest National Marine Renewable Energy Center[NNMREC], University of Washington Branch: Tidal Energy)

After the analysis of the data, values were visually read from the charts for velocity magnitude. These values are used to create the current velocity profile shown in Figure 2.4.

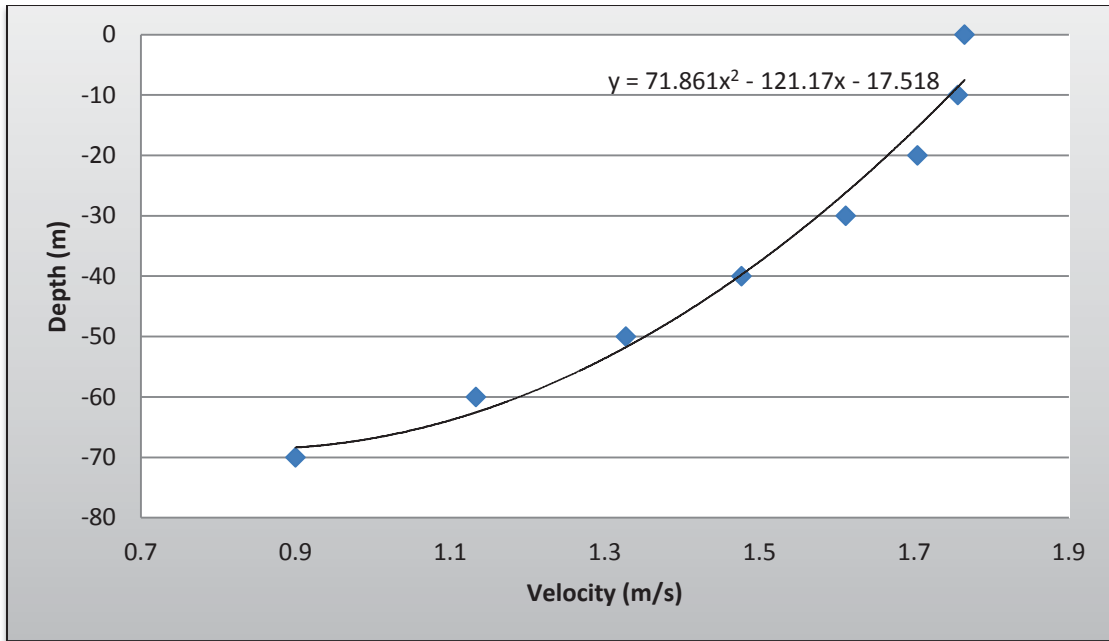


Figure 2.4 – The average current velocity profile for approximately twenty minutes of data collection. Intervals were chosen and data values were picked off of the above chart using the colored key for current velocity

The tidal current velocities are usually modified based on various factors such as: residual momentum, global oceanic marine circulation, wind fetch and density variations and the rotating velocity vectors caused by passing waves. When the current velocity reaches a certain level suitable for power generation, the velocity vectors exceed the other effects significantly. The current velocity varies with respect to depth in the ocean. This relationship is described by a seventh power law as a function of depth in the lower half of the flow (Fraenkel P. L., Power from marine currents, 2002). Equation (2.1) gives the power law expression for the current velocity:

$$V = V_0 \left(\frac{z}{d}\right)^{\frac{1}{7}} \quad (2.1)$$

Where: V = Current velocity

V_0 = Current velocity at surface level

Z = Variable depth (measured from seabed)

d = Total depth to the seabed from surface

2.3.2 Metaocean Data for Southeast Florida

Variable Depth Research

There are two types of ocean currents: surface currents or circulation, and thermohaline circulation. Surface currents are found in the upper 400 m of ocean and are currents that are driven by wind. Surface currents make up 10% of all the water in the ocean. Deep water currents, or thermohaline circulation make up the other 90% of the ocean. These currents move around the basins in the ocean due to forces caused by density and gravity. The temperature and salinity of the water causes these forces to fluctuate. Ocean currents are caused mainly by two forces. The first is called primary force and comprises of solar heating, wind, gravity, and coriolis. These forces start the water moving. Secondary forces are the other kind of force and they influence where the currents flow. The presence of both types of ocean currents is seen in Florida. These currents are responsible for mass transport greater than 30 times the total freshwater river flows of the world. This results in an energy flux of approximately 25 GW. The Florida current has the potential to generate up to 10 GW of power (Driscoll, et al., 2009). A test turbine has been proposed in Dania Beach, Florida by the Southeast National Marine

Renewable Energy Center (SNMREC). The proposed turbine is a 20 kW Open Current Turbine Testbed (OCTT) which has an open-blade, axial flow horizontal axis turbine driven by a 3 m diameter, 3-blade rotor. In order to carry out sufficient tests on this turbine, the SNMREC endeavored to collect nearly two years of current velocity measurements. These measurements were taken near the core of the Florida Current offshore Ft. Lauderdale, Florida (Driscoll, et al., 2009). The data reflected an average current speed at the surface of 1.7 m/s. The ocean bottom is at 320 m, where the current velocity is estimated to be in the vicinity of 0.19 m/s. Figure 2.5 shows the mean current velocity with respect to depth for the data collected by SNMREC using the ADCP.

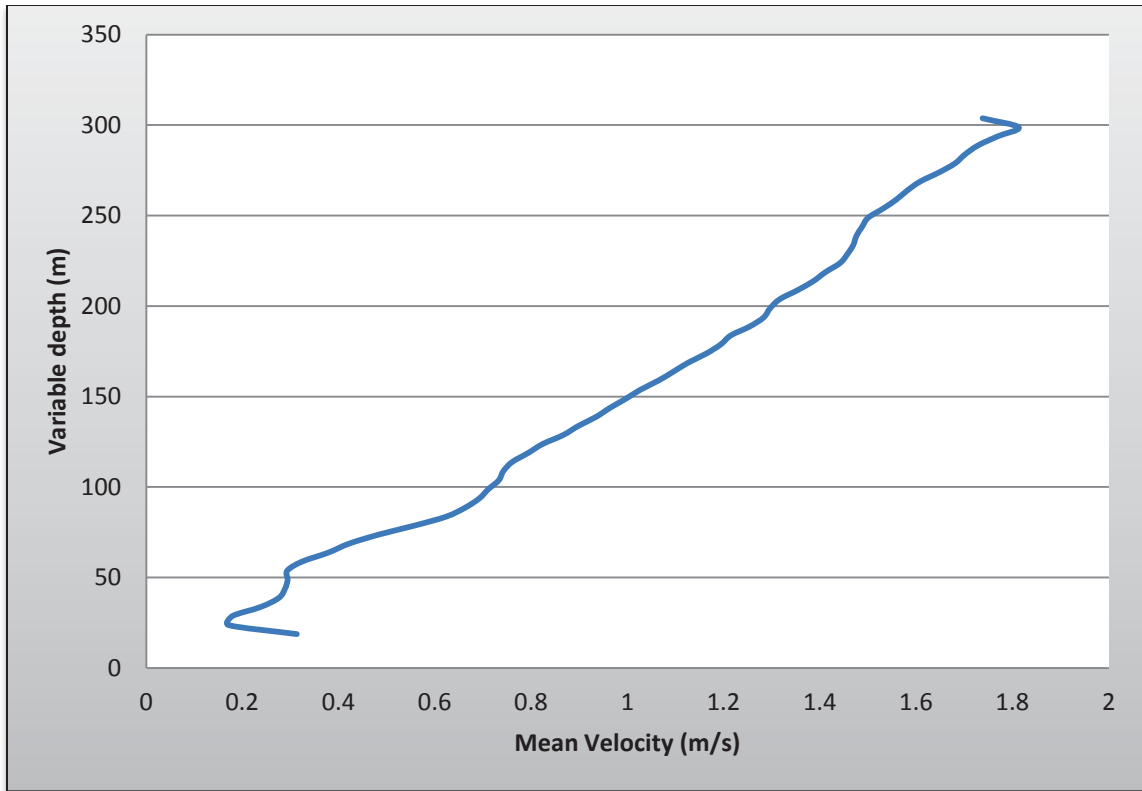


Figure 2.5 - Raw velocity data showing current profile of the mean velocity with respect to ocean depth.

Analysis for the Florida Current

Figure 2.6 shows the wave height information for Tuesday, September 6th 2011. The wave height data from the National Weather Service, Miami, was observed for a period of time, and the wave height values were found to be roughly the same. A maximum wave height of 2 feet (0.609 m) is seen from Figure 2.6. This information is used in the present study as input into the ANSYS wave models.

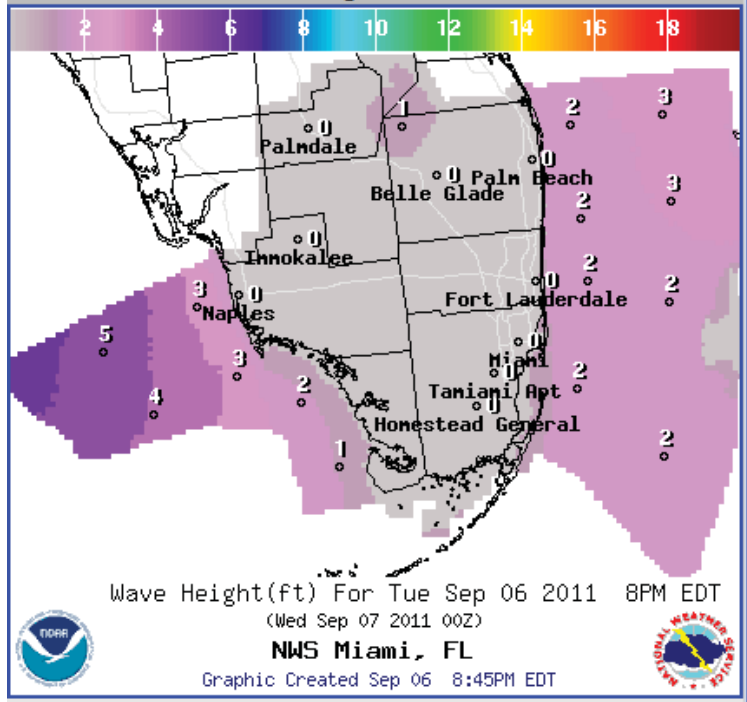
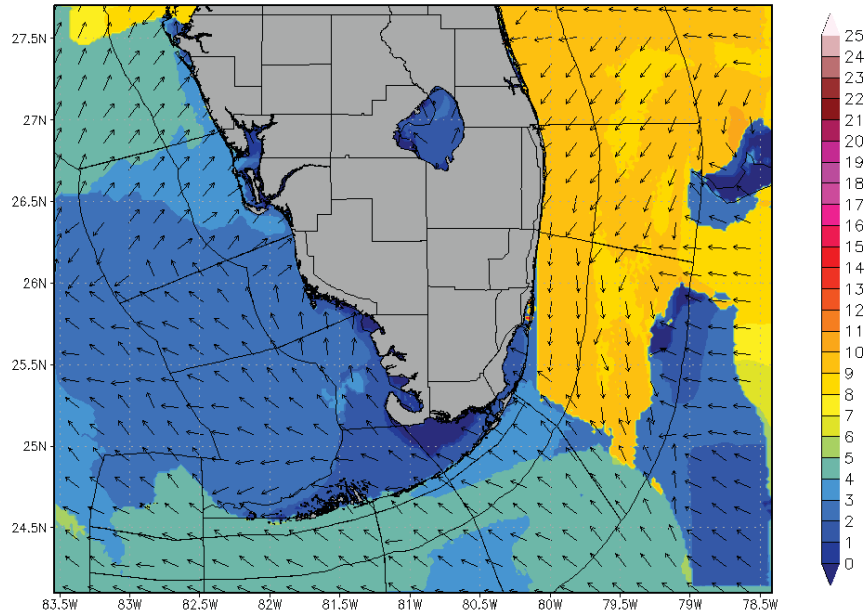


Figure 2.6- Peak wave heights near the Southeast Florida region showing wave heights offshore the coast of Ft. Lauderdale and Miami. (NOAA National Weather Service).

Figure 2.7 shows the peak wave period in feet for the waters offshore the coast of Ft. Lauderdale.

SWAN Peak Wave Period (s) and Direction
Hour 114 (12Z11SEP2011)



SWAN Peak Wave Period (s) and Direction
Hour 27 (21Z07SEP2011)

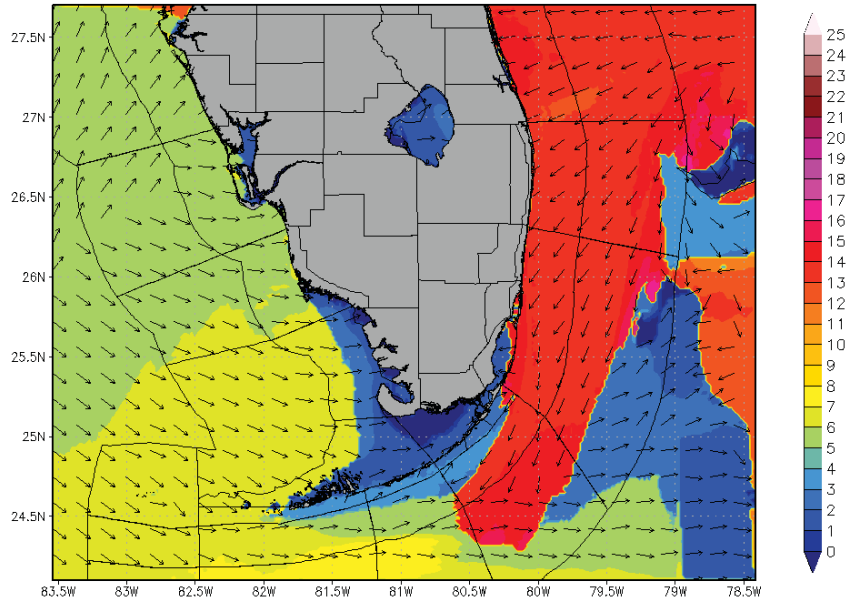


Figure 2.7- Peak wave periods near the Southeast Florida region showing the wave periods offshore the coast of Ft. Lauderdale and Miami. (NOAA National Weather

Service).

2.4 Marine Current Extraction Technologies

Similar to wind energy conversion devices, the use of marine current energy converters is dependent on the flow characteristics of the ocean currents. The effects of the turbine on the current flow, the interactions with the free surface, the seabed, and marine life are equally important to the conversion of marine current energy (Maganga et al., 2009). The French Research Institute for Exploitation of the Sea (IFREMER) has been developing software capable of modeling three-dimensional flow on the marine current turbine in order to study the wake effects of turbine operation. The wake effects are important to assess the disturbances generated on the turbine's adjacent ocean environment. Furthermore, the proximity of turbines when building a marine current energy farm will be determined by the wake effects to maximize the inflow velocity for each turbine. IFREMER used a free surface circulation flume tank in order to carry out experimental tests to validate their numerical work. The tri-bladed horizontal axis turbine was tested for wake effects, and efficiency. The efficiency of the turbine is determined based on the thrust and power generated by the rotor subjected to different flow characteristics. The wake was characterized by Laser Doppler Velocimetry (LDV) (Maganga et al. 2009). LDV is used in the study of various flows like atmospheric turbulences and flows in internal combustion engines. The experiment uses the Doppler Effect to calculate the velocity of fluid particles (Kalkert & Kayser, 2006). Experiments were carried out on a 1/30th scale model. The pitch angle of the three blades was adjustable, and the test rotor measured 0.7 m in diameter. The model was tested in current speeds ranging from 0.5 to 1.5 m/s and turbine performances obtained over a range of rotor speeds from 10 to 190 rpm, and blade pitch angles from -5 to

15 degrees. The flume tank measured 18 m long by 4 m wide and 2 m deep. A pump was used capable of generating flow velocity between 0.1 to 2.2 m/s. The use of honeycomb straighteners caused a flow turbulence between 8 and 25%. The LDV was used along with another non-intrusive optical measurement device called Particle Image Velocimetry system (PIV). The LDV was used for local measurement whilst the PIV was used for global measurements. Figure 2.8 and Figure 2.9 show the submerged test turbine in the flume tank and the layout of the water tunnel respectively.

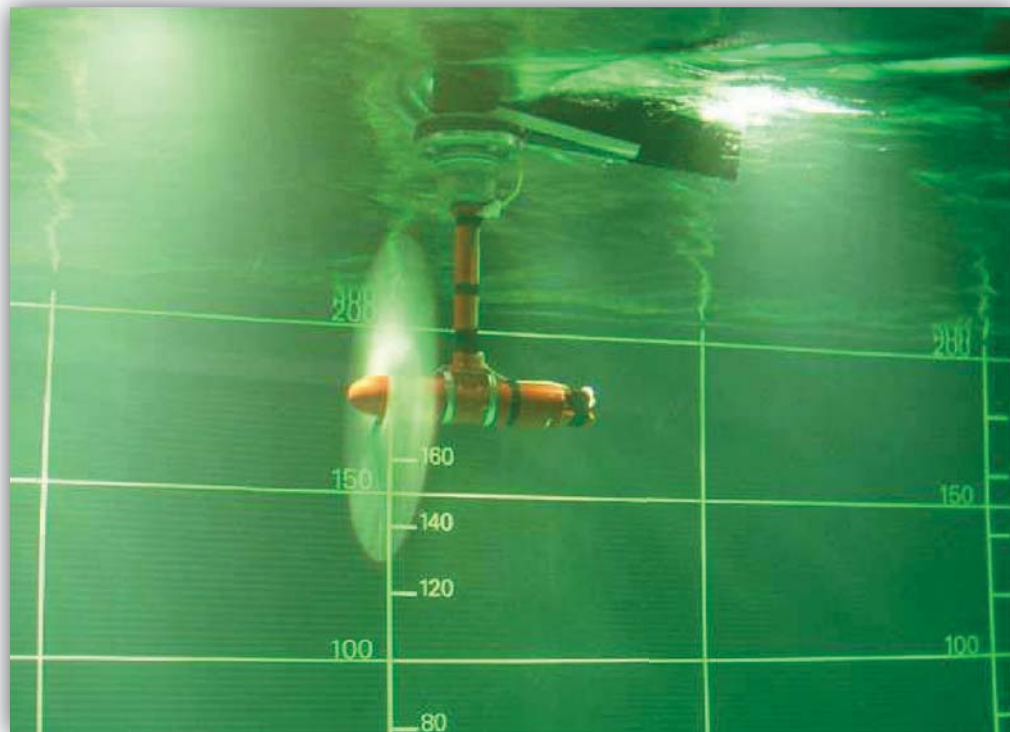


Figure 2.8- Model turbine during trials in the IFREMER tank.

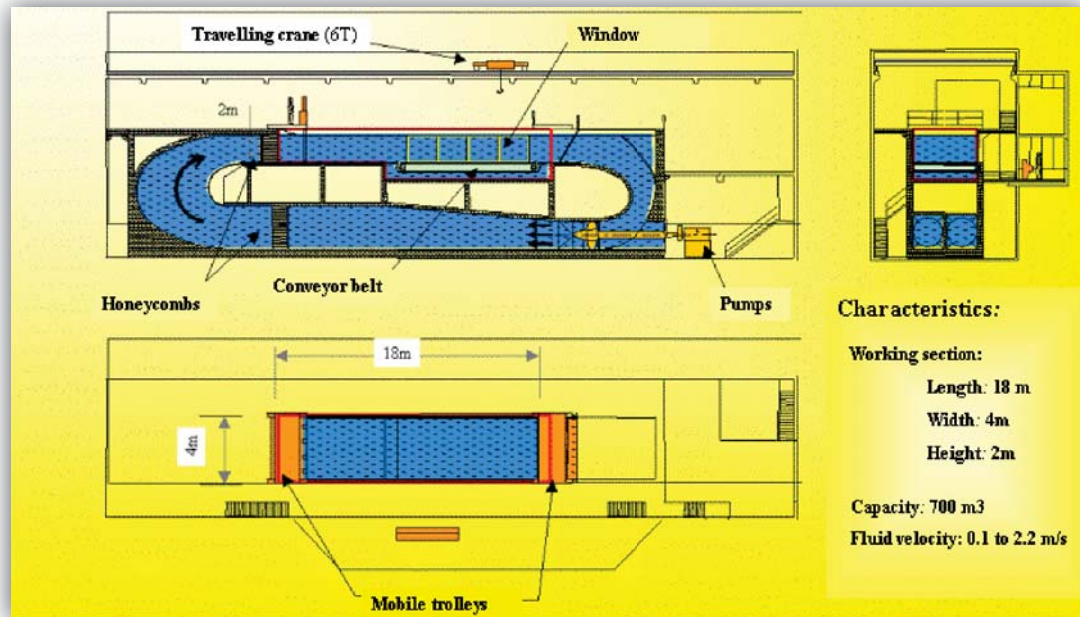


Figure 2.9- IFREMER free surface hydrodynamic water tunnel located in Boulogne-sur-Mer, France.

The results are expressed in terms of the tip speed ratio which is given by Eqn. (2.4.1).

$$TSR = \frac{\Omega D}{2U_{\infty}} \times A \quad (2.4.1)$$

Where A is a coefficient, $\frac{\Omega D}{2}$ is the tangential speed at the tip of the rotating blades, and U_{∞} is the inflow velocity of the system. The thrust coefficient was plotted as a function of TSR for a working current velocity range of 0.6- 1.5 m/s . Figure 2.10 shows the plot of the parabolic curve to describe the thrust coefficient.

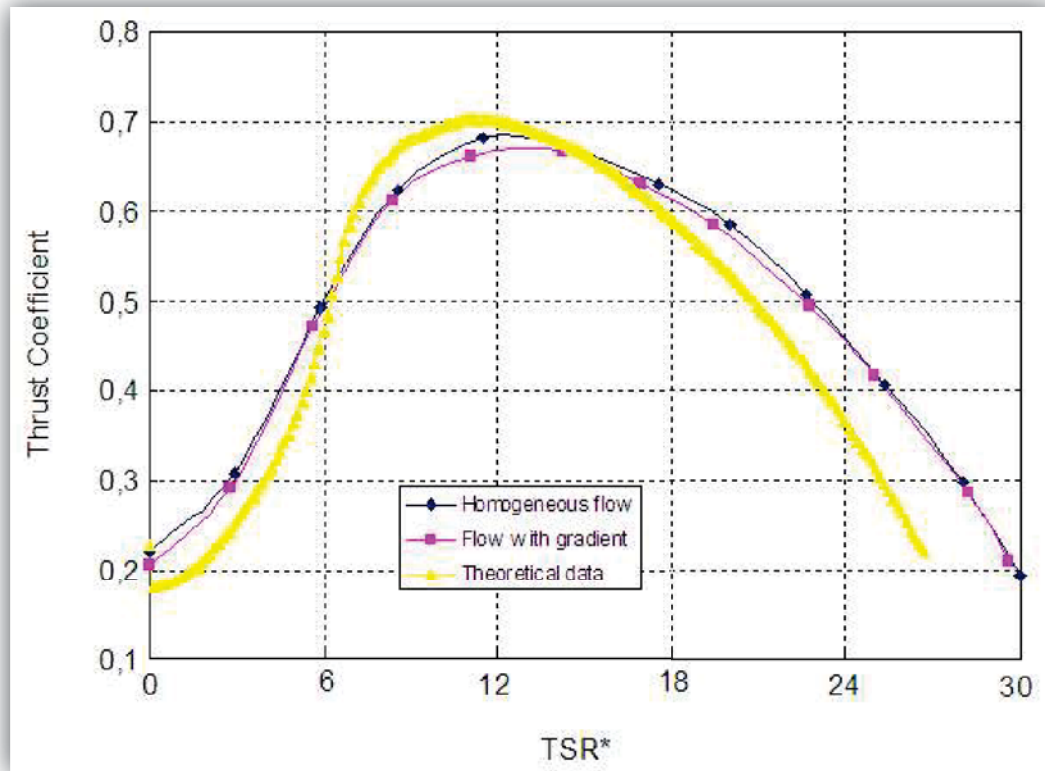


Figure 2.10- Thrust coefficient comparison (theoretical and experimental data) at a mean speed of 0.79 m/s (Maganga et al., 2009).

The measured power needed to ensure constant turbine rotational speed is shown in Figure 2.11 for homogeneous flow and flow with a transverse gradient of 8%.

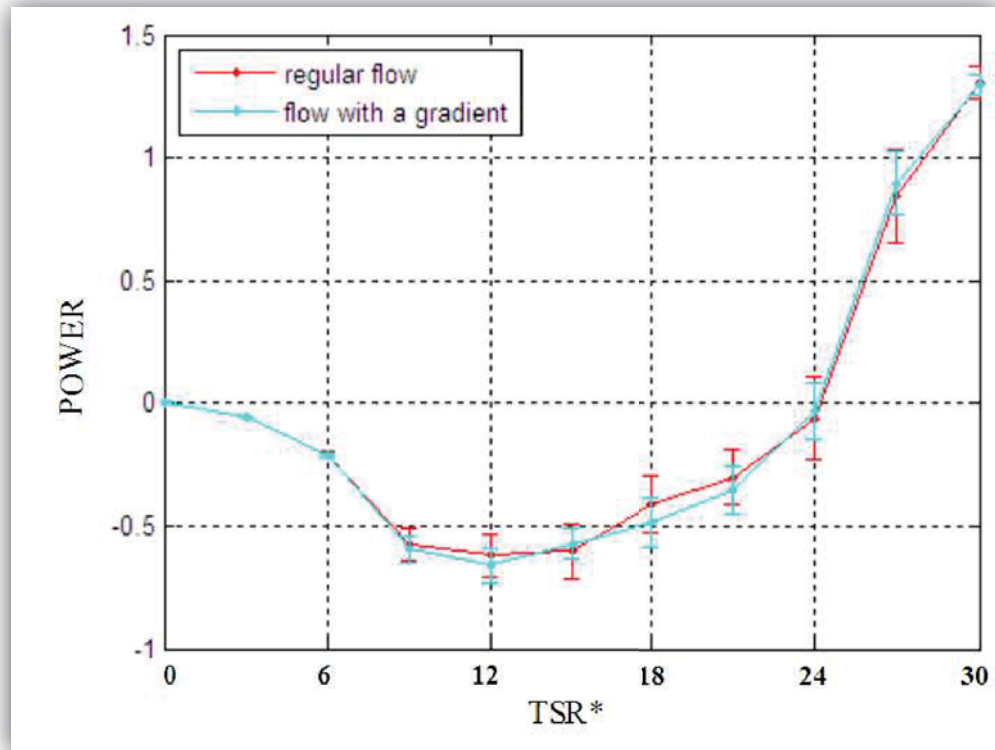


Figure 2.11- Measured power for a homogeneous flow and a flow with a flow gradient (Maganga et al. , 2009).

Angle of Incidence

The recorded thrust was seen to decrease when the incidence angle deviated from 0° . The rotor torque, however, was the highest when the incidence angle was set at 20° . The power generated showed some increased values for an incidence angle of 20° , when the tip speed ratio was between 9 and 15. Apart from this range, the recorded power was quite consistent for different angles of incidence.

Turbulence Intensity (TI)

Turbulence intensity does not seem to play a major role in the thrust generated from the turbine when operated for *TI* values of 8 and 25%. The power generated was

also only slightly affected by different TI values. Figure 2.12 and Figure 2.13 show the thrust and power generated at different turbulence intensities for varying $TSRs$ respectively.

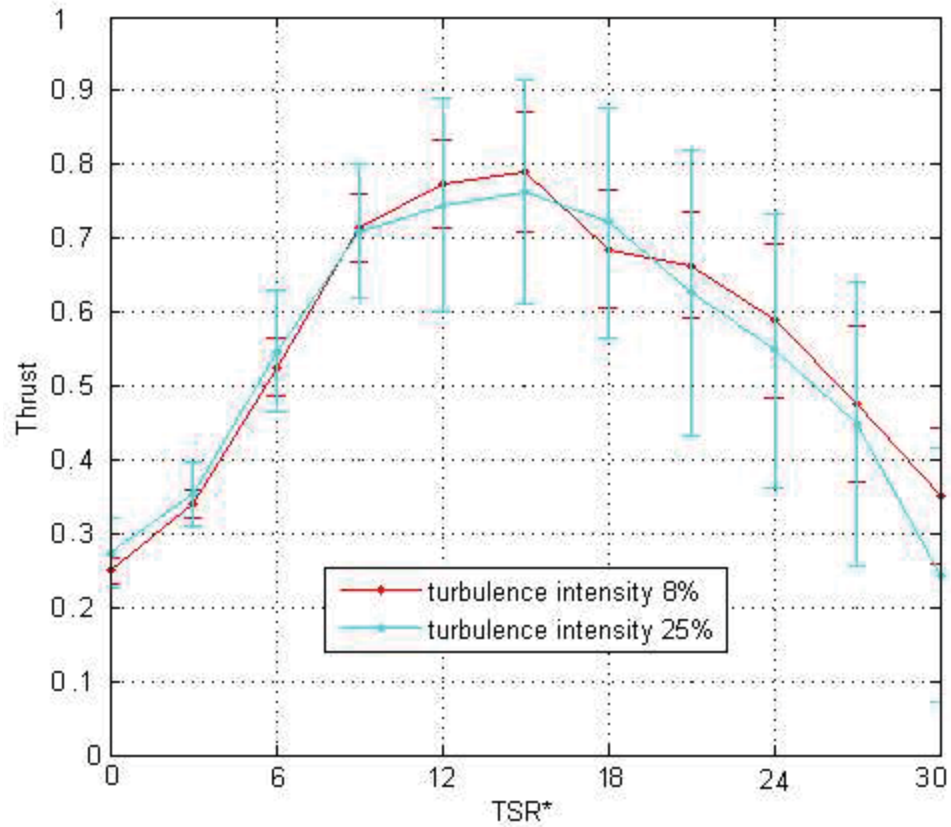


Figure 2.12- Normalized thrust for turbulence intensity levels of 8% and 25% at a mid-depth location (Maganga et al., 2009).

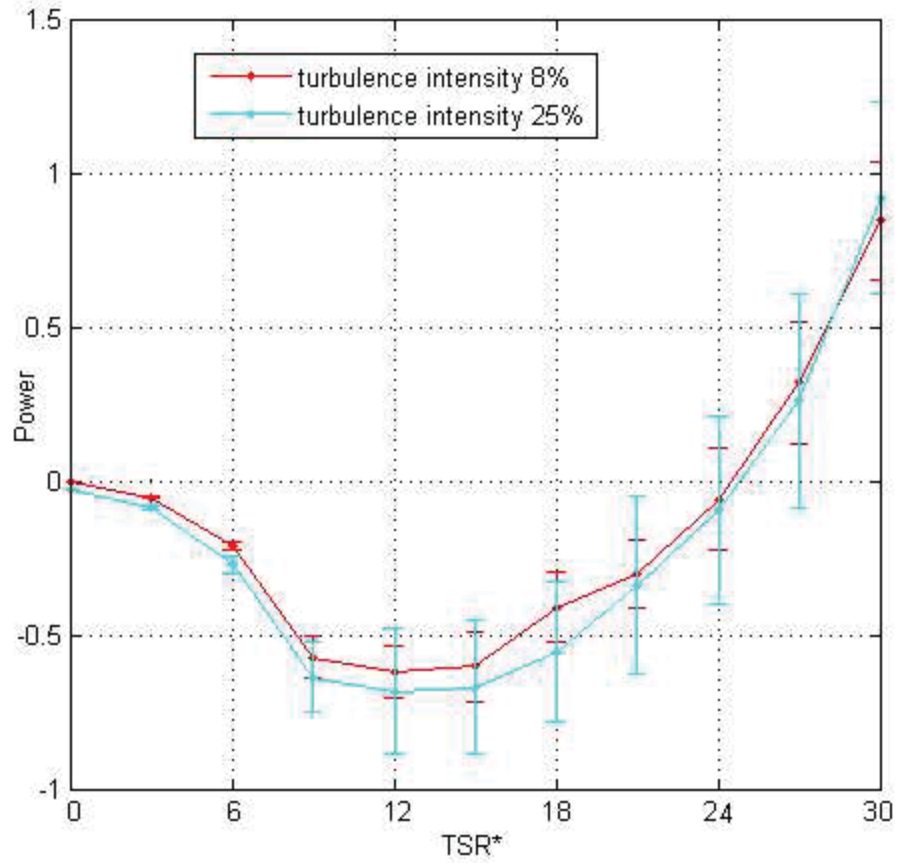


Figure 2.13- Measured power for both turbulence intensity rates of 8% and 25% at a mid-span location (Maganga, et al., 2009).

2.5 Power from Marine Current Turbines

The power available from a stream of water is given by Equation (2.5.1):

$$P = \frac{1}{2} \rho A V^3 \quad (2.5.1)$$

Where ρ is the density of water, A is the cross-sectional area of the rotor used to intercept the flow, and V is the free stream velocity of the current. As indicated by this

formulation, the power generated from a marine current energy device is highly dependent on the free stream velocity. As a result, the power density is exponentially influenced by increasing current velocity. Table 2.1 shows the comparison of the power densities for water velocities, wind speeds, and solar sources (Fraenkel P. L., 2002).

Table 2.1- Relative power density of marine currents compared to wind and solar sources.

	Energy Resource						
	Marine Currents					Wind	Solar
Velocity (m/s)	1	1.5	2	2.5	3	13	Peak at noon
Velocity (knots)	1.9	2.9	3.9	4.9	5.8	25.3	
Power Density (kW/m²)	0.52	1.74	4.12	8.05	13.91	1.37	~1.0

The ideal location for a marine current turbine is one where there is fast flowing water with little change in the gradient of the seabed. A uniform seabed minimizes turbulence due to gradual changes in current velocity. This allows for a large enough turbine or farm of turbines to be installed. Proximity to the shore is also important in order to minimize the hardware needed to access the generated power and transport it to the respective destination. The power generated from a marine current turbine is based on the swept area of the rotor blades, the average efficiency in converting kinetic energy, and the load factor for the site. The load factor can be taken to be the ratio of the average power of the

system to the rated power of the turbine. This load factor can be significantly affected by any outages in power generation; hence the reliability of the turbine must be closely examined. The energy conversion system should be able to operate without human intervention for long periods of time due to costly equipment and services needed to perform maintenance on offshore devices. These costs far outweigh those for performing maintenance on equivalent land-based energy conversion devices. As a result, it is believed that the maintenance interval for marine renewable energy systems needs to be five years or more.

Efficiency of the Turbine

The ideal power generated from a wind turbine was described by A. Betz in 1920 using a one-dimensional model (Hartwanger & Horvat, 2008). An “actuator disk” was used to represent the rotor, creating a pressure discontinuity of area, A and local velocity, V . This area refers to the swept area of the turbine rotor blade. The stream of fluid flow past this area is idealized as the control volume with an initial upstream velocity of V_0 over an area of A_0 , and a slower downstream velocity V_3 over a larger area A_3 at the outlet. Figure 2.14 shows a sketch of the working actuator disk model utilizing the control volume of fluid for analysis.

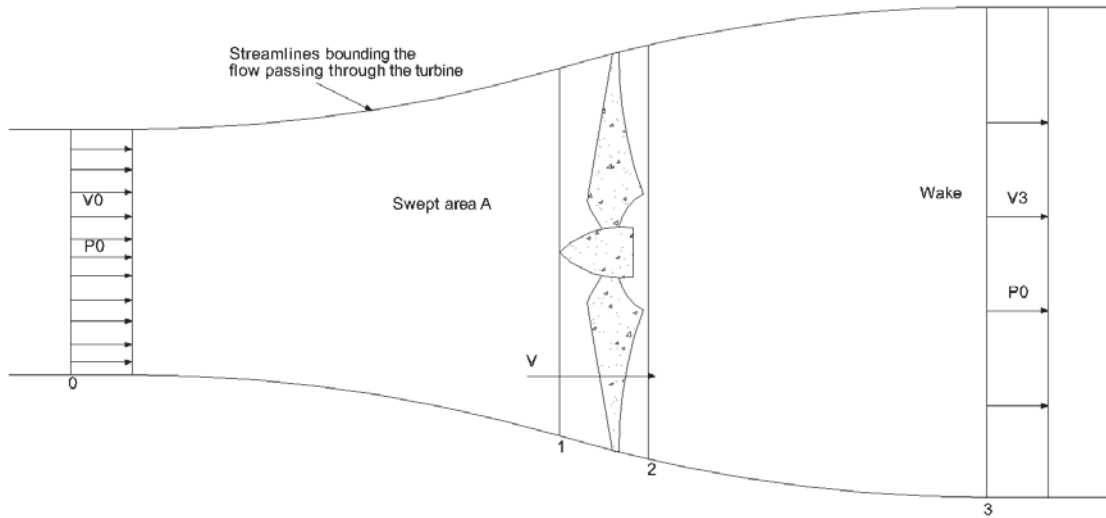


Figure 2.14- Control volume for the idealized actuator-disk theory.

The velocity at the face of the turbine, V , is taken as the average of the wind velocities upstream and downstream. Equation (2.5.2) gives the formulation of V .

$$V = \frac{1}{2} (V_0 + V_3) \quad (2.5.2)$$

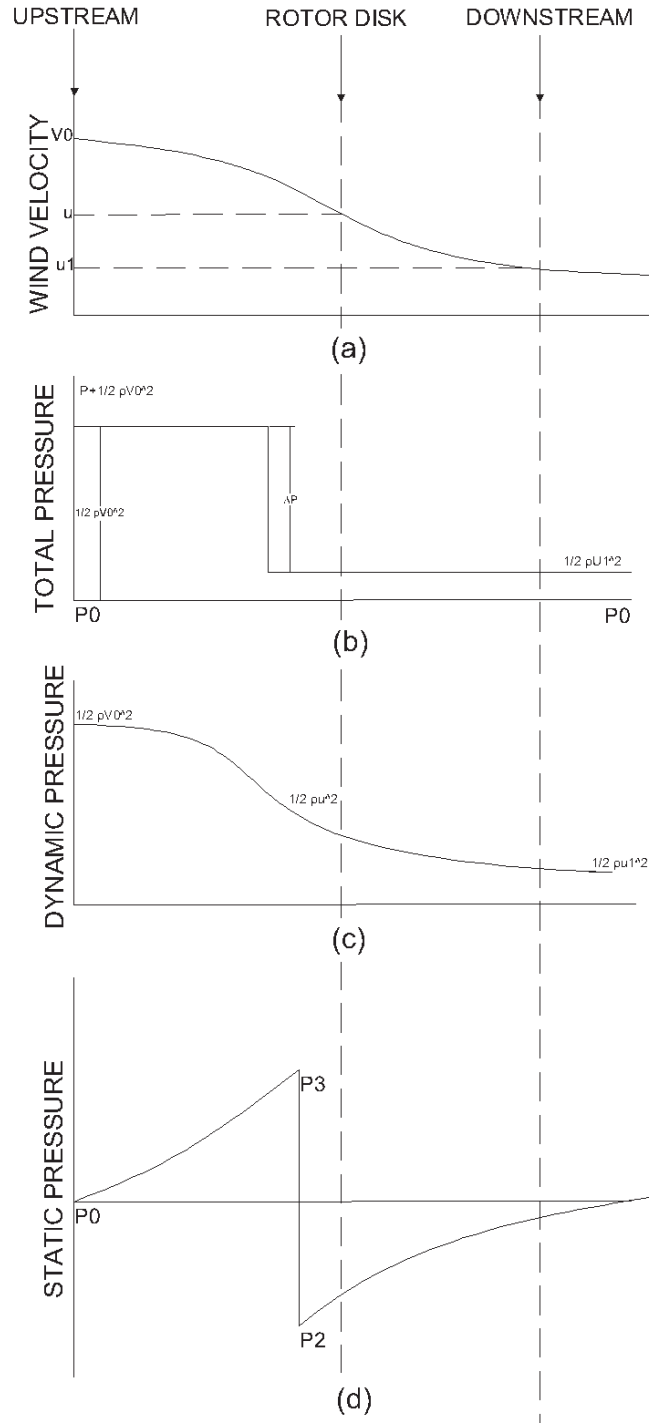


Figure 2.15- Actuator Disk Theory.

Figure 2.15 shows the Actuator Disk Theory for a wind turbine. The velocity and pressures in the present study will be compared to this theory.

The reduction in wind speed as the flow approaches the turbine rotor blade is expressed in terms of an axial induction factor, a . Equation (2.5.3) gives the formulation of the axial induction factor as follows:

$$a = \frac{V_0 - V}{V_0} \quad (2.5.3)$$

The value of a can be up to $\frac{1}{2}$ which requires V_3 to be 0. Therefore, the thrust on the turbine disk is calculated from Eqn. (2.5.4) below:

$$T = \frac{1}{2} \rho A V_0^2 4a(1 - a) \quad (2.5.4)$$

The maximum ideal thrust on a turbine rotor is given by Eqn. (2.5.5) as a function of inflow velocity as shown below (Harrison, et al., 2009):

$$T = \frac{1}{2} \rho V_0^2 A \quad (2.5.5)$$

The power coefficient, C_p , is defined in terms of a as follows:

$$C_p = 4a(1 - a)^2 \quad (2.5.6)$$

From Eqn. (2.5.5), C_p reaches a maximum value of 0.593, also known as the Betz limit for an ideal frictionless turbine. Figure 2.16 shows the power coefficient for varying axial induction factors.

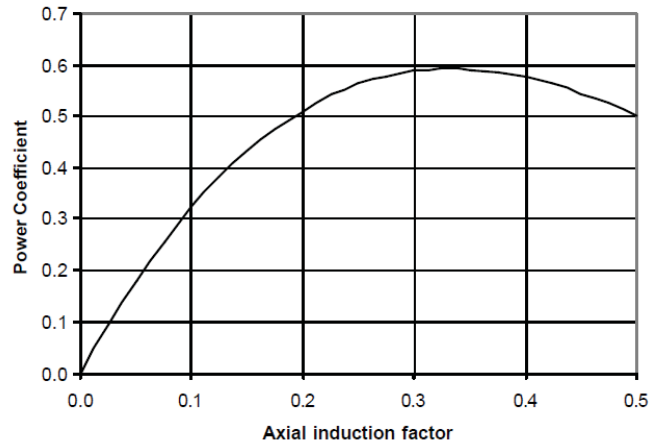


Figure 2.16- Power Coefficient for an ideal Betz model wind turbine.

The theoretical power generated by a wind turbine is dependent on the tip speed ratio.

Figure 2.17 shows the power coefficient with respect to changing tip speed ratio.

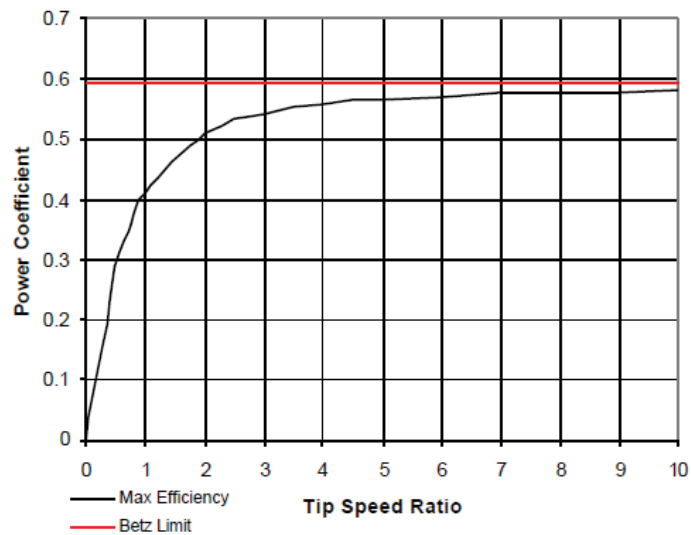


Figure 2.17- Theoretical maximum power coefficient.

Figure 2.18 shows a comparison of power coefficients of actual turbines to the ideal maximum values.

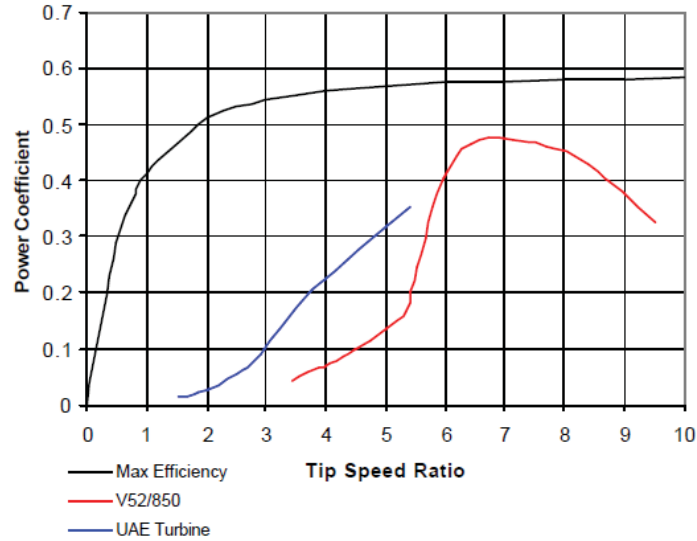


Figure 2.18- Typical turbine performance from real devices.

It is often important to vary the thrust coefficient when using a CFD analysis for marine current turbines. The thrust coefficient (C_T) is calculated based on the simulated thrust force from the CFD model using the following equation:

$$C_T = \frac{T}{0.5\rho U_0^2 A_d} \quad (2.5.7)$$

The generated torque is given by (Lee, et al., 2011) in the following equation:

$$C_p = \frac{Q\Omega}{\frac{1}{2}\rho\pi R^2 V_M^3} \quad (2.5.8)$$

Where Q is the Torque, Ω is the rotational speed and V_M is the model speed.

Cavitation inception can be described by the relationship between the cavitation number and the local pressure shown in Equation 2.5.9 and 2.5.10 respectively.

$$\sigma = (P_{AT} + \rho gh - P_V)/0.5\rho V^2 \quad (2.5.9)$$

Where, P_{AT} = Atmospheric pressure and P_V =Water vapor pressure.

$$C_{pressure} = (P_L - P_0)/0.5\rho V^2 \quad (2.5.10)$$

Where, P_L = Pressure at particular location and P_0 =Initial pressure.

2.6 Rotor Blade Types

Designs from wind energy applications may be adopted for marine current turbines, since the principles used for converting kinetic energy are similar for wind or flowing water. The main focus of designing a marine current turbine rotor blade is to maximize lift forces and minimize drag. In order to fulfill this requirement, two types of turbines have been considered by researchers. The first is the axial flow or propeller type, in which the direction of current flow coincides with the rotor axis. This type of turbine requires a drive train to be located either at the rotor hub or at right-angles to the energy transmission mechanism in order to transmit the energy. The second type of rotor blade is the cross-flow or Darrieus rotor. A Darrieus rotor transmits torque directly upward or downward due to its perpendicular axis of rotation to the current flow. This allows easier mechanism setup for harnessing power from a surface vessel or from equipment at the

ocean bottom. Figure 2.19 (A) and (B) show the different rotor types. The present study considers the axial flow turbine for modeling and analysis.

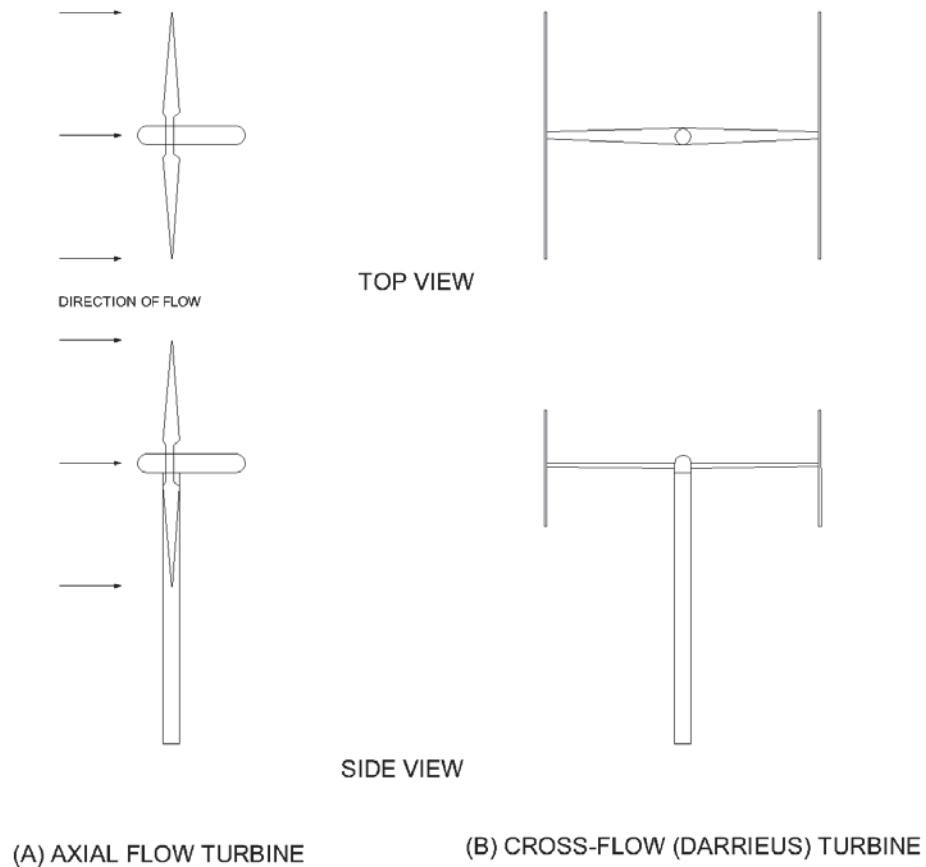


Figure 2.19- Two types of rotor blade configuration.

2.6.1 Axial Flow Rotor Blade Design

The geometric design of a rotor blade has been reported wherein aerodynamic design codes, PROPID and PROPGA (Bir & Migliore, 2004) are developed and used to determine the blade chord, twist, and airfoil shape variation along the span. The codes generate the chord and twist distributions for the given blade with respect to length. The PROPID code was used by the US National Renewable Energy Laboratory (NREL) for the aerodynamic design of the rotor blade. Both the PROPGA and PROPID codes are

used to generate the blade chord and twist distributions optimized for minimum cost of energy.

2.7 Hydrodynamics

2.7.1 Wind Turbine Operation Modeling Using CFD

Efficiency is one of the most important parameters in energy conversion devices. CFD modeling is capable of simulating a wind turbine farm with in-situ conditions in order to evaluate the efficiency of the technology. The NREL performed a benchmarking exercise using CFD to model a wind turbine in an Unsteady Aerodynamics Experiment (UAE) (Hartwanger & Horvat, 2008). Two dimensional blade sections are used to obtain the necessary data input to construct a 3D CFD model of a turbine. The results from the 3D experiment were used to develop estimates for actuator disk induction factors. These factors were used to modify the conventional actuator disk of wind turbines. The CFD modeling to test and analyze the performance of a marine current turbine is similar to that used for wind turbine models.

Turbine Performance Evaluation using CFD Model vs. Experimental Results

Use of CFD to model a wind turbine or ocean current turbine requires accurate aerofoil data. CFD modeling lacks the required tools to predict the performance of a wind turbine in post stall conditions. A 3D CFD analysis was done on the UAE turbine using a turbine blade designed from an S809 aerofoil section. Figure 2.20- S809 Aerofoil section. shows a typical section of the aerofoil used in the UAE turbine model.

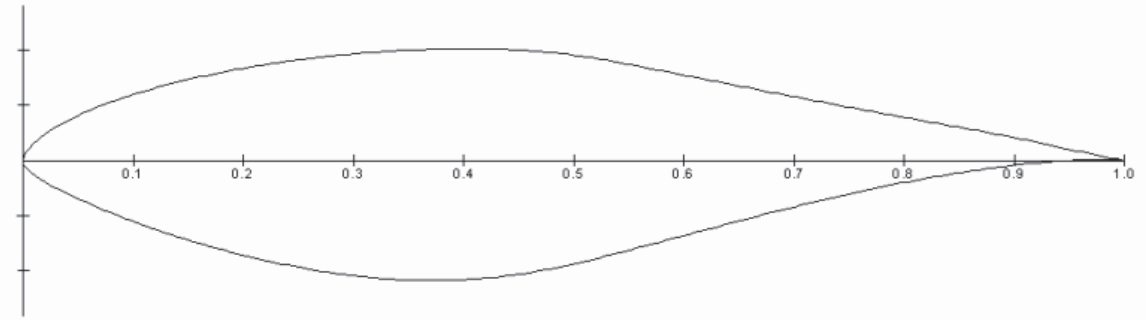


Figure 2.20- S809 Aerofoil section.

Results of 2D experiments were compared with those from an XFOIL 6.0 panel code, and two ANSYS-CFX CFD analyses. This comparison was done to determine the predictive accuracy of the numerical tools in terms of 2D lift and drag.

The CFD model is created using three inflation layers to resolve near wall boundary conditions. The CFD modeling was done using ANSYS-CFX 11.0 while the mesh was created using ANSYS ICEM CFD. The blade was designed using NREL S809 aerofoil in Rhinoceros 3D with a constant pitch angle. Figure 2.21 shows the turbine blade.

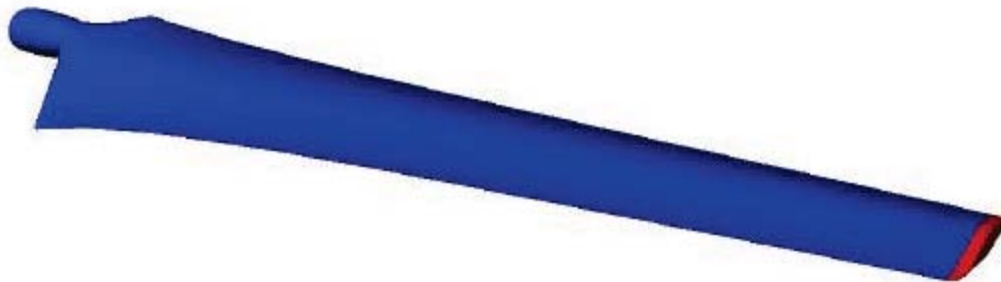


Figure 2.21- UAE turbine blade constructed in Rhinoceros CAD.

After approximately 1000 iterations, the steady state solution converged using the CFX Frozen-Rotor model with a timescale factor of 1. A total pressure inlet and static pressure outlet were used for this model. The measured torque and generated power are compared with the experimental results to validate the CFD model. Figure 2.22 and Figure 2.23 show the measured torque output and generated power of the UAE turbine.

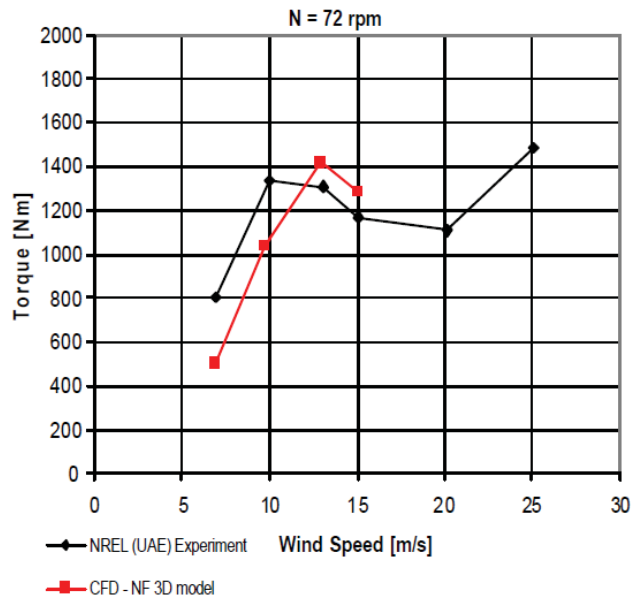


Figure 2.22- Measure Torque Output comparing the results between CFD and experiment.

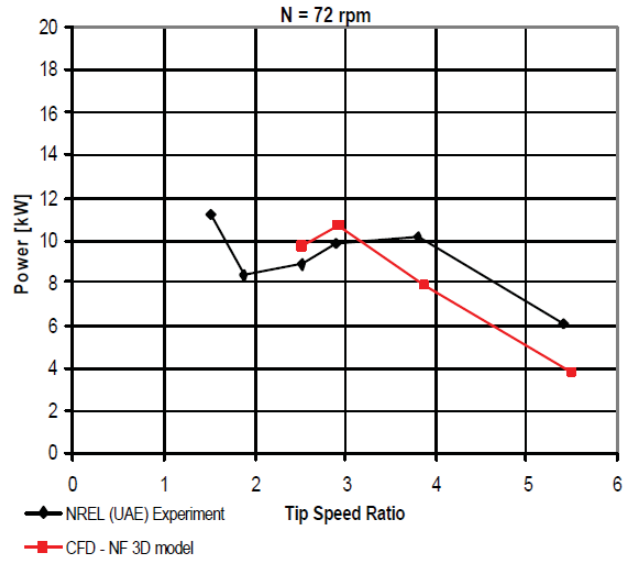


Figure 2.23- Measured power output comparison between CFD and experiment

The torque generated from the CFD model is compared with the NREL UAE experiment based on the actuator disk theory. Figure 2.24 shows the results.

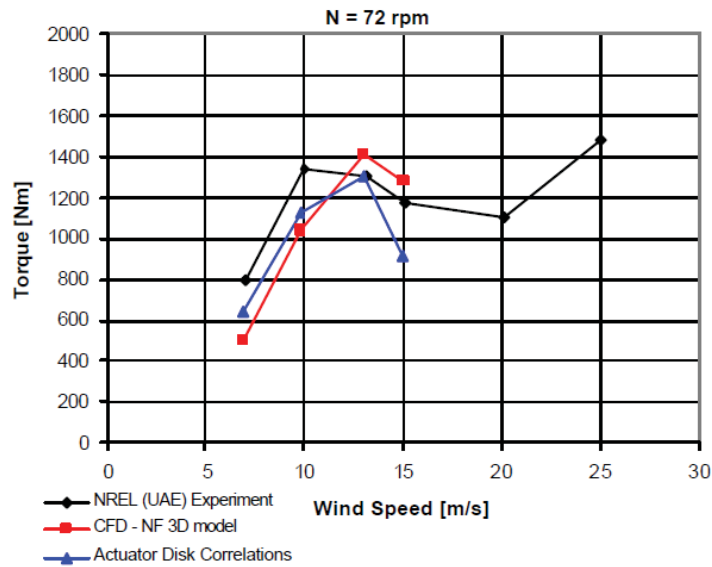


Figure 2.24- Torque distribution calculated from the measured angular induction factor.

2.7.2 Marine Turbine Operation Modeling Using CFD

Prediction of Far Wake of a Horizontal Axis Marine Current Turbine

The effect on far wake due to marine current turbines has been studied by (Harrison, et al., 2009). The thrust coefficient based on an ANSYS CFX model is compared with the experimental data obtained from actuator disks. The objective was to verify that the wake generated from a CFD simulation follows characteristics similar to porous disks for a range of C_T values.

Experimental data was collected at the University of Southampton by measuring the velocity downstream at different distances to examine the wake effects from 0.1 m -diameter discs with varying porosity and compared with results from the CFD model based on ANSYS CFX 11. The model used a hybrid of the finite volume and finite difference discretization methods. The results showed that when $C_T \approx 0.8$ the model gives reasonable agreement with the experimental results. The wake recovered to about 0.9 of the free stream velocity at a downstream distance of $20D$. At the centerline along the rotor axis, the velocity decreases to 0.45 of free stream at a downstream distance of $4D$. The two models showed convergence of C_T at a distance $6D$ downstream (Harrison, et al., 2009).

2.7.3 Wave Current Interactions

Blade element momentum (BEM) theory is frequently used for the prediction of torque and thrust in a marine current turbine. The results from the theory along with linear wave theory, particle velocities and acceleration were compared with wave-current

interaction experimental data for a 400-mm diameter rotor model (Barltrop, et al., 2007). Parametric studies are conducted to evaluate the effects of changing wave height, frequency, and tip-speed ratio. The tests are carried out by the experimental setup using a deep-wave tow tank at the Universities of Glasgow and Strathclyde. Figure 2.25 shows the comparison of experimental values with simulated results for thrust and torque in still water. Figure 2.26 shows a similar comparison for waves 150 mm high propagating at a frequency of 0.50 Hz .

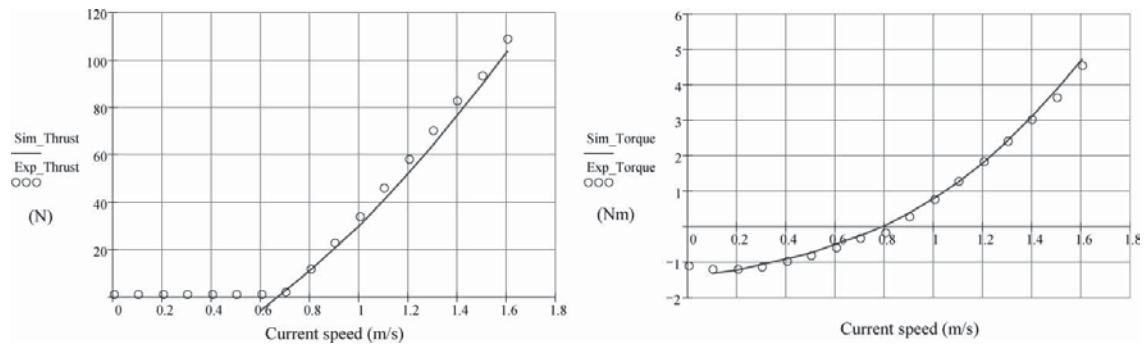


Figure 2.25- Thrust and Torque curves in still water at 200r/min.

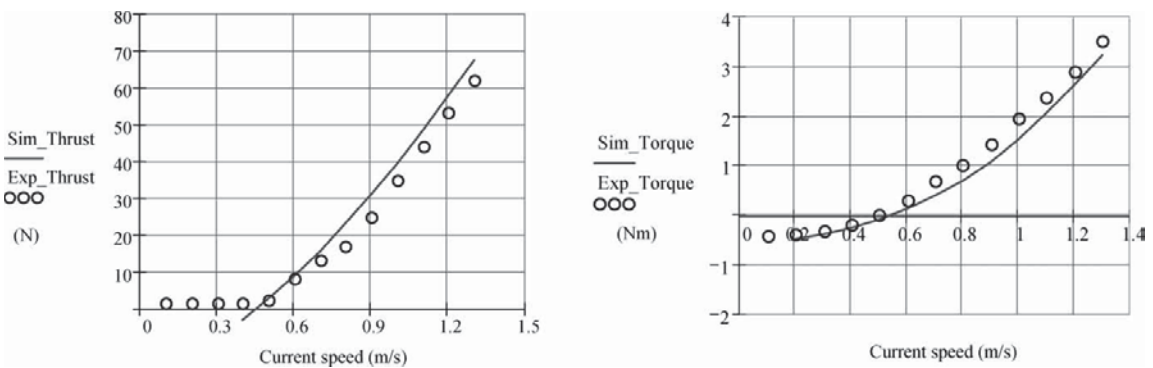


Figure 2.26- Thrust and torque curves in $H = 150\text{ mm}$ and $f = 0.50\text{ Hz}$ at 150 r/min.

The effects of wave frequency on the mean torque and thrust are also compared in Figure 2.27.

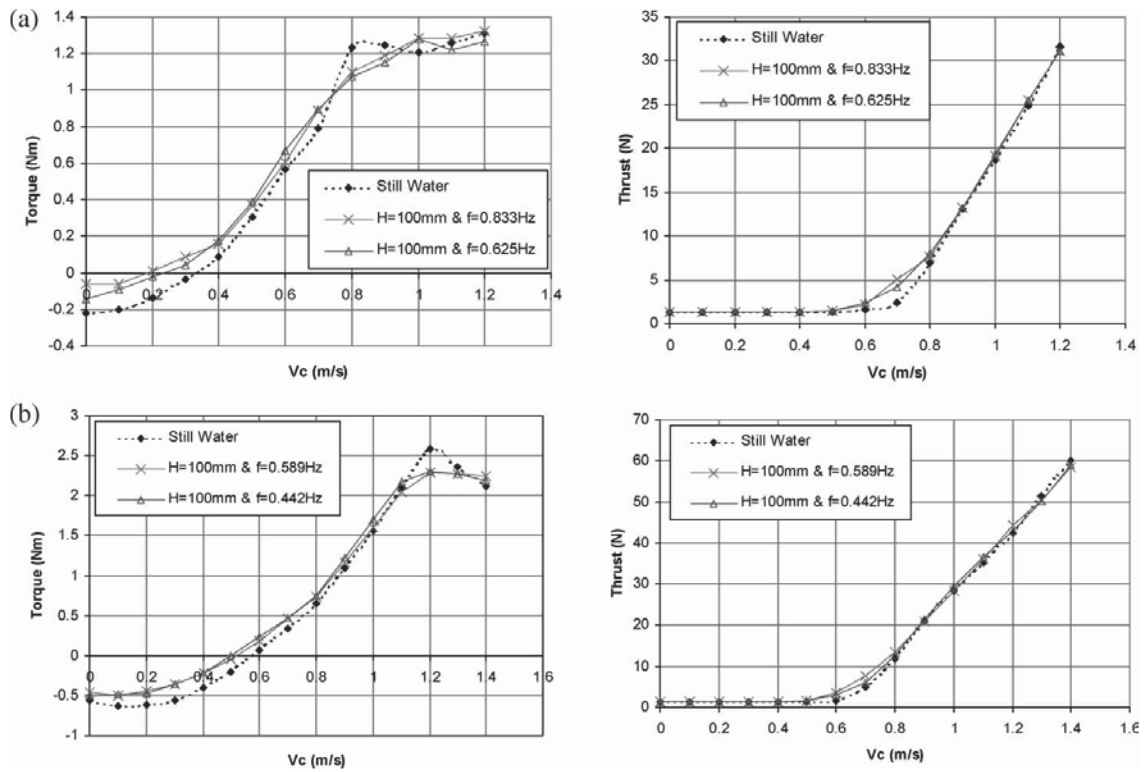


Figure 2.27- Effects of wave frequency on mean torque and thrust when rotor rotates at
 (a) 90 r/min and (b) 127 r/min.

CHAPTER 3

TRANSIENT, INCOMPRESSIBLE AND TURBULENT FLUID FLOW

3.1 Introduction

This chapter describes the theoretical models in ANSYS FLUENT that are useful for modeling the operation of a marine current turbine. The choice of the models will depend on the flow characteristics present at the specific site chosen in the present study. Based on these characteristics and boundary conditions, different types of turbulence flow models are considered. The necessary formulations for each of the applicable models are discussed in detail in the following sections.

This chapter presents details of multiphase flow models. These models simulate inflow in a discretized domain and rotor blade constructed in *SolidWorks* and *ANSYS ICEM CFD* using tetrahedral volume meshing. The multiphase flow model idealizes two or more fluid phases in the simulation of the solid-liquid-gas interface.

The multiphase flow model uses two methods of computation: the Euler-Euler approach and the Euler-Lagrange approach. The Euler-Euler approach is the only applicable model since it has the capability of modeling water flow in an open channel where the ratio of water present at the inlet and to that at the outlet can be specified. The Euler-Lagrange method is mostly suited for simulating sprays of dispersed liquids in a gaseous environment. Within the multiphase flow model, three sub-models are available:

the Volume of Fluid (VOF), Mixture, and Eulerian models. The VOF model is preferred in this study to model the open channel flow. Current flow in the ocean can be modeled using open channel flow where waves and wind velocity effects are important. The equations in the VOF model are expressed in raw form, and the notation and physical meanings are given in Sections 3.4 and 3.5. The Mixture and Eulerian models are not used in the present study because they do not allow the modeling of the flow in open channels.

3.2 Flow Characteristics

A compressible fluid is one in which the fluid density changes when the fluid is subjected to high pressure-gradients. The molecules of compressible fluids do not have the ability to bounce back to their original density and are, therefore, easily compacted or compressed. An incompressible fluid maintains constant density throughout and cannot be compacted easily. Most liquids are incompressible fluids, while gaseous fluids can be either compressible or incompressible depending on the fluid density and the surrounding conditions. For most theoretical and experimental applications, gases are assumed to be incompressible when they are moving at speeds under *220 miles per hour (mph)* (Garber, 2009). The key difference between compressible and incompressible flow is the way by which the external forces are transmitted through the fluid in a pipe. In a compressible fluid, the imposition of a force at one end of a system does not result in an immediate flow throughout the system. Instead, the fluid compresses near where the force is applied; that is, its density increases locally in response to the force. The compressed fluid expands against neighboring fluid particles causing the neighboring fluid itself to

compress and setting in motion a wave pulse that travels throughout the system. The pulse of higher density fluid takes some time to travel from the source of the disturbance down through the pipe to the far end of the system.

The wave-pulse mechanism of momentum transfer is a different kind of molecular momentum transfer that needs to be included in the momentum balances. The total stress tensor Π is given by Eqn. (3.2.1) as follows:

$$\Pi = pI + \tau \quad (3.2.1)$$

Where p is the static pressure, I is the unit tensor, and τ is the extra stress tensor. Π is the quantity that contains a mathematical expression for all the molecular processes that affect stress generation in the flow, and it is here that new terms are needed for the microscopic equations of change to properly model compressible flow. Herein, for Newtonian fluids, the extra stress tensor τ is given by a simple expression that is valid for all flows:

$$\tau = -\mu\gamma \quad (3.2.2)$$

Equation (3.2.2) shows the Newtonian constitutive equation for incompressible fluids. (Morrison, 2004) where μ is the molecular viscosity of the liquid and γ is the ratio of the heat capacity at constant pressure to the heat capacity at constant volume. A measure of the compressibility of a fluid can be taken by finding the Mach number (M). This number is a dimensionless quantity calculated based on the fluid velocity and the way the sound travels inside the fluid. Equation (3.2.3) shown below gives the formulation of M in terms of available data:

$$M = \frac{v}{c} (1.4 \times 10^{-4}) \quad (3.2.3)$$

Where v is the velocity of fluid flow, and c is the velocity of sound travelling through the fluid. Based on Eqn. (3.2.3), the flow can be considered to be subsonic when $M < 1$, transonic when $0.8 < M < 1.2$, supersonic when $M > 1$, and hypersonic when $M > 5$. The fluid may be taken as incompressible when:

$$\frac{1}{2}M^2 \ll 1(1.4 \times 10^{-5}) \quad (3.2.4)$$

In theory, the flow of water under atmospheric pressure can be treated as incompressible flow.

3.3 Computational Fluid Dynamics

Computational fluid dynamics (CFD) is the science of predicting fluid flow, heat and mass transfer, chemical reactions, and related phenomena by solving numerically the set of governing mathematical equations such as the conservation of mass, momentum, energy and species, effects of body forces and continuity. The results obtained from a CFD study can be used to develop prototypes of new designs, test existing fluid-structure interactions and examine the defects of a system in order to be able to redesign that system adequately and accurately. The CFD method focuses on the user defined specific aspects of a given problem. Therefore, CFD reduces the total effort and cost associated with standard testing methods and data acquisition (ANSYS, Inc. Proprietary, 2009). ANSYS FLUENT provides comprehensive modeling capabilities to various forms of CFD modeling. It allows for the analysis of incompressible or compressible flows, laminar or turbulent flow as well as transient or steady-state analysis.

3.4 Basics of Fluid Flow in ANSYS FLUENT

When modeling all types of fluid flow, ANSYS FLUENT solves conservation equations for mass and momentum. The equation for conservation of mass also known as the continuity equation is valid for incompressible as well as compressible flows. The general form for continuity is shown in Eqn. (3.4.1) as follows:

$$\frac{\partial \rho}{\partial t} + \nabla \cdot (\rho \vec{v}) = S_m \quad (3.4.1)$$

Where the source S_m is the mass added to the continuous phase from the dispersed second phase and any user-defined sources, \vec{v} is the velocity vector, ∇ is the partial derivative operator and ρ is the fluid density. Herein, the continuous phase refers to the air and the flowing fluid (water) is taken to represent the dispersed second phase.

The equation for conservation of momentum in a stationary reference frame is given by Eqn. (3.4.2) as follows:

$$\frac{\partial}{\partial t} (\rho \vec{v}) + \nabla \times (\rho \vec{v} \vec{v}) = -\nabla p + \nabla \times (\vec{\tau}) + \rho \vec{g} + \vec{F} \quad (3.4.2)$$

Where p is the static pressure, $\vec{\tau}$ is the stress tensor, and $\rho \vec{g}$ and \vec{F} are the gravitational body force and external body forces respectively. Body forces are caused by the interaction with the dispersed phase. $\vec{\tau}$ is given by Eqn. (3.4.3) as follows:

$$\vec{\tau} = \mu \left[(\nabla \vec{v} + \nabla \vec{v}^T) - \frac{2}{3} \nabla \times \vec{v} I \right] \quad (3.4.3)$$

Where μ is the molecular viscosity, I is the unit tensor, and the second term on the right hand side refers to the effect of volume dilation. (ANSYS, Inc., 2010, pp. 1-4)

3.5 Multiphase Flow

ANSYS FLUENT has the capability to model free surface. The multiphase flow regimes can be used to model: gas-liquid, gas-solid, liquid-liquid, solid-liquid, and three phase flows for infinite number and types of boundary conditions. ANSYS FLUENT uses the volume-of-fluid (VOF) model, Mixture and Eulerian models, as well as the Discrete Phase Model (DPM). Examples of multiphase flows include open channel flows in the ocean, sprays, sedimentation, separation, and cavitation. (ANSYS, Inc., 2010, pp. 1-4,455).

When modeling multiphase flows, ANSYS FLUENT solves transport equations for two types of scalar: *per phase* and *mixture*. For an arbitrary k scalar in *phase-l*, denoted by ϕ_l^k , ANSYS FLUENT solves the transport equation inside the volume occupied by *phase-l* given by Eqn. (3.5.1) below:

$$\frac{\partial \alpha_l \rho_l \phi_l^k}{\partial t} + \nabla (\alpha_l \rho_l \vec{u}_l \phi_l^k - \alpha_l \Gamma_l^k \nabla \phi_l^k) = S_l^k \quad k = 1, \dots, N \quad (3.5.1)$$

Where α_l , ρ_l , and \vec{u}_l are the volume fraction, physical density, and velocity of *phase-l*, respectively. Γ_l^k and S_l^k are the diffusion coefficient and source term, respectively, which is user specific. The variable l could be used to denote single or multi phase flow. The scalar ϕ_l^k is associated only with one phase (*phase-l*) and is considered as an individual field variable of *phase-l*.

Equation (3.5.2) gives the mass flux for *phase-l* defined as:

$$F_l = \int_s \alpha_l \rho_l \vec{u}_l d\vec{S} \quad (3.5.2)$$

A mixture of phases, ϕ^k can be used in applications where the transport variable described by scalar ϕ_l^k , represents the physical field that is shared or considered to be the same for each phase. Equation (3.5.3) shows the generic transport equation for the scalar in the mixture phase:

$$\frac{\partial \rho_m \phi^k}{\partial t} + \nabla(\rho_m \bar{u}_m \phi^k - \Gamma_m^k \nabla \phi^k) = S^k \quad \text{where } k = 1, \dots, N \quad (3.5.3)$$

Where the mixture density ρ_m , mixture velocity \bar{u}_m , mass flux F_m , and mixture diffusivity for the scalar k Γ_m^k are calculated according to Eqns. (3.5.4a)-(3.5.4d):

$$\rho_m = \sum_l \alpha_l \rho_l \quad (3.5.4a)$$

$$\rho_m \bar{u}_m = \sum_l \alpha_l \rho_l \bar{u}_l \quad (3.5.4b)$$

$$F_m = \int \rho_m \bar{u}_m \cdot d\vec{S} \quad (3.5.4c)$$

$$\Gamma_m^k = \sum_l \alpha_l \Gamma_l^k \quad (3.5.4d)$$

$$S_m^k = \sum_l \alpha_l S_l^k \quad (3.5.4e)$$

In order to calculate diffusivity, individual diffusivities for each material associated with individual phases must be specified (ANSYS, Inc., 2010).

The choice of the general multiphase models for use in a given problem shall be made considering the regimes that describe most accurately the particular flow at hand.

For gas-liquid flows, the following regimes are available for selection:

- Slug flow: This is where large bubbles flow in a continuous fluid.
- Bubbly flow: This occurs when discrete gaseous or fluid bubbles flow through a continuous fluid.

- Droplet flow: This type of flow involves discrete fluid droplets flowing in a continuous gas.
- Stratified/free-surface flow: Here the flow of immiscible fluids can be seen, separated by a clearly-defined interface.

Figure 3.1 shows the different flow regimes that can be modeled using multiphase flow.



slug flow



bubbly, droplet, or
particle-laden flow



stratified/free-surface flow



pneumatic transport,
hydrotransport, or slurry flow



sedimentation



fluidized bed

Figure 3.1- Multiphase flow regimes available in ANSYS FLUENT (ANSYS, Inc., 2010).

Two methods can be used in the calculation of multiphase flows: the Euler-Lagrange approach and the Euler-Euler approach. These approaches are discussed below:

Euler-Lagrange Approach

In the Euler-Lagrangian discrete phase model, Navier-Stokes equations are solved for the continuity of the fluid phase. The dispersed phase is then solved by tracking a large number of particles, bubbles, or droplets through the calculated flow field. Physical quantities such as mass, momentum, and energy can be exchanged between the dispersed phase and the fluid phase. One assumption that the Euler-Lagrange method makes is that the dispersed second phase occupies a low volume fraction in the mixture. The method individually calculates the particle trajectories at specified intervals during the fluid phase calculation. This model is most suited for modeling spray dryers, coal and liquid fuel combustion, and some particle-laden flows, but not suited for applications involving a user defined volume fraction for the dispersed second phase.

The Euler-Euler Approach

The Euler-Euler approach involves treating each phase mathematically as interpenetrating continua. This method uses volume fractions where the volume of one phase when flowing full, cannot be occupied by another phase. Each volume fraction is a continuous function in terms of space and time from which conservation equations are derived for each phase to obtain a set of equations that relates all phases in the model. Using the kinetic theory, these equations are connected using empirical formulation to provide constitutive relations. The present study uses the VOF model which is described in the following section (ANSYS, Inc., 2010, p. 458).

3.5.1 The VOF Model

3.5.1.1 Overview of the VOF Model

The VOF model tracks the surface of an Eulerian mesh. It is designed for two or more immiscible fluids where the position of the interface between the fluids is of interest. Immiscible fluids are those which do not mix. The VOF model uses a single set of momentum equations for the fluids, tracking the volume fraction of each fluid throughout the domain. The VOF model is mostly used for stratified flows, free-surface flows, filling, sloshing, the motion of large bubbles in a liquid, the motion of liquid after a dam breaks, the prediction of jet breakup, and the steady or transient tracking of any gas-liquid interface.

3.5.1.2 Limitations of the VOF Model

The following restrictions apply to the VOF model:

- A pressure-based solver must be used instead of a density-based solver.
- The entire computational domain must be completely filled with at least one phase in the model, as the VOF model does not allow gaps or voids in the fluid flow.
- Only one of the phases can be defined as a compressible ideal gas. However, there is no limitation on using compressible liquids using user-defined functions.
- Stream-wise periodic flow including specified mass flow rate or specified pressure drops, cannot be modeled using the VOF model.

- When using the VOF explicit scheme, the second-order implicit time-step formulation cannot be used.
- The DPM cannot be used with the VOF model when tracking particles, if the shared memory option is enabled.

3.5.1.3 Steady-State and Transient VOF Calculations

The VOF model in ANSYS FLUENT is ideally used to obtain a time-dependent solution. A steady-state VOF formulation is only feasible when the solution is independent of the initial conditions, and there are distinct inflow boundaries for the individual phases. The VOF formulation assumes that the different phases are not interpenetrating, and for each additional phase, the volume fraction can be specified to describe the percentage of fluid in that computational cell. For a controlled volume, the volume fractions for all phases present must add up to unity. As long as the volume fraction is known for each phase at a given cross section, the domains and ranges for all variables and properties are shared by the phases and represent volume-averaged values. Consequently, the variables and properties in any given cell or element are either purely representative of one of the phases, or representative of a mixture of the phases, depending on the volume fraction values. An example for volume fraction α for a given fluid (water) can be given by the following:

$\alpha_{water} = 0$; the cell has no water in it.

$\alpha_{water} = 1$; the cell is full of water.

$0 < \alpha_{water} < 1$; the cell contains the interface between water and one or more other fluids.

Based on the local value of α_{water} , the appropriate properties and variables will be assigned to each control volume within the domain.

In a transient flow model, the governing equations must be discretized for both time and space. The spatial discretization for the transient model is the same as that for the steady state solution. However, for temporal simulations, the governing equations must be integrated over a specified time step.

3.5.1.4 Volume Fraction Equation

In order to track the interface between phases, the solution from a continuity equation for the volume fraction of the phases is used. For the q^{th} phase, the continuity equation has the following form:

$$\begin{aligned} & 1/\rho_q \left[\frac{\partial}{\partial t} (\alpha_q \rho_q) + \nabla \times (\alpha_q \rho_q \vec{v}_q) \right] \\ & = S_{\alpha_q} + \sum_{p=1}^n (\dot{m}_{pq} - \dot{m}_{qp}) \end{aligned} \quad (3.5.5)$$

Where \dot{m}_{qp} is the mass transfer from phase q to phase p and \dot{m}_{pq} is the mass transfer from phase p to phase q . The mass source S_{α_q} is zero by default but a constant or user defined value can be specified for each phase. The volume fraction equation is not solved for the primary phase (air); the primary-phase volume fraction will be computed based on the following constraint given by:

$$\sum_{p=1}^n \alpha_q = 1 \quad (3.5.6)$$

The volume fraction equation (3.5.6) can be solved by either implicit or explicit time discretization.

The Implicit Scheme

The Implicit Scheme in ANSYS FLUENT uses the following standard finite-difference interpolation schemes: QUICK, Second Order Upwind and First Order Upwind, and the Modified High Resolution Interface Capturing (HRIC) schemes. Using these schemes, the face fluxes for all cells can be obtained as described by Eqn. (3.5.7) given by:

$$\frac{\alpha_q^{n+1} \rho_q^{n+1} - \alpha_q^n \rho_q^n}{\Delta t} V + \sum_f (\rho_q^{n+1} U_f^{n+1} \alpha_{qf}^{n+1}) \quad (3.5.7)$$

$$= \left[S_{\alpha_q} + \sum_{p=1}^n (\dot{m}_{pq} - \dot{m}_{qp}) \right] V$$

Where $n + 1 =$ index for the current time step. $n =$ index for previous time step, $\alpha_{qf} =$ face value of the q^{th} volume fraction, computed from the first-order or second-order upwind, modified HRIC, compressive, or the Compressive Interface Capturing Scheme for Arbitrary Meshes (CICSAM) scheme, $V =$ volume of cell, and $U_f =$ volume flux through the face, based on normal velocity. As opposed to the explicit scheme which uses the volume fraction at the previous time step, the implicit scheme uses the volume fraction for the current time step. Multiple iterations are performed for the standard scalar transport equation for the volume fraction at each time step for the secondary phase. Within the implicit scheme, both steady-state and transient flows can be modeled.

The Explicit Scheme

The calculations for the explicit scheme are carried out based on volume fraction values that were computed at the previous time step. Equation (3.5.8) shows the formulation for the explicit scheme:

$$\frac{\alpha_q^{n+1} \rho_q^{n+1} - \alpha_q^n \rho_q^n}{\Delta t} V + \sum_f (\rho_q U_f^n \alpha_{qf}^n) \quad (3.5.8)$$
$$= \left[\sum_{p=1}^n (\dot{m}_{pq} - \dot{m}_{qp}) + S_{\alpha_q} \right] V$$

For interpolation of the fluids near the interface, ANSYS FLUENT uses various schemes to run the calculations: the Geometric Reconstruction scheme, the Donor-Acceptor scheme, the CICSAM, the Compressive and Zonal Discretization Schemes (CZDS), and the Bounded Gradient Maximization (BGM) scheme.

The Geometric Reconstruction scheme is the most desirable approach for a cell located at the interface between two phases. It represents the interface between fluids using a piecewise-linear-approach. As a result of the unstructured mesh being used for this model, the Geometric Reconstruction scheme is most accurate. The method uses a linear slope for the interface between two fluids within any given element. As a result, a simplified approach is used in calculating the volume fraction in each cell.

The donor-acceptor scheme is used when one flowing fluid occupies the entire cell. It uses this cell as the donor of a certain amount of fluid, while the neighboring cell as the acceptor of the same amount of fluid. The amount of fluid transferred is dependent on the amount donated or the capacity of fluid that the accepting cell can hold.

The CICSAM scheme is used primarily for flows with high ratios of viscosities between the phases, and this scheme is not used in the present study.

The compressive scheme consists of the zonal discretization and phase localization compressive schemes which are available for both implicit and explicit formulation in the VOF model. This Immiscible Fluid Model must be activated to model immiscible fluids. The first order upwind scheme is used when the slope limiter value $\beta_{max} = 0$. When $\beta_{max} = 1$, the second order reconstruction bounded by the global minimum/maximum of the volume fraction is selected. When $\beta_{max} = 2$, the scheme is compressive. When $0 < \beta < 1$, blending of the first order and second order compressive schemes is denoted, whilst $1 < \beta < 2$ represents blending of the second order and compressive schemes.

The BGM scheme is used to obtain sharp interfaces with the VOF model similar to that obtained by the Geometric Reconstruction scheme. This scheme is not applicable to transient modeling and hence will not be used in the present study.

3.5.1.5 Fluid Properties

For a two-phase system with air and water, the density in each cell is given by Eqn. (3.5.9) as follows:

$$\rho = \alpha_{water}\rho_{water} + (1 - \alpha_{water})\rho_{air} \quad (3.5.9)$$

This equation forms the basis for calculation of density along with all other fluid properties in each phase of the model. For a two-phase system, the volume-fraction-averaged density has the form given by Eqn. (3.5.10):

$$\rho = \sum_{q=1}^2 \alpha_q \rho_q \quad (3.5.10)$$

3.5.1.6 Momentum Equation

ANSYS FLUENT uses a single momentum equation throughout the computational domain. The resulting velocity field is then used to describe the velocity among both phases. The conservation of momentum is given by Eqn. (3.3.2) in section 3.3. This formulation is dependent on the volume fractions of both phases through the properties of fluid density, ρ and molecular viscosity, μ . This shared-fields method is most useful when there are small velocity differences between the phases. The accuracy of the momentum conservation decreases as these velocity differences become larger. The velocity differences in the phases are represented by the viscosity ratio. Therefore, when this value exceeds 1×10^3 , convergence of solution may occur. The CICSAM scheme is used in order to model this type of flow more accurately. However, the viscosity difference between phases is small for this model.

3.5.1.7 Energy Equation

Since the fluid properties are related by the same general form of conservation equations, the energy equation (3.5.11) has the following form:

$$\frac{\partial}{\partial t}(\rho E) + \nabla \times [\vec{v}(\rho E + p)] = \nabla(k_{eff} \nabla T) + S_h \quad (3.5.11)$$

The energy, E, and temperature, T, are treated as mass-average values. The computation of these averages are achieved by Eqn. (3.5.12) as follows:

$$E = \frac{\sum_{q=1}^n \alpha_q \rho_q E_q}{\sum_{q=1}^n \alpha_q \rho_q} \quad (3.5.12)$$

Where E_q for each phase is based on the specific heat of that phase and the shared temperature. The properties ρ and k_{eff} (effective thermal conductivity) are shared by the phases. The source terms, S_h contain contributions from radiation, as well as any other volumetric heat sources.

Similar to the velocity field, a more accurate solution is formed when the changes in temperature near the interface is limited. For the air-water interface, the change of temperature between the phases is not significant to affect the convergence and precision of the solution.

3.5.1.8 Turbulence

ANSYS FLUENT uses various models to describe turbulent flows. Turbulent flow is a state of flow where the particles do not flow in a linear fashion but rather overlap each other. Osborne Reynolds systematically studied this state of flow using a colored liquid in a glass tube. The colored liquid was allowed to flow into the water filled tube. The liquid flowed linearly without mixing with the surrounding water. This state was labeled laminar flow. Reynolds then gradually opened the valve until the water flow velocity reached a certain value, where the line of colored liquid began mixing with the surrounding water creating the flow phenomenon known as turbulence. The flow velocity at which the laminar flow turned to turbulent flow is called the critical velocity. This critical velocity is achieved when the Reynolds number reaches a certain value given by:

$$Re = \frac{\rho v d}{\mu} \quad (3.5.13)$$

Here, ρ is the density of the fluid, μ is the dynamic viscosity, d is the diameter of the tube, and v is the average velocity. Laminar flow occurs when $Re < 2000$. Transitional flow occurs when $2000 < Re < 4000$, and turbulent flow occurs when $Re > 4000$ (Nakayama, 1999). The turbulence model used in the present study is defined in terms of the turbulent kinetic energy (k), and specific dissipation rate (ω), which can be obtained from the ratio of ε to k , calculated from the following equations (Harrison, et al., 2009):

$$k = \frac{3}{2} I^2 U^2 \quad (3.5.14)$$

Where, I is the turbulence intensity, and U is the free stream velocity

$$\varepsilon = \frac{k^{3/2}}{0.3 D_h} \quad (3.5.15)$$

Where, D_h is the water depth.

The choice of a turbulence model entails the knowledge of the physics of flow, the degree of accuracy desired, the computational resources and governing time constraints. The choice of turbulence models used in the present study is based on the relevance of the model to wind and marine current turbines. Since no single turbulence model is universally accepted as the best model to use, possible candidates are chosen with the capabilities of simulating the rotating aerofoil shape within a flowing fluid. The models are described briefly to give the user an idea of the limitations and computational cost of each:

1. Standard k - ε : This is the simplest two-equation model, proposed by (Launder and Spalding, 1972). It is capable of efficiently modeling fully turbulent

flow to a reasonable degree of accuracy. Improvements on the *Standard k-ε* model lead to the development of models 2 and 3.

2. *Re-Normalization Group (RNG) k-ε*: This model enhances the *k-ε* model to simulate swirling effects on turbulence more accurately. The model is based on Navier-Stokes equations making it more accurate and reliable for a wider range of flows.

3. *Realizable k-ε*: In addition to the previous modeling capabilities, the *Realizable k-ε* has a new formulation for turbulent viscosity and the dissipation rate. This model satisfies certain mathematical constraints of the Reynolds stresses.

4. *Standard k-ω*: This model is designed with the intention to accurately predict far wake, mixing, wall-bounded flows and free shear flows. Previous studies show that the *k-ω* models give the best velocity prediction in centrifugal separators when compared to the *Realizable k-ε* and the *Reynolds Stress Models*.

5. *Shear Stress Transport (SST) k-ω*: This model combines the accuracy of the *Standard k-ω* model at near-wall regions with the far-field independence capabilities of the *k-ε* models. Advantages include a modified turbulent viscosity to aid in the transport of turbulent shear stress. This improves the model's accuracy in flows where negative pressure is seen.

6. *Transition SST*: This model couples the *SST k-ω* model with transport equations for intermittency and transition onset criteria, in terms of momentum-thickness Reynolds number. User-defined empirical correlation can be entered

with the *Transition SST* model. This correlation can be used to control the transition onset momentum thickness Reynolds number equation.

3.5.1.9 Time Dependence

When using time-dependent VOF calculation, ANSYS FLUENT uses Eqns. (3.5.5) and (3.5.6) to solve for the volume fraction using an explicit time-marching scheme. This time step can be modified by changing the Courant number for the system. The Courant-Friedrichs-Lewy condition generally referred to as the Courant number or CFL is a necessary condition for convergence when solving certain partial differential equations. The CFL is determined from Eqn. (3.5.16) given below:

$$C = v \frac{\Delta t}{\Delta y} \quad (3.5.16)$$

Where C is the Courant number, v is the flow velocity and Δt and Δy are the change in time and length along the direction of flow respectively (Cebeci, et al., 2006). The volume fraction can be set to update once for every time step, or once for every iteration within each time step.

3.5.1.10 Surface Tension and Adhesion

Surface Tension

The surface of a liquid has the tendency to shrink causing the free surface molecules to pull against each other to form an elastic film over the fluid. The tensile strength per unit length of the free surface is known as the surface tension (Nakayama, 1999). The surface tension effects at the air-water interface can be modeled using the

VOF model. ANSYS FLUENT allows the customization of this model by specifying the contact angles between the phases and walls and at porous jumps. The surface tension coefficient can be specified as a function of temperature, a user defined function or a constant. In this model, a constant surface tension value will be used due to constant velocity, interface level in both phases and gravity. Variable surface tension coefficients are only important in applications involving negligible gravity. The surface tension coefficients σ for water in contact with air for water temperatures ranging from 0 to 374.1°C are given in Table 3.1 as follows:

Table 3.1- Surface tension of water in contact with air based on water temperature.
(engineeringtoolbox.com)

Temperature T(°C)	Surface tension σ (N/m ²)
0	0.0756
5	0.0749
10	0.0742
20	0.0728
30	0.0712
40	0.0696
50	0.0679
60	0.0662
70	0.0644
80	0.0626
90	0.0608
100	0.0589
150	0.0482
200	0.0376
250	0.0264
300	0.0147
350	0.0037
374.1	0

The solver accounts for minor changes in surface tension throughout the duration of flow and includes additional stress terms to compensate for the change in surface tension, σ .

Surface tension is caused by inter-molecular forces in fluids. These forces act only at interfaces where the two fluids meet. Surface tension opposes the net force exerted by one fluid on the molecules of another fluid, maintaining equilibrium when these two fluids interact. For interfaces that are relatively flat, the surface tension is created to minimize the free energy by reducing the surface area of the interface. ANSYS FLUENT uses the continuum surface force (CSF) model to simulate the surface tension between fluids. This model places a source term, F_{vol} in the momentum equation (3.3.2). In order to describe this source term, Eqn. (3.5.17) can be examined for constant surface tension across a surface. The source term is given by Eqn. (3.5.21). The pressure drop across the surface is calculated from the product of the surface tension and the surface curvature as follows:

$$p_2 - p_1 = \sigma \left(\frac{1}{R_x} + \frac{1}{R_y} \right) \quad (3.5.17)$$

Where p_2 and p_1 are the pressures in the two fluids on either side of the interface, and R_x and R_y are two radii measured along the plane of the interface in orthogonal directions. In ANSYS FLUENT, the CSF model uses local gradients from the surface normal when computing R_x and R_y . The surface normal is calculated by eqn. (3.5.18) as shown below:

$$n = \nabla \alpha_q \quad (3.5.18)$$

Where n is the surface normal, and α_q is the volume fraction of the q^{th} phase.

Equation (3.5.19) shows the formulation for the curvature as:

$$\kappa = \nabla \hat{n} \quad (3.5.19)$$

Where κ , defined according to the divergence of the unit normal, \hat{n} .

Equation (3.5.20) gives the expression for \hat{n} as follows:

$$\hat{n} = \frac{n}{|n|} \quad (3.5.20)$$

The source term, F_{vol} is given by eqn. (3.5.21) and has the following form:

$$F_{vol} = \sum_{pairs\ i,j, i < j} \frac{\alpha_i \rho_i \kappa_j \nabla \alpha_j + \alpha_j \rho_j \kappa_i \nabla \alpha_i}{\frac{1}{2}(\rho_i + \rho_j)} \quad (3.5.21)$$

Where F_{vol} is the volume force at the surface expressed using the divergence theorem as a result of the pressure jump across the surface. For a two-phase model, $\kappa_i = -\kappa_j$ and $\nabla \alpha_i = -\nabla \alpha_j$. Equation (3.5.21) then simplifies to:

$$F_{vol} = \sigma_{ij} \frac{\rho \kappa_i \nabla \alpha_i}{\frac{1}{2}(\rho_i + \rho_j)} \quad (3.5.22)$$

Where ρ is the volume-averaged density computed using Eqn. (3.5.9). This equation shows that the surface tension is computed using the average density in the cell.

Surface tension can sometimes be neglected based on the Reynolds number, Re , and the capillary number, Ca ; or Re and the Weber number, We . These numbers are all dimensionless quantities, and they all affect the importance of surface tension. For $Re \ll 1$, the capillary number must be taken into consideration. Equation (3.5.23) is used to calculate the capillary number as follows:

$$Ca = \frac{\mu U}{\sigma} \quad (3.5.23)$$

Where μ is the viscosity, U is the free-stream velocity and σ is the surface tension.

For $Re \gg 1$, the Weber number needs to be considered. Equation (3.5.24) is used to calculate the Weber number given by:

$$We = \frac{\rho LU^2}{\sigma} \quad (3.5.24)$$

The effects of surface tension can be neglected if $Ca \gg 1$ or $We \gg 1$.

Wall Adhesion

A wall adhesion angle can be used along with the contact angles in the surface tension model to adjust the normal vector to the surface in cells near the wall of the blade. The curvature of the surface near the wall is adjusted so that a boundary condition at the blade wall itself is not needed. The surface normal at the cells adjacent to the rotor blade wall is described by eqn. (3.5.25) as follows:

$$\hat{n} = \hat{n}_w \cos \theta_w + \hat{t}_w \sin \theta_w \quad (3.5.25)$$

Where θ_w is the contact angle at the wall boundary. \hat{n}_w and \hat{t}_w are the normal and tangential unit vectors to the wall respectively. The body force term in Eqn. (3.3.2) is adjusted by the new curvature formulated in this equation, which incorporates the newly calculated contact angle and the normally calculated surface normal in order to determine the local curvature of the surface.

3.5.1.11 Open Channel Wave Boundary Conditions

Open channel wave boundary condition allows the incorporation of waves into the fluid model. This multiphase model is useful to simulate the effects of the turbine operation in the ocean, subjected to current velocity as well as the effects of wave action.

ANSYS FLUENT allows the modeling of waves based on their steepness which is defined as the ratio of wave height to wave length. This parameter is important in

determining which type of wave theory to use in the model. Waves with lower steepness are modeled using smaller amplitude wave theories, whilst waves with greater wave steepness require higher order wave theories. For applications which use infinite liquid height, short gravity wave expressions are used in wave theories whereas shallow or intermediate wave expressions are used when a finite liquid height is used. For the marine application where the depth of the ocean is well over 300 m, short gravity wave expressions are the most applicable method to the theory.

Equation (3.5.26) defines the wave height, H , as follows:

$$H = 2A = A_t + A_c \quad (3.5.26)$$

Where A is the wave amplitude, A_t is the wave amplitude at trough, and A_c is the wave amplitude at the crest. For linear wave theory, $A_t = A_c$ and for nonlinear wave theory $A_t \neq A_c$.

The wave number k , given by Eqn. (3.5.27) has both longitudinal (parallel to direction of flow) and transverse (perpendicular to direction of flow) directions, and given by Eqns. (3.5.28a) and (3.5.28b) respectively:

$$k = \frac{2\pi}{\lambda} \quad (3.5.27)$$

$$k_x = k \cos \theta \quad (3.5.28a)$$

$$k_y = k \sin \theta \quad (3.5.28b)$$

Where λ = wavelength, θ is the wave heading angle between the wave front and the flow direction in both the longitudinal and transverse directions of flow.

The wave frequency ω is an important parameter in determining the extent of subsurface effects that will occur as a result of the presence of waves and given by:

$$\omega = \frac{1}{T} \quad (3.5.29)$$

Where T is the wave period in seconds.

The effective wave frequency is defined by eqn. (3.5.30) as follows

$$\omega_e = \omega + k_x V \quad (3.5.30)$$

Where V is the velocity magnitude parallel to the direction of flow.

The wave speed celerity c is another important parameter in wave theory, and Eqn. (3.5.31) describes the calculation of c as follows:

$$c = \frac{\omega}{k} \quad (3.5.31)$$

The wave velocity can then be expressed in a vector form by Eqn. (3.5.32) as follows:

$$\vec{V} = (V + v)\hat{y} + u\hat{x} + w\hat{z} \quad (3.5.32)$$

Where u , v , and w are the velocity components of the surface gravity wave in the \hat{x} , \hat{y} , and \hat{z} directions, respectively. Here y is in the direction of flow.

Two theories for wave analysis are provided in ANSYS FLUENT to model gravity waves. These theories are only available through the velocity inlet boundary condition:

- First order Airy wave theory
- Higher order Stokes wave theory

Airy Wave Theory

The first order Airy wave theory gives the wave profile, $\zeta(X, t)$, for a linear wave in Eqn. (3.5.33) as follows:

$$\zeta(X, t) = A \cos \alpha \quad (3.5.33)$$

Where α is the given by Eqn. (3.5.34) as follows:

$$\alpha = k_x x + k_y y - \omega_e t + \varepsilon \quad (3.5.34)$$

Where x and y are the space coordinates in the longitudinal and transverse flow directions, respectively, ε is the phase difference and t is the time. Within the Airy wave theory, the wave frequency takes on a different formulation than the conventional method involving the period as shown in Eqn. (3.5.29). Equations (3.5.35) and (3.5.36) shows the formulation for wave frequency for shallow/intermediate waves, and gravity waves, respectively as follows:

$$\omega = \sqrt{gk \tanh(kh)} \text{ for shallow or intermediate waves.} \quad (3.5.35)$$

$$\omega = \sqrt{gk} \text{ for short gravity waves.} \quad (3.5.36)$$

Where h is the liquid height, k is the wave number, and g is the gravitational constant. The velocity components for both intermediate and gravity waves are described for the incident wave boundary condition as follows:

- Velocity components for shallow/intermediate waves:

$$\begin{pmatrix} u \\ v \end{pmatrix} = \frac{gkA}{\omega} \frac{\cosh[k(z+h)]}{\cosh(kh)} \begin{pmatrix} \cos \theta \\ \sin \theta \end{pmatrix} \cos \alpha \quad (3.5.37)$$

$$w = \frac{gkA}{\omega} \frac{\sinh[k(z+h)]}{\cosh(kh)} \sin \alpha \quad (3.5.38)$$

- Velocity components for short gravity waves:

$$\begin{pmatrix} u \\ v \end{pmatrix} = \frac{gkA}{\omega} e^{kz} \begin{pmatrix} \cos \theta \\ \sin \theta \end{pmatrix} \cos \alpha \quad (3.5.39)$$

$$w = \frac{gkA}{\omega} e^{kz} \sin \alpha \quad (3.5.40)$$

Where z is the height from the free surface level in the \hat{z} direction opposite to the direction of gravity.

Stokes wave theories are used for higher order formulation (the second to the fifth order). Equation (3.5.41) shows the generalized expression for wave profiles as follows:

$$\begin{aligned}\zeta(X, t) = & A \cos \alpha + A^2 k (b_{22} + A^2 k^2 b_{24}) \cos 2\alpha \\ & + A^3 k^2 (b_{33} + A^2 k^2 b_{35}) \cos 3\alpha \\ & + A^4 k^3 b_{44} \cos 4\alpha + A^5 k^4 b_{55} \cos 5\alpha\end{aligned}\quad (3.5.41)$$

For Stokes wave theories, the wave frequency ω is given by eqn. (3.5.42) as follows:

$$\omega = [gk(1 + A^2 k^2 c_3 + A^4 k^4 c_5) \tanh kh]^{\frac{1}{2}} \quad (3.5.42)$$

Where c is the wave speed and g is the magnitude of gravitational constant.

The velocity components for surface gravity waves are computed by Eqn. (3.5.43 a-c) as follows:

$$u = \frac{\partial \phi}{\partial x} \cos \theta \quad (3.5.43a)$$

$$v = \frac{\partial \phi}{\partial x} \sin \theta \quad (3.5.43b)$$

$$w = \frac{\partial \phi}{\partial z} \quad (3.5.43c)$$

In order to know which of the models (Airy or Stokes) is best suited for the specific application, first the Ursell number Ur shall be computed. For nonlinear waves,

the Ursell number assumes the waves to be single-crested, having no secondary crests at the trough. As wave steepness increases, waves tend to assume a nonlinear pattern. With higher order theories involving second and fourth order terms, there is a greater chance of having secondary crests. Hence, the choice of the ideal wave theory depends on important parameters relating to the wave breaking limit.

For shallow/intermediate waves within the wave breaking limit, the following conditions should be met:

- Maximum wave height to depth ratio $\left(\frac{H}{h}\right)_{max} = 0.78$
- Maximum wave height to wave length ratio within breaking limit for linear waves $\left(\frac{H}{\lambda}\right)_{max} = 0.0625 \tanh\left(2\pi \frac{h}{\lambda}\right)$
- Maximum wave height to wave length ratio within breaking limit for nonlinear waves $\left(\frac{H}{\lambda}\right)_{max} = 0.142 \tanh\left(2\pi \frac{h}{\lambda}\right)$

The Ursell number is then given by eqn. (3.5.44) as follows:

$$Ur = \frac{H\lambda^2}{h^3} \quad (3.5.44)$$

For linear waves, $Ur < \frac{32\pi^2}{3}$, and for nonlinear waves, $Ur < \frac{8\pi^2}{3}$.

For short gravity waves within the wave breaking limit, the following conditions should be satisfied:

- The minimum water height to wave length ratio $\left(\frac{H}{\lambda}\right)_{min} = 0.5$
- The maximum wave height to wave length ratio for linear waves $\left(\frac{H}{\lambda}\right)_{max} = 0.0625$

- The maximum wave height to wave length ratio for nonlinear waves $\left(\frac{H}{\lambda}\right)_{max} = 0.142$

As a result, the wave height to water depth ratio $\left(\frac{H}{h}\right)_{max} = 0.78$. For short gravity waves, the Ursell number stability criterion is automatically satisfied for both linear and nonlinear wave theories (ANSYS, Inc., 2010).

3.5.2 The Mixture Model

The Mixture Model is a simplified procedure to model multiphase flows. It can be used to model multiphase flows where each phase moves at a different velocity while maintaining local equilibrium over short spatial length scales. The mixture model can be used to model homogeneous flows where coupling occurs and the velocity is constant throughout the multiphase model. The model uses the mixture equations to calculate non-Newtonian viscosity. The mixture model is feasible when a simplified solution is desired in cases where there is a wide distribution of the particulate phase or when the interphase laws are unknown. As opposed to the full multiphase model, the mixture model is not suitable for accurate modeling of gas-liquid interfaces where open channel conditions and waves are present. As a result, the mixture model is not considered in the present study (ANSYS, Inc., 2010).

3.5.3 The Eulerian Model

The Eulerian model is used for multiple separate phases which are in contact with each other. This model can be used for a combination of any or all of the three phases of matter, using an Eulerian treatment for each phase instead of a discrete phase model as in

the case of the Euler-Lagrangian model. This model is well suited for modeling any number of phases; however, this model does not incorporate the effects of waves and open channel flow and hence cannot be used in this study (ANSYS, Inc., 2010).

3.6 The Finite Element Method

The CFD solvers used by ANSYS are based on the finite volume method. The finite volume method discretizes the specific computational domain into a finite number of control volumes with the general shape of each element defined by the user (ANSYS, Inc. Proprietary, 2009). Discretization involves dividing the computational domain and all of its components into an equivalent system of finite elements with associated nodes, and choosing the most appropriate element type to closely model the actual physical behavior (Logan, 2007). The total number of elements is based upon the engineering application and dependent on the particular location within the domain. Smaller size elements are used in locations where refined analysis is needed. These locations are determined by curvature and proximity to the blade structure, and the size of elements exponentially increases outward from these locations. Two-dimensional elements are typically used to model plane stress or plane strain applications. The benefit of using simple three-dimensional elements is to represent a three-dimensional stress state along with higher-order three-dimensional elements with intermediate nodes along the edges. The most common three-dimensional elements are tetrahedral and hexahedral elements. These elements have four corner nodes and straight sides and can be easily interlocked into a grid to form large bodies. The nodes are numbered in a manner so as to avoid the

calculation of negative volumes. It must also be consistent with counterclockwise node numbering associated with the constant strain triangular element (Logan, 2007).

3.7 Blade Element Momentum Theory

The generated torque, thrust, and bending moments from a stream flow can be calculated using linear blade element momentum theory (Bartrop, et al., 2006). A blade with varying chord and pitch or twist angles is analyzed by dividing each blade into sections and assuming these values to be constant throughout each section. The velocity of water flow past each blade section is then calculated based on the effects of current velocity with the presence of waves. Lift and drag coefficients are calculated as functions of incident angles on the blades, then adjusted to account for three-dimensional effects. The wave frequency is affected by the current speed as seen in Eqn. (3.7.1) below,

$$f_e = \frac{1}{T_e} = \frac{1}{T_w} + \frac{U_c}{L_w} \cos(\theta_w) \quad (3.7.1)$$

Where T_e and T_w are the encountered and wave period respectively, L_w is the wave length, U_c is the current speed and θ_w is the incident angle of wave. Waves mainly cause the change of the velocity field and pressure field around the rotor. The velocity field affects the fluid forces on the rotor while the pressure field determines the inception of cavitation. The extent to which the waves affect the rotor is dependent on the magnitude and direction of the flow velocity caused by the wave motion. This flow velocity has two components: horizontal wave particle velocity and vertical wave particle velocity. Increase in the horizontal wave particle velocity will increase the incident flow velocity if acting in the same direction as the current while decreasing this velocity if acting in the

opposite direction of the current. Vertical wave particle velocity affects the total flow velocity around the turbine as well as the flow incidence angle resulting in the modification of the lift and drag coefficients and forces. Periodical forces result on the rotor when regular waves are present. These forces decrease when the turbine is positioned deeper in the water. Wave effects are neglected when the wave propagation speed is significantly less than the current speed.

3.8 Principles of Similitude

The laws of physics can depend on the ratio of known quantities of the same type (Assis, 2004). Proportioning factors can be derived to scale a prototype model to its representative full scale model using these laws. For the present study, results reported from literature are scaled to obtain an accurate comparison between the simulated results to previously published data. The scale factor for the thrust is given by Equation 3.8.1 below (Harris & Sabnis, 1999):

$$S_T = S_\sigma S_l^2 \quad (3.8.1)$$

Where S_T is the scale factor for thrust, S_σ is the proportion factor for the stress and S_l is the ratio of the model rotor diameter to the full scale rotor diameter. For torque comparison, the scale factor, S_Q for torque is given by Eqn. 3.8.2.

$$S_Q = S_\sigma S_l^3 \quad (3.8.2)$$

For generated power, provided that the velocity remains the same for the prototype and the model, the scale factor for thrust is the same as the scale factor for power.

CHAPTER 4

NUMERICAL SIMULATION OF WAVE-CURRENT INTERACTIONS IN FULL-SCALE MARINE CURRENT TURBINE ROTOR BLADES

4.1 Introduction

This chapter presents the mathematical simulation of wave-current interactions in marine current turbine (MCT) rotor blades. The simulation considers multiphase flow involving open channel flow with wave boundary conditions. The model uses a three-dimensional rotor blade constructed using *SolidWorks* by means of connecting cross-sectional curves. An adequate computational domain is created, and both the domain and the 3D blade are meshed using ANSYS ICEM CFD. The meshed geometry is then given as input into ANSYS FLUENT to perform the CFD simulations.

Before performing the fluid flow computations, it is necessary to understand the metaocean environment. Information on the environmental site assessment performed by SNMREC is used to describe the prevailing conditions at the site, off the coast of Ft. Lauderdale, Florida. The site assessment includes the present and historical information about the ocean and the metaocean conditions. Some of the characteristics included in this site assessment are the fluid properties, characteristics and magnitudes of flow.

The properties of the flowing fluids that are present on the specific site need to be determined prior to the numerical simulation. The data provided by the SNMREC for

current velocity, ocean temperature, and salinity are used in this study to determine the variable density along the ocean depth. The current velocity profile of the ocean with respect to depth is used to determine the optimum depth for deployment of the marine current turbine. Upon choosing the turbine location and depth, the turbine rotor blade is created in *SolidWorks* using preliminary structural design information for the composite blades reported by the National Renewable Energy Laboratory (NREL) (Migliore, 2004). The turbine has a total rotor diameter of 43.2m. The computational domain is formed based on a specific current velocity profile and the published data from (Reza, 2010) on the wake effects caused by the blade rotation. Based on this information, the extents of the domain are chosen to be 20m before and 100m after the plane of rotation. Once the blade geometry and computational domain are meshed using ANSYS ICEM CFD, the model is imported into ANSYS FLUENT where the CFD analyses are carried out.

The analyses are performed using multiphase flows. The volume of fluid multiphase flow model is used to model open channel flow with wave boundary conditions. The pressure, velocity, and volume fraction from the CFD analyses are used in the calculation of the power, thrust, and torque.

4.2 Physical Properties of Fluids

The density of pure water is 1000 kg/m^3 at standard atmospheric temperature and pressure. Depending on the level of salinity and temperature, the density of ocean water can vary above or below that of pure water. At the surface, the density of ocean water can be taken to be $1,027 \text{ kg/m}^3$. Increasing salinity and decreasing temperature

cause the ocean water to become denser. Because less dense water floats above the denser water, higher water temperatures are seen at or near the surface of water bodies. Due to the more significant effect of temperature on the density of water, water with higher salinity can float above water with less salinity, if the higher salinity water is sufficiently warmer than the lower salinity water.

The temperature in the ocean decreases with increasing depth from the surface causing the densest water to be located at the ocean floor. The movements of ocean currents tend to be horizontal due to the movement of water along layers with the same density. In order to measure the density of ocean water, a laboratory experiment must be conducted on a sample obtained from the field. As a result of the impracticability of this method for collecting data throughout the ocean depth, the density profile for most oceans is calculated using salinity, temperature and pressure (Bergman, 2001). A Conductivity-Temperature-Depth (CTD) instrument is commonly used to obtain the data on salinity and temperature. The equipment setup on the NOAA's *Ocean Power* vessel is shown in Figure 4.1 below.



Figure 4.1- CTD Instrument setup onboard the Ocean Power preparing to collect data for temperature and salinity (Leland, 2009, p. 32).

These data were collected by the Southeast National Marine Renewable Energy Center at Florida Atlantic University. Oceanographic data were measured and recorded using the Sea Bird Electronic's *SBE 9plus* CTD. This CTD has the capability of measuring altitude above the seafloor, conductivity, salinity, oxygen, temperature, pH, density, and pressure with respect to depth in waters as deep as 6,800 *m*. The CTD is operated by lowering the instrument at a rate of 1*m/s* to a depth of 10*m* above the sea floor using a steel armored coaxial cable which communicates between the onboard computer on the ship and the instrument. The CTD contains a pump which is switched on before lowering and raising of the instrument. The pump has a constant flow rate of 100 *ml/s* so that the sensor response times are independent of the lowering rate. Data is collected while the instrument is being lowered as well as during the upward journey. (Leland, 2009). Figure 4.2 shows the temperature profile off the coast of southeast

Florida. The highest temperature at the surface is seen to be 30°C or 86°F. The lowest temperature of 9°C or 48°F is observed to be at the greatest depth near the ocean bottom.

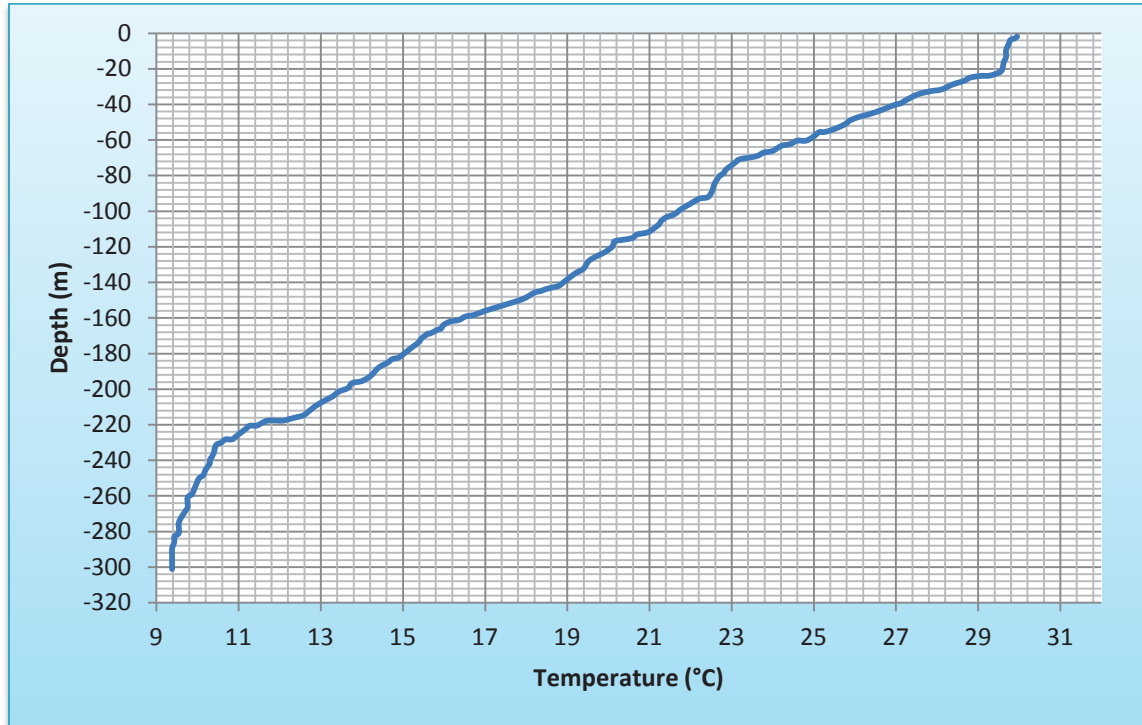


Figure 4.2- Temperature-depth plot from the data collected by the CTD instrument offshore the coast of Ft. Lauderdale, Florida.

The other important parameter is the salinity of the ocean water. The area of concern is the uppermost region where the current velocity is highest. The salinity of water is defined as the number of grams (g) of material in 1000 g of water. Therefore, salinity has no physical units but it is measured in practical salinity units (PSU). If a body of water has 25 g of salt dissolved in 1000 g of water, then its salinity would be 25 psu . In order to plot a density profile of ocean water, an online calculator based on Fofonoff, P. and R. C. Millard Jr (1983) Algorithms is used for computation of the salinity of seawater. (Unesco Technical Papers in Marine Sciences). Figure 4.3 shows the

salinity profile offshore the coast of Ft. Lauderdale, and the highest salinity is found to occur at a depth of about 60 m.

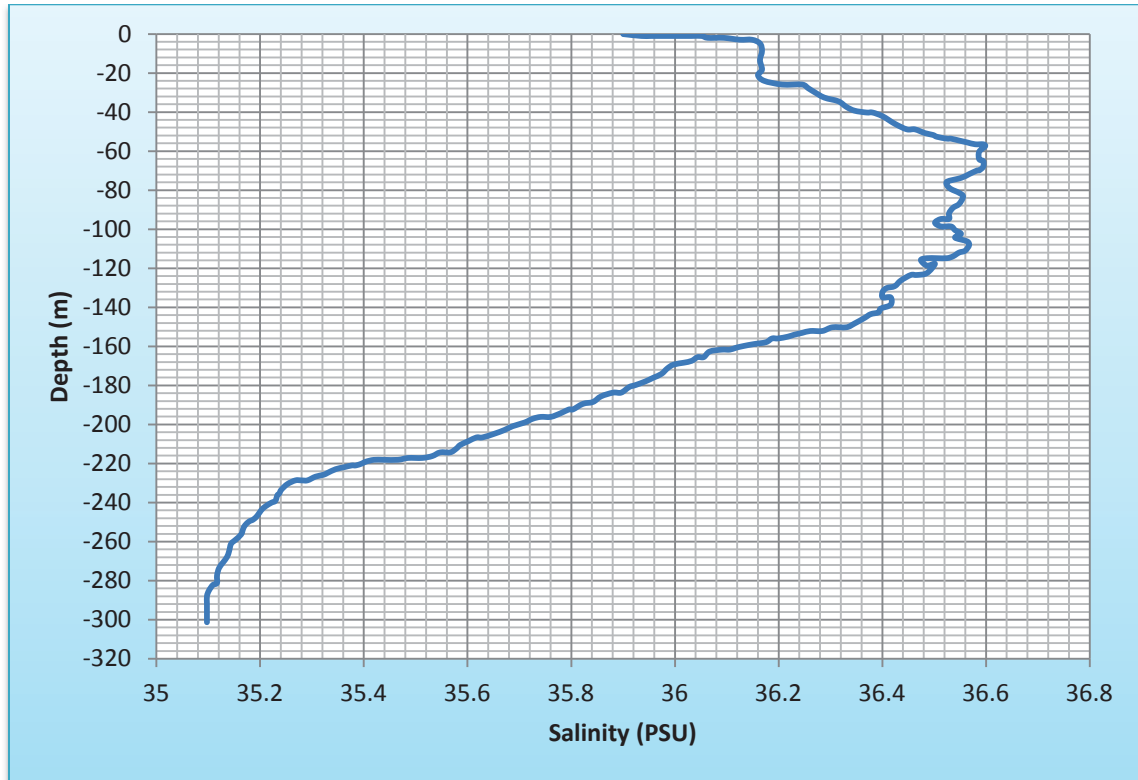


Figure 4.3- Salinity-depth plot from the data collected by the SNMREC using the CTD instrument offshore the coast of Ft. Lauderdale, Florida.

The online calculator is used to calculate the density based on salinity, temperature and ocean depth. Figure 4.4 shows the plotted values for density computed using the online calculator at 10 m ocean depth increments.

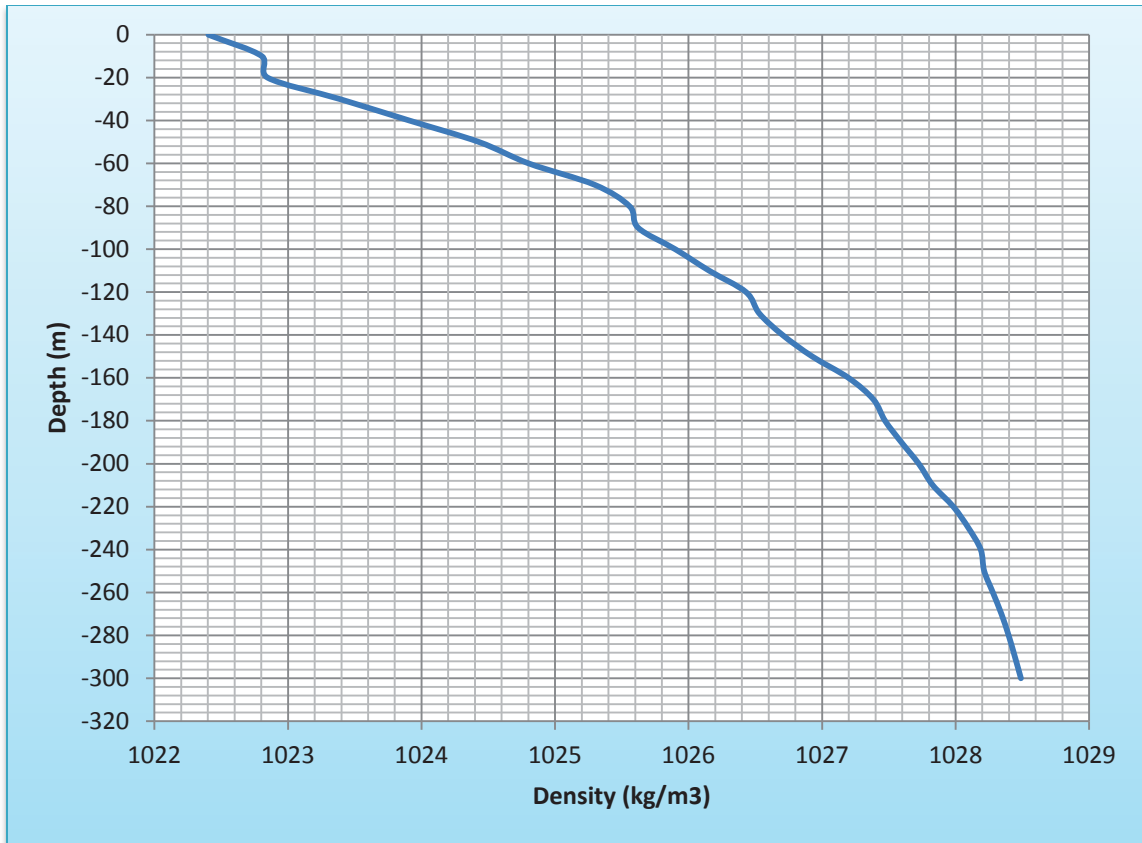


Figure 4.4- Density profile computed using online calculator using salinity, temperature, and ocean depth data.

4.3 Fluid Flow in Marine Current Turbines

The type of fluid flow is a key factor in the numerical simulation. Therefore, the analyses should take into account the accurate fluid flow properties of the ocean near the southeast coast of Florida. Using the data obtained from the SNMREC, an ocean current velocity profile with respect to depth is plotted to show the maximum, minimum and average values of current velocity based on the two years of collected data. Figure 4.5 shows the comparison of these plots, which indicates the highest current velocity measured at 21 m below the surface. The average current velocity is seen to reach its

maximum value of about 1.6 m/s at this depth and decreases linearly toward the ocean bottom.

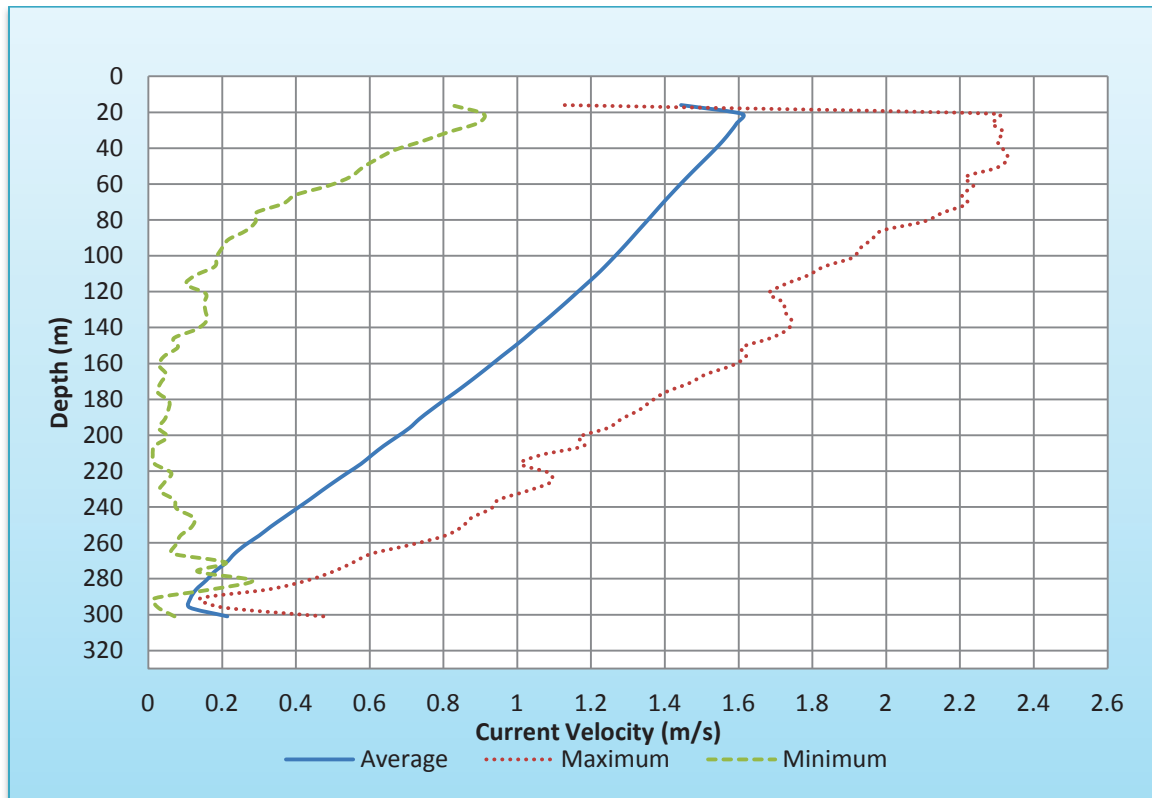


Figure 4.5- Comparison of average, maximum, and minimum current velocity profiles along the depth of the ocean offshore the coast of Ft. Lauderdale, FL.

The magnitude of ocean current velocity is used to determine the mechanical properties for the fluids used in this model. ANSYS FLUENT provides comprehensive modeling capabilities depending on whether the desired fluid flow is compressible or incompressible, laminar or turbulent and steady state or transient.

4.3.1 Compressible or Incompressible flow

Determination is first made whether the flow of water along the computational domain is compressible or incompressible. The Mach number determines whether or not

a fluid is to be considered as compressible or incompressible. Equation (3.2.3) is used to calculate the Mach number of the air and ocean water. The speed of sound propagating in sea water at a temperature of 30°C is $1,507\text{ m/s}$ (Engineering Toolbox, 2011). Using Equation (3.2.3) with the highest current velocity of about 2.3 m/s , the Mach number for ocean water is calculated to be:

$$M = \frac{2.3}{1507} (1.4 \times 10^{-4}) = 2 \times 10^{-7}$$

The highest wind speed observed for a given day is about 10 m/s . (Nat. data. Buoy. Cntr). The speed of sound in air at standard atmospheric pressure at a temperature of 30°C is 349.1 m/s . (Engineering Toolbox, 2011). Applying Eqn. (3.2.3) gives:

$$M = \frac{10}{349.1} (1.4 \times 10^{-4}) = 4 \times 10^{-6}$$

From Equation (3.2.4), the water and air can be considered as incompressible fluids if $\frac{1}{2}M^2 \ll 1(1.4 \times 10^{-5})$.

For water, $\frac{1}{2}M^2 = 2 \times 10^{-14} \ll 1.4 \times 10^{-5}$, and for air $\frac{1}{2}M^2 = 8 \times 10^{-12} \ll 1.4 \times 10^{-5}$, so both fluids can be considered as incompressible.

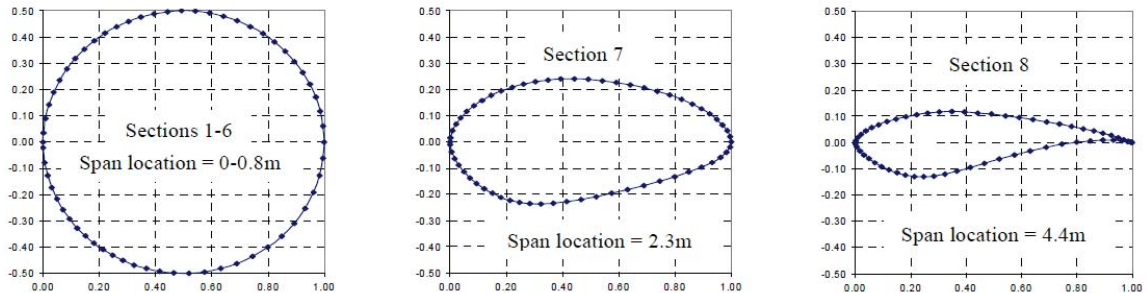
4.3.2 Laminar and Turbulent Flow

Equation (3.5.13) is used to calculate the Reynolds number. The dynamic viscosity, μ of water at 30°C is $0.798 \times 10^{-3}\text{ N}\frac{\text{s}}{\text{m}^2}$. The Reynolds number is then calculated using an ocean water density, ρ of $1,027\frac{\text{kg}}{\text{m}^3}$, an average velocity, v of 2.3 m/s , and a diameter, d of 50 m . Since the computational domain is cubical with sides of

50 m, the representative diameter of 50 m is chosen for the equivalent pipe diameter. Applying Eqn. (3.5.13) yields a value of 147×10^6 for $Re \gg 2000$, hence the flow is turbulent.

4.4 Modeling the Rotor Blade and Hub using SolidWorks

A 43.2 m diameter turbine blade is used in the present study on which the numerical calculations are performed using ANSYS FLUENT. Cross sections of each of the three blades are based on published literature from the National Renewable Energy Laboratory (NREL) in the form of cross-sectional curves. The cross sectional coordinates are adjusted based on chord length based on (Migliore, 2004). Figure 4.6 shows the plots of the cross-sectional curves used in this study.



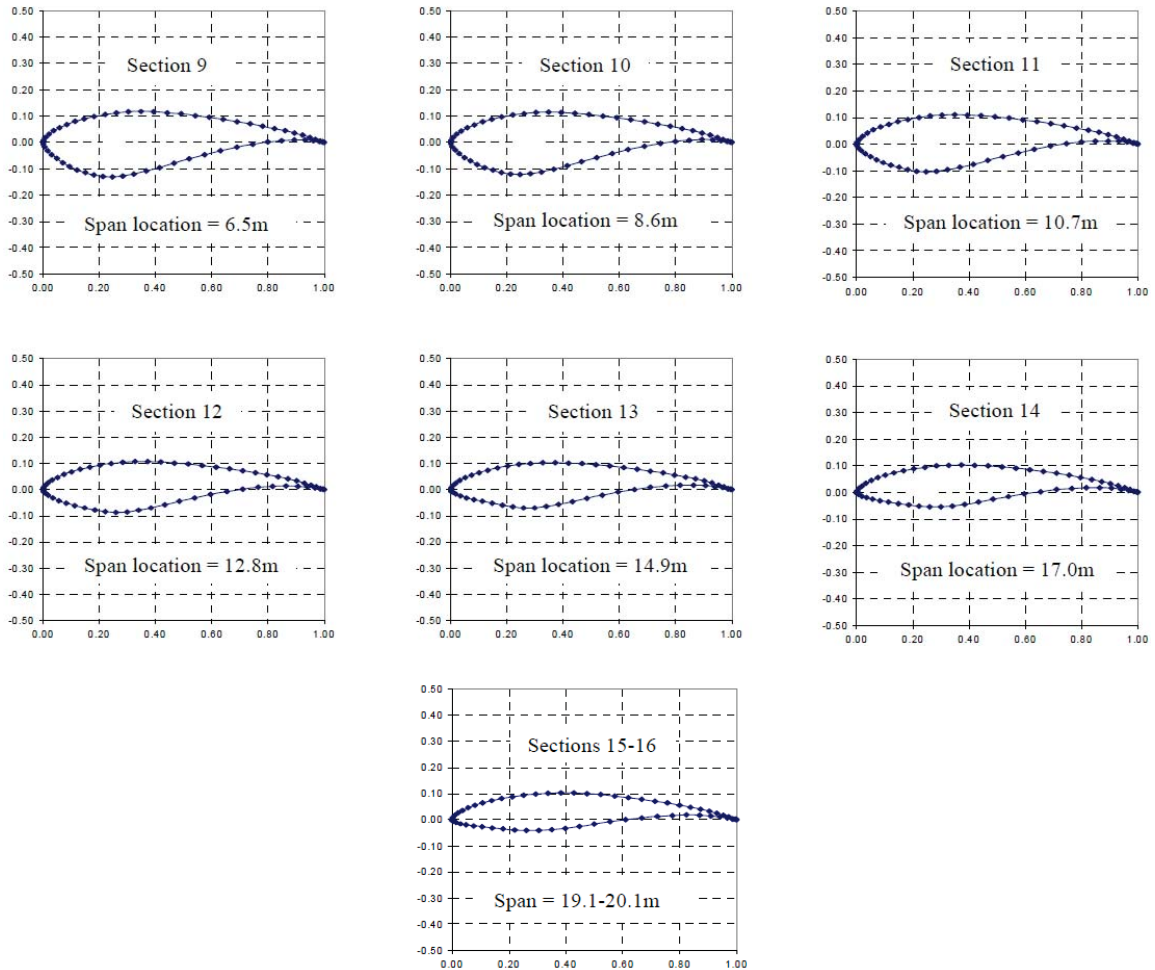


Figure 4.6- Cross-sectional curves obtained from the National Renewable Energy Laboratory (NREL).

A curve digitizer, GetData is used to obtain the xyz coordinates of each cross section which are given as input into *SolidWorks* in text format. *SolidWorks* is a 3D mechanical computer aided design (CAD) program developed by Dassault Systèmes *SolidWorks* Corp. It is used to create a solid geometry of the blade by connecting the curves to form a surface. The “Loft” feature is used to connect the curves from hub to tip. A final rendering of the full completed loft blade is shown in Figure 4.7 below:



Figure 4.7- Completed blade formed from building lofted base from imported cross-sectional curves.

The optimum operating pitch angle to maximize the lift/drag interaction is between 12-15°[Somers, 1992; Somers, 1997]. In the present study, a pitch angle $\beta = 15^\circ$ is used due to time constraints. Each blade is created using the loft feature, then given the respective pitch angle. Figure 4.8 shows the pitch angle given to each of the blades.



Figure 4.8 - Pitch angle of blade on model set at 15°.

The blades are rotated 120° from each other. Once the blades are in place, the root of each blade is connected to a 3m diameter hub at the center. Figure 4.9 shows the *SolidWorks* model of the three blades of the turbine rotor. A filleted hub tip is created for hydrodynamic purposes.



Figure 4.9- Completed rotor blade showing tri-blade setup connected to a center hub with face fillets.

The blade is exported as a “Parasolid” file format so that it can be imported into the meshing software ANSYS ICEM CFD.

4.5 Creation of Domain and all its Entities using ANSYS ICEM CFD

4.5.1 Blade Geometry Manipulation

The “Parasolid” blade created using *SolidWorks* is imported into ANSYS ICEM CFD where it is checked for continuity using the “geometry repair” tool. The geometry repair tool extracts the curves used to create the blade geometry along the surfaces of the rotor. The connected points used to create the curves are also extracted. After the “Build Diagnostic Topology” option is used, new curves are formed along the boundaries of the surfaces. The topology is repaired based on a “tolerance” of 0.07 with the “Filter points” and “Filter curves”. The entire blade is treated as a single part in ANSYS ICEM CFD. In

order to achieve results specific to a single blade, multiple parts are created from the single part. Each blade is assigned a part name: blade 1, blade 2, and blade 3. All surfaces which cover each blade until the blade connects with the hub are selected when creating the blade part. In this way, the CFD program can distinguish results for bending moment and pressures on individual blades, making it easier to analyze the structural integrity of the connections. Figure 4.10 shows the rotor blade with separate parts assigned to each blade for ease of data representation.

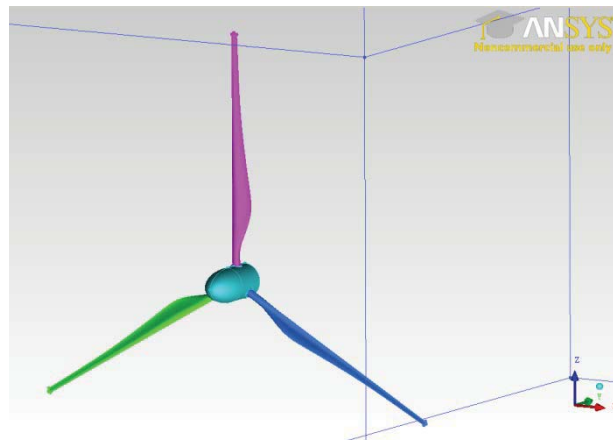


Figure 4.10- Repaired blade showing the location of curves only along the edges of the surfaces in the geometry

4.5.2 Computational Fluid Domain

In order to create the computational fluid domain, the “Simple surface” feature is used. This opens the “Create/Modify Surface” window. From here the “Standard shapes” menu is chosen to allow the creation of a “Box” under the submenu of “Create std geometry.” Within this submenu, the geometry can be created either by specifying the origin and the extents of the domain or by just specifying the “Entity bounds.” For this computational domain, the origin and extents specification method are used. The origin is

set at $XYZ (-25, -20, -25) m$. The turbine rotor blade was created such that the axis of rotation is positioned along the y -axis in the global coordinate system shown in Figure 4.11.

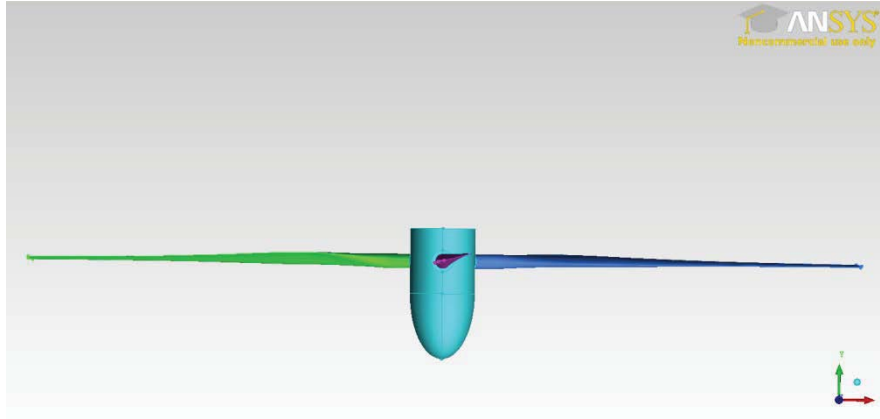


Figure 4.11- Repaired rotor blade in ICEM CFD showing the global y -axis (the axis of rotation of the turbine).

4.5.3 Multiphase Domain

Extents of Domain

The computational domain for the multiphase model extends $50 m$ in the $x - axis$ direction, $120 m$ in the $y - axis$ direction and $65 m$ in the $z - axis$ direction. This domain is divided into two separate domains along the $xy - plane$ at $z = 0$. The domain can, therefore, be considered as the single phase domain with an added second domain directly above the top surface. Figure 4.12 shows the dimensions of the computational domain used for the multiphase model. Similar to the single phase model, the domain for this model extends roughly 2.5 diameters behind the turbine in order to refine the elements around the blade geometry as much as possible (Reza, 2010).

The present study uses a rotational speed of 7 rpm and maximum current velocity of 2.50 m/s . Due to time and computational power limitations, 2 million mesh elements are used for the model. As a result of this limitation, the domain for this model extends roughly 2.5 rotor diameters past the turbine in order to refine the elements around the blade geometry.

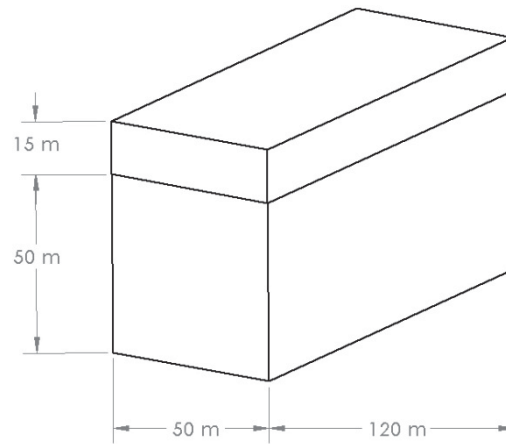


Figure 4.12- Sketch showing the dimensions of the multiphase computational domain used in the model

The geometry of the full computational domain is shown in Figure 4.13 below:

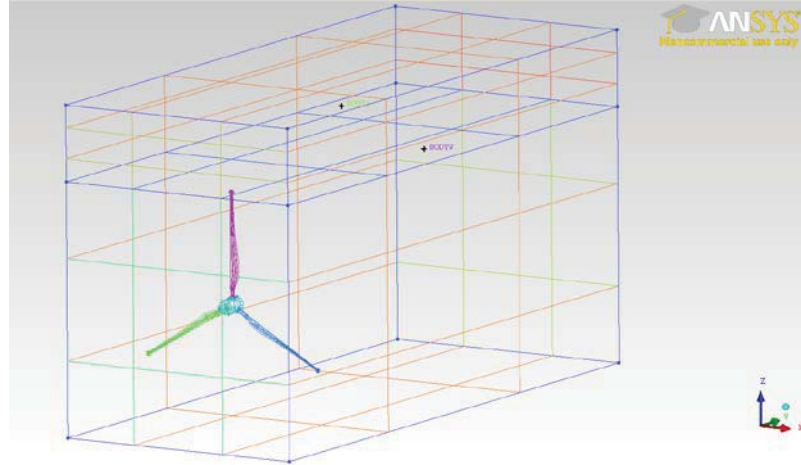


Figure 4.13- Geometry layout of the full computational domain showing position of blade along the **y – axis**.

Part Geometry Setup

The boundaries of the full domain are converted to “Parts” by selecting individual faces of the domain. For this domain, there are separate faces in front of the turbine blade. The lower face is designated as “INLET.W” to represent the water inlet, whilst the upper face is given as “INLET.A” to represent the inlet for air. The faces behind the turbine are labeled as “OUTLET.A” and “OUTLET.W” to distinguish between the outlets for air and water respectively. The remaining faces are named “SYMMETRY.” The face between the two fluid domains is not given a name. The boundary conditions at these faces will be explained later in this section. Figure 4.14 - Figure 4.18 show the parts of the multiphase domain.

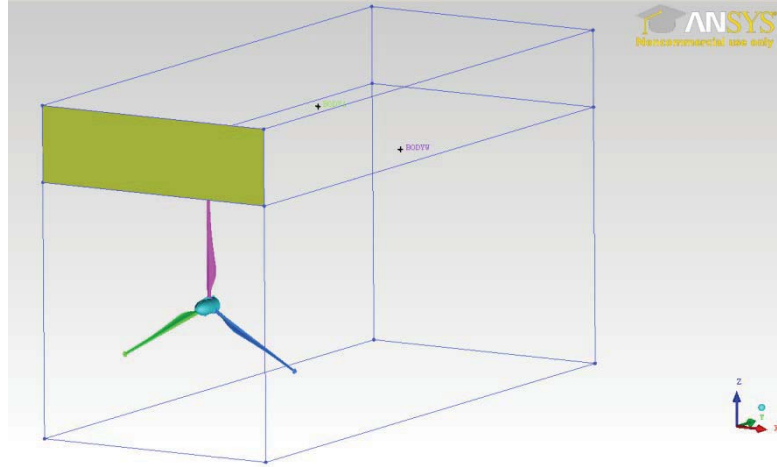


Figure 4.14- Multiphase computational domain for “INLET.A” part setup

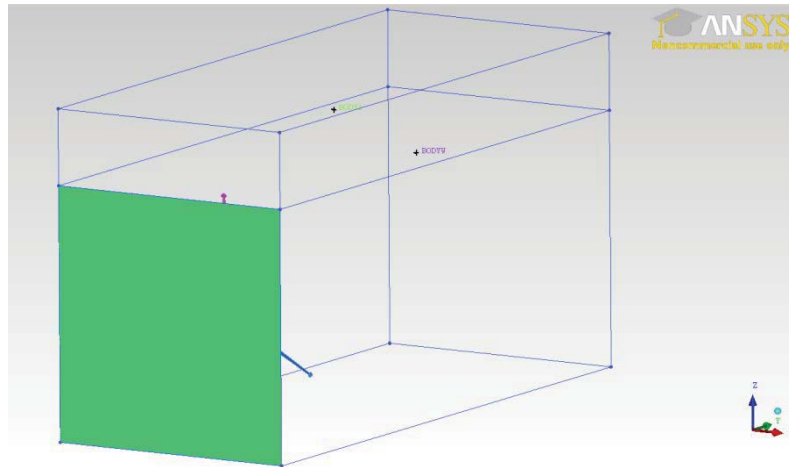


Figure 4.15- Multiphase computational domain for “INLET.W” part setup

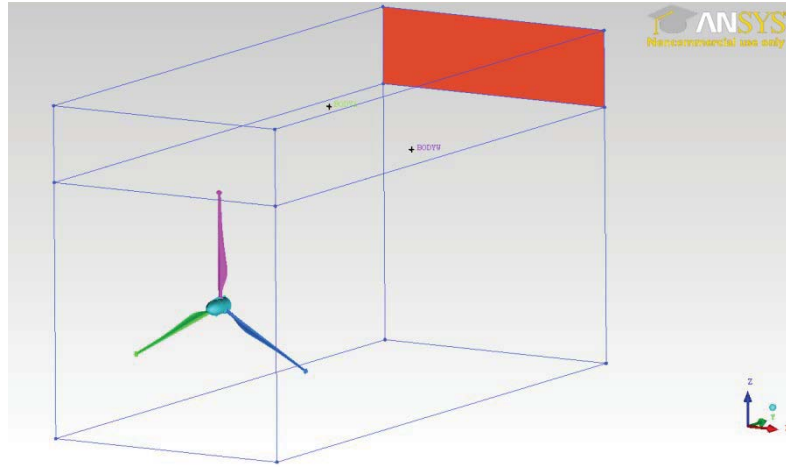


Figure 4.16- Multiphase computational domain for “OUTLET.A” part setup

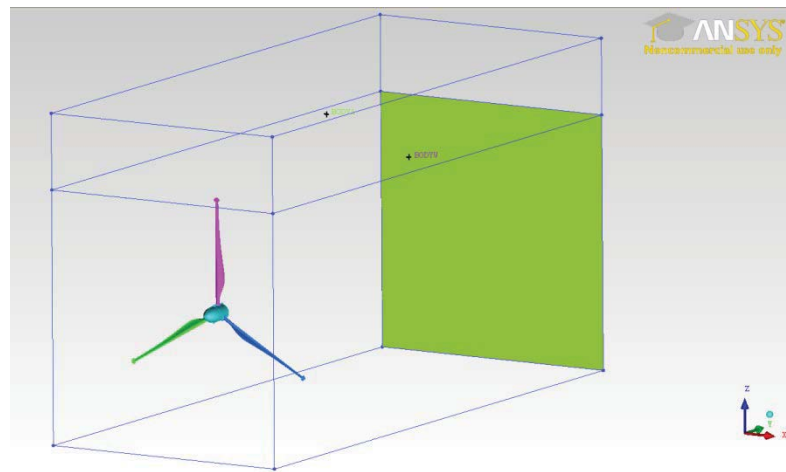


Figure 4.17- Multiphase computational domain for “OUTLET.W” part setup

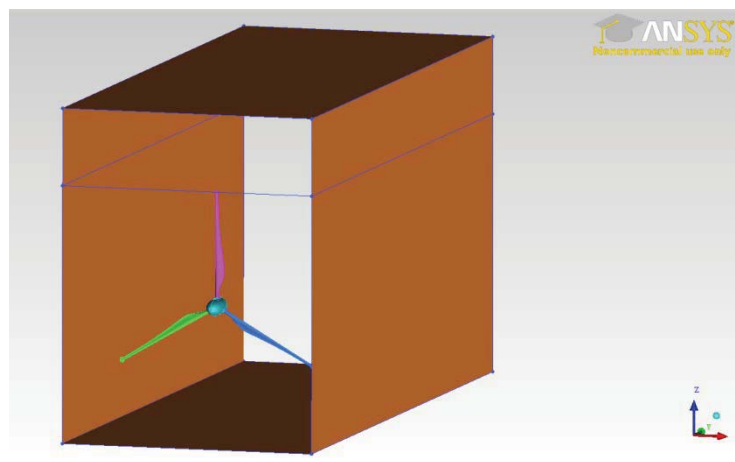


Figure 4.18- Multiphase computational domain “SYMMETRY” part setup

Creating Fluid Bodies

The body for the multiphase fluid model includes separate bodies for the air and water phase. The “Create Body” icon is used to specify the first point along the geometry of the blade and the second along one of the edges of the “INLET.W” face to create the first body, “BODY.W.” This body will contain the ocean water portion of the two-phase model. For the second body, the two points are chosen from the lower edge of the “INLET.A” face to the upper edge of the “OUTLET.A” face. This body called “BODY.A” will contain the air phase of the two-phase model. The two separate bodies, “BODY.A” and “BODY.W” are shown in Figure 4.19 below.

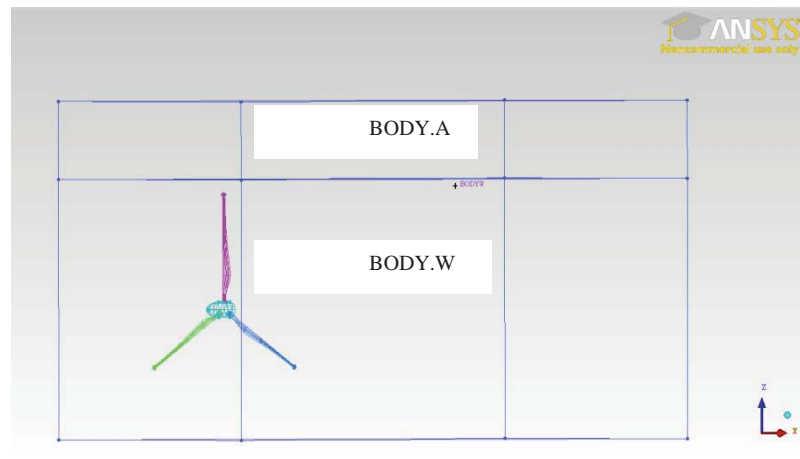


Figure 4.19- Separate bodies created for the two phase computational domain: "BODY.A" (top) for the air phase and "BODY.W" (bottom) for the water phase.

4.6 Meshing the Domain and Blade

4.6.1 Mesh Type Selection

Generation of an adequate yet simplistic mesh is extremely important to the CFD model. The mesh must be able to cover the areas where detailed analysis is required the most while expanding in size at areas where the change in measured quantities is locally minimal. At the same time, limitations on the CFD modeling software prevent too large number of mesh elements; hence the mesh size is restrained. In ANSYS ICEM CFD, three categories of mesh are used.

- Structured Mesh – For 3D domain, the structured method uses hexahedral mesh laid out in a regular repeating pattern. This method allows twisting of the elements allowing the user to have more control over shapes of elements. As a result, the mesh conforms more easily to any geometry shape and size. This type of mesh, however, requires more expertise to use and tends to be more time consuming (Reza, 2010).
- Unstructured Mesh – this method uses arbitrary elements throughout the domain using tetrahedral elements for 3D applications. This type of meshing requires less user manipulation, therefore, it is the preferred method in this study.
- Hybrid Mesh – this method uses a form of structured mesh containing hexahedral, tetrahedral, prismatic, and pyramid elements in the 3D domain. Basically, hybrid mesh combines unstructured and structured mesh types to form a controllable mesh domain, but these meshes still require expert knowledge to create.

Volume meshing is preferred over surface or prism meshing. The surface mesh does not allow analysis within the computational domain, and the prism method encounters difficulty in clustering in the lateral direction due to the underlying triangular structure (Reza, 2010). The options of elements within volume meshing are: hexahedral elements and tetrahedral elements. Due to simplicity, tetrahedral meshing is used for both phases in this model.

4.6.2 Multiphase Mesh Setup

Tetrahedral mesh elements are used for the multiphase model due to its simplicity and speed of computation.

Global Mesh Setup

For the global mesh setup of the multiphase model, a “Scale Factor” of 1 is used so that no user implied scaling of the mesh is imposed. The display can be toggled on and off to visualize a tetrahedral element of the specified Scale Factor in three dimensional space. The “Max Element” size is set to 2. The “Curvature/Proximity Based Refinement” option is set to a minimum size of 0.1. Therefore, the smallest size an element can adopt is 0.1 *m*. Within the “Curvature/Proximity Based Refinement” window, the number of “Elements in gap” is set to 2 so that there are more elements within close proximity of surfaces, and the “Refinement” is set to 12 so that there are a maximum of 12 elements within 360°.

Part Mesh Setup

The maximum size for individual entities of the multiphase domain are assigned within the “Part mesh setup” dialog box. For the first multiphase model, the mesh size for the “INLET.A,” “INLET.W,” “OUTLET.A,” “OUTLET.W,” and “SYMMETRY,” boundaries are set to the maximum element size of 2, whilst the rotor blade was given a maximum mesh size of 1.

Volume Meshing Parameters

After setting the global mesh constraints for the model, the volume meshing type is set to “Tetra/Mixed” indicating that Tetrahedral elements will be used. The default setting for the remainder of options are used for the first mesh computation. After computing the mesh, the cross section of the volume meshing elements near the blade is observed to rapidly increase in size from the areas of curvature and proximity. Figure 4.20 shows the initial cross section of the meshed computational domain and blade with increasing sized elements from the blade to the boundaries.

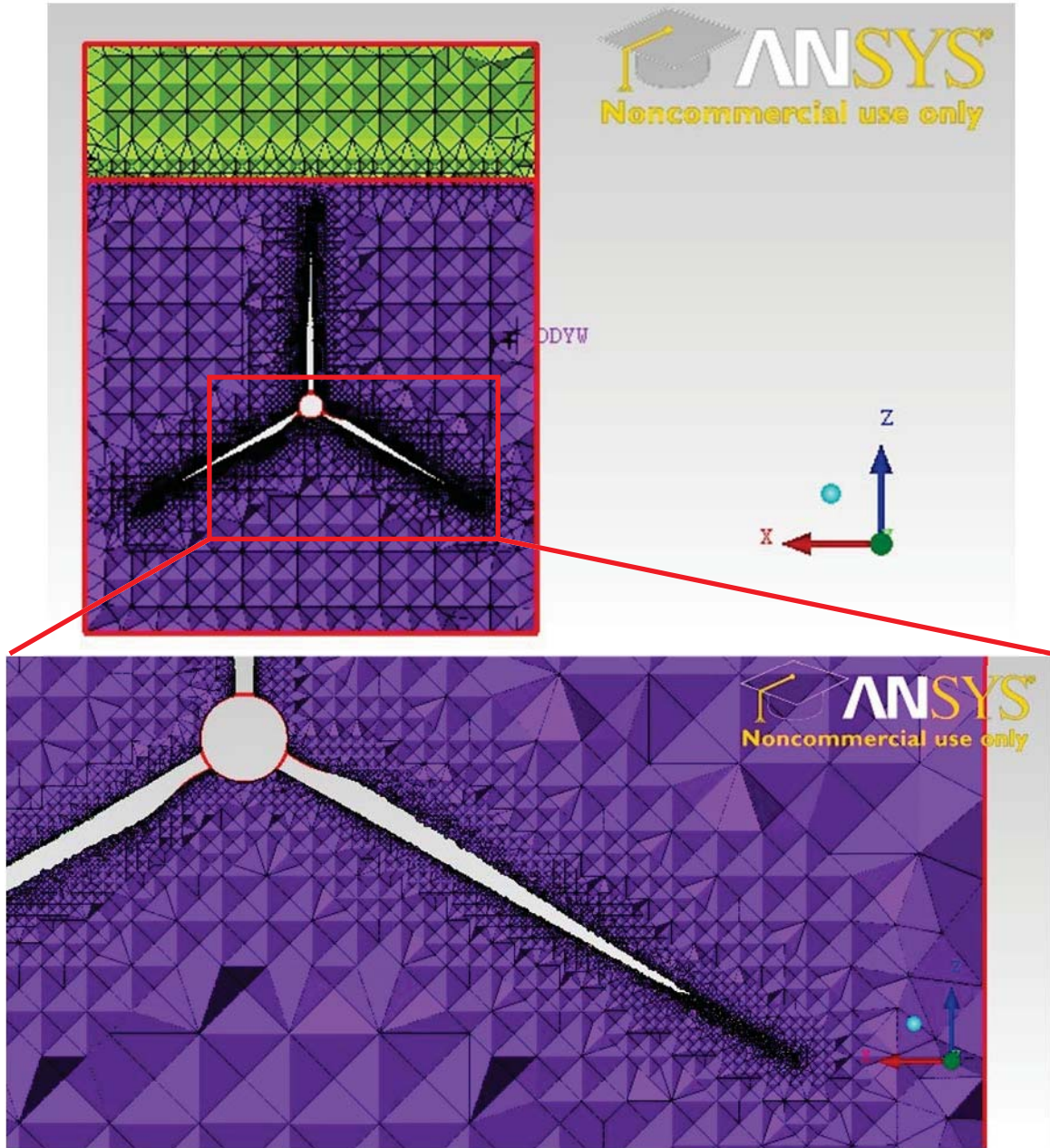


Figure 4.20- Initial mesh quality used for simulation of the multiphase domain model.

Refining the Mesh

This type of rapid mesh expansion is not desired in this model as the solution would not be as accurate. The transitions in size are smoothed out using a “Quick (Delaunay)” mesh method instead of the default setting of “Robust (Octree).” The “Delete volume elements” option from the “Edit Mesh” tab is used to get rid of all volumes within the Octree mesh. The “Smooth globally” option is then used to smooth the surface mesh transitions based on the Laplace smoothing technique. Once completed, the Delaunay method is used to compute the mesh with prism layers turned on. The improved mesh quality is shown in Figure 4.21 below.

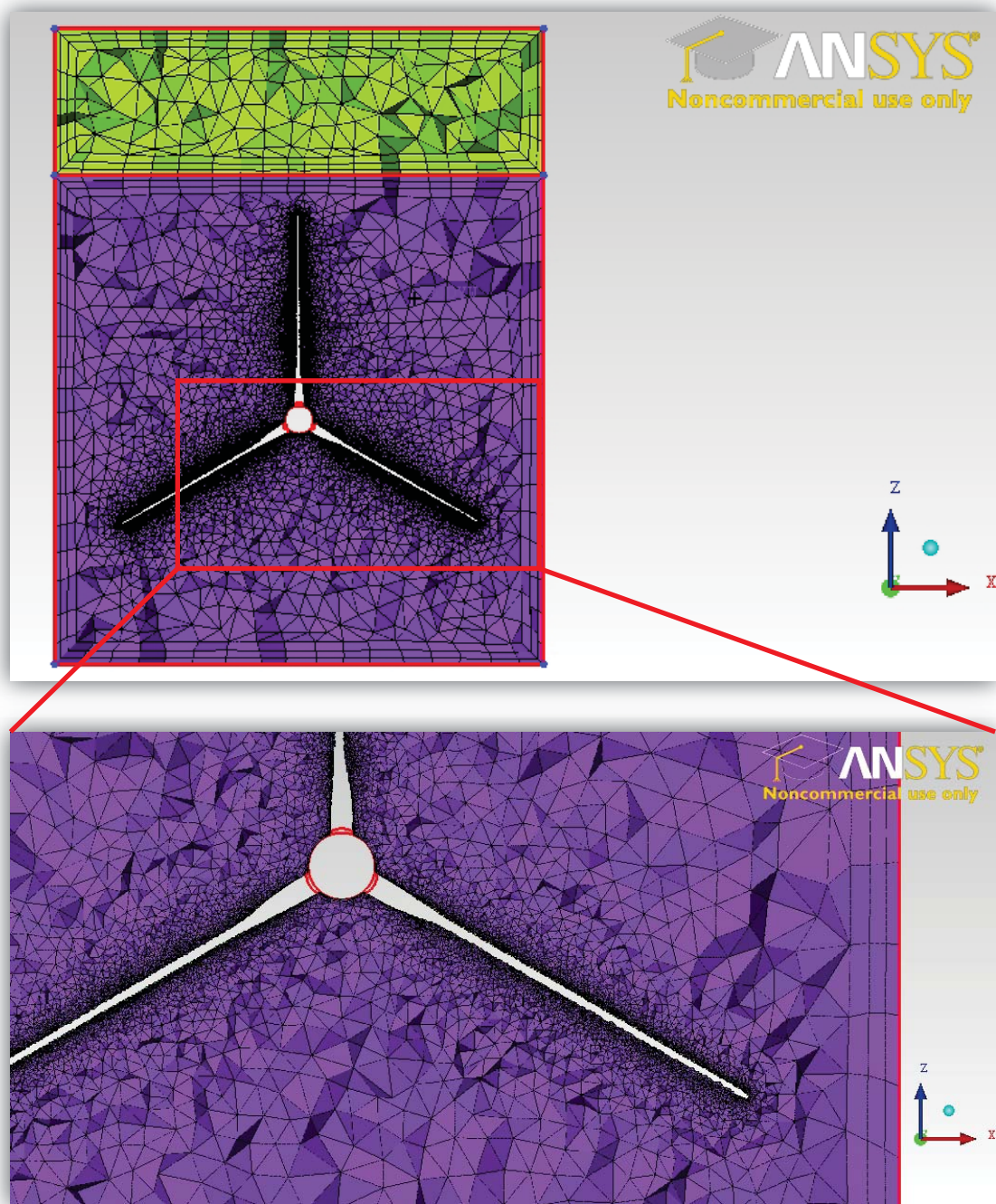


Figure 4.21 - Delaunay mesh detail for multiphase setup.

Output Setup

The solver of choice is the Fluent V6 since ANSYS FLUENT is used in the computation of the fluid model. After setting the desired solver, the boundary conditions for each face and part of this model are set. The boundary conditions determine which face will be used as an inlet for the water flow and where the flow will exit. The “INLET.A” and “INLET.W” faces are given boundary conditions of “velocity inlet” for the multiphase model. The “OUTLET.A” and “OUTLET.W” faces are given “outflow” boundary conditions so that the volume of fluid (VOF) model can be used. The side walls, top and bottom of the computational domain are given as “symmetry” boundary conditions. The interior “BODY.A” and “BODY.W” are given “fluid” boundary conditions to represent the flowing water and air phases that are present in this study. The fluid types and specifications are selected in ANSYS FLUENT. The rotor blades and hub are given boundary conditions of “wall” so that the CFD program will treat them as solid objects within the fluid domain. After the boundary conditions are set up, the tetrahedral mesh is saved for modeling in ANSYS FLUENT.

4.7 CFD Simulation using ANSYS FLUENT

4.7.1 Multiphase Flow CFD

In order to set up the multiphase flow model, certain parameters are first calculated. These parameters include the wavelength (λ), the angular velocity (ω) and frequency (f) of the waves being modeled. In order to calculate the wavelength, the wave period must be known. From Figure 2.7 the range of wave periods used in this study are chosen to be between 9 and 15s. These values were visually picked off of the color coded charts in Figure 2.7, which represents the minimum and maximum wave periods recorded over at least 114 hour period for a particular day. Based on the current velocity and wave height, the wavelengths are calculated to range between 126.5 and 351.3 m. These values are given as input in ANSYS FLUENT when using the Open Channel Wave BC model. The peak wave height recorded based on Figure 2.6 is 2 ft or 0.609 m. This value represents the vertical distance between the crest to the trough of a particular wave. The wave amplitude is the magnitude of the displacement of the wave from still water position.

Once the parameters are obtained, the multiphase mesh is read into ANSYS FLUENT. The mesh is translated so that the axis of rotation of the turbine blade passes through the point $XYZ (0,0, -25)$ and the normal to the plane of rotation is parallel to the $y - axis$. The mesh is then checked for errors using the mesh check feature on the general problem setup menu. A pressure based solver is used for this model along with absolute velocity formulation. The multiphase model uses transient flow time to simulate

the movement and effects of waves. Gravity is then turned on and set to $-9.81 \frac{m}{s^2}$. The Open Channel Flow with Wave Boundary Conditions model is chosen to replicate the real scenario of waves plus current. Under the “materials” tab, air and water are added, changing the water density from $1000 \frac{kg}{m^3}$ to $1023 \frac{kg}{m^3}$ to account for greater unit weight due to salinity in seawater. Air is selected as the primary phase while seawater, as the secondary phase. The secondary phase is typically the flowing fluid below the primary phase. The surface tension of water in contact with air and normal temperature ranges offshore Ft. Lauderdale is about $0.07 N/m$. This value is used for phase interaction. Boundary conditions are set up individually for each inlet and outlet. For the Open Channel Wave BC model, the same wave length and amplitude must be set up in each inlet. Both the water and air domains are given a constant current velocity of $1.7 m/s$. This value is chosen based on the average surface velocity measured by the ADCP offshore the coast of Ft. Lauderdale. The direction of flow for both inlets is chosen to be in the negative $y - axis$ direction, which represents the length along the computational domain.

Flow with Waves

The wave amplitude is set to a value based on meteocean data obtained from at the Miami weather center offshore the Southeast coast of Florida. The simulations using ANSYS FLUENT are made varying the wave amplitude and current velocity to replicate actual conditions and then the torque, thrust, and power are compared for still water flow and flow with waves.

Results from previous work done by (Singh & Arockiasamy, 2011) on single phase flow effects on marine current turbines show the use of the Standard $k-\varepsilon$ turbulence model to obtain the pressure and velocity plots along the length of the turbine axis of rotation. These plots are compared to the actuator disk to determine the suitability of ANSYS FLUENT CFD to model the current velocity. The present study uses this preliminary research to develop the multiphase model to simulate waves and current velocity on the turbine.

CHAPTER 5

PARAMETRIC STUDIES AND DISCUSSIONS

5.1 Introduction

This chapter presents the results of models with varying mesh element densities with an objective of establishing the grid independent model based on convergence of upstream and downstream pressures around the turbine rotor blade. The results from multiphase flow models simulating still water and two different wave heights are presented along with discussions. The wave heights considered are based on meteocean data obtained from the meteorological center in Miami, FL. All three models are run in ANSYS FLUENT using the *Standard k- ω* turbulence model for a current velocity in the range of 1 m/s to 2.5 m/s . The still water model is run without any wave input while wave heights of 1ft (0.305 m) and 2ft (0.609 m) are used for the other two models. The effect of waves on the thrust, torque, power, bending moments, lift, and drag are compared to those with the still water model.

The present study compares the upstream and downstream pressures around the turbine rotor blade, as well as calculated thrust force, power and thrust coefficients. The results from the grid independence study are discussed to establish the adequacy of the mesh resolution for modeling. For this model, the trailing edge is meshed to a reasonable

degree of accuracy within the constraints of the available computational power. As a result of this restriction, the element sizes are adjusted to cover the blade all the way to the trailing edge. The *Standard k- ω* turbulence model used in the present study is based on the relevance of the model to wind and marine current turbine applications.

5.2 Mesh Verification and Grid Independence

In order to establish the adequacy of the number and sizes of elements that will ensure accuracy of the results, a number of simulations were carried out using several mesh densities. The models were created and meshed by decreasing the global mesh scale factor by *0.1* each time until two successive models yielded the same results for pressure, torque and thrust.



Figure 5.1- Grid Independence Study Performed so as to obtain convergence of Thrust and Pressure on the Turbine.

Figure 5.1 shows convergence in the solutions when the number of mesh elements increase to about 650,000. Refinement of the model is continued until the mesh size can conform to the thinnest blade sections without discontinuity. A satisfactory mesh containing 2,000,000 elements was finally resolved and used for computation. The computational domain size was verified after running a simulation and comparing simulated current velocity and pressure. These values for each model were monitored using color coded contour plots of the cross section of the domain along the length of the turbine flow direction. It was noticed that towards the walls of the domain denoted as symmetry boundary conditions, there was no change in velocity or pressure from the initial values so it was safe to assume that the computational domain was adequate. As current velocity and blade rotation increase, additional modeling would be necessary to establish the domain size. A general norm is to use a domain which extends at least 1 diameter on either side of the turbine swept area. For efficient computational usage, the domain had to be optimized based on results as much as possible.

5.3 Turbulence Study

Six different turbulence models are evaluated in this study for comparison and identification of the most appropriate model for Marine Current Turbine (MCT) simulations. The turbulence models include: Standard $k-\varepsilon$, Re-Normalization Group (RNG) $k-\varepsilon$, Realizable $k-\varepsilon$, Standard $k-\omega$, Shear Stress Transport (SST) $k-\omega$, and Transition SST. Based on the evaluation, the turbulence model chosen for the present study is the Standard $k-\omega$ model. This model is chosen because of the stability of the pressure and velocity plots upstream and downstream the turbine rotor plane. Figure 5.2 shows the velocity distribution along the direction of the turbine axis of rotation. An inlet

current velocity of 2 m/s is set at position of -20 m . As the current approaches the turbine, the velocity decreases. The current velocity then increases to a specific value past the plane of rotation decreasing to a steady state value at a distance of 100 m downstream. This distribution follows that given by the classical Actuator Disk Theory (Figure 2.15). The other turbulence models studied did not yield realistic results for the upstream and downstream current velocities.

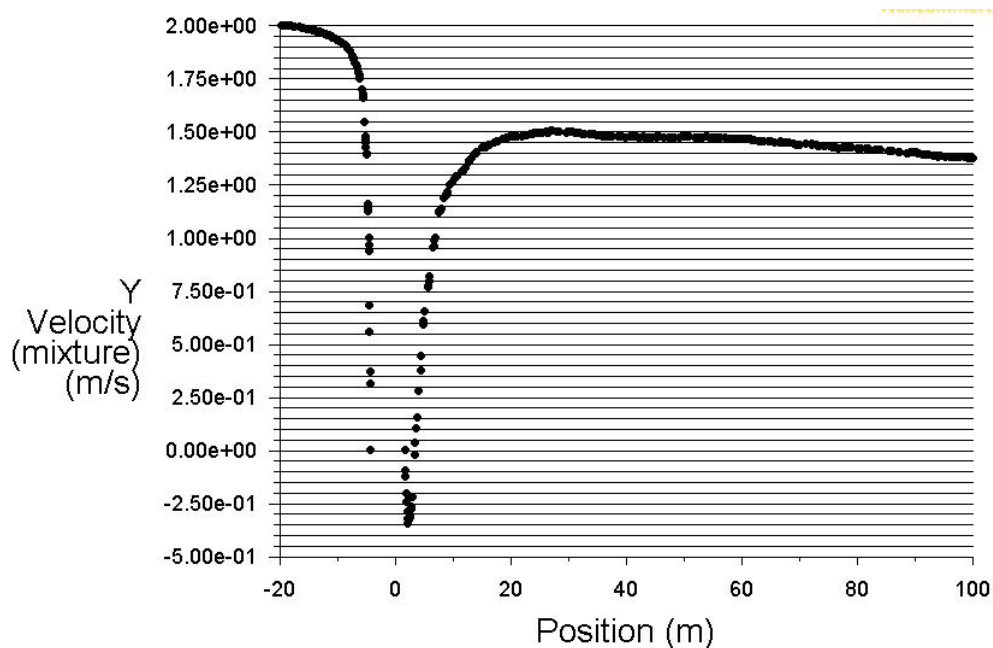


Figure 5.2- Velocity Distribution along the Length of the Direction of Flow. The Turbine Plane of Rotation is Located at Position = 0.

5.4 Turbine Performance

The objective of modeling the still water flow is to create a benchmark for comparison of results from the wave models. This comparison gives the reader a better understanding by how much the turbine performance changes when waves are present. The still water models use a transient time stepping model, and the simulation is allowed

to run for approximately three hours for each model. The time step size is adjusted according to the current velocity so that the simulated results can be obtained at relatively consistent distances along the domain. Upon convergence, the pressures along the length of the channel are obtained along with velocity, torque, bending moments, lift and drag. These results reflect simulated values approaching the turbine rotor blade and past the plane of rotation illustrating the effects of varying current velocities on the simulated quantities. The simulated current velocity is used calculate the axial induction factor and the generated power and thrust on the rotor. The in-plane and out-of-plane bending moments are obtained from force data generated by FLUENT, and compared with the values from the wave models. Figure 5.3 shows the published data on turbine performance based on rotor diameter. The simulated results in the present study are based on a rotor diameter of 43.2 m . for a current velocity of 2.3 m/s , application of the principles of similitude yields a generated power of 4.1 MW , thrust of 9.1 MN , and a torque of 7.5 MNm .

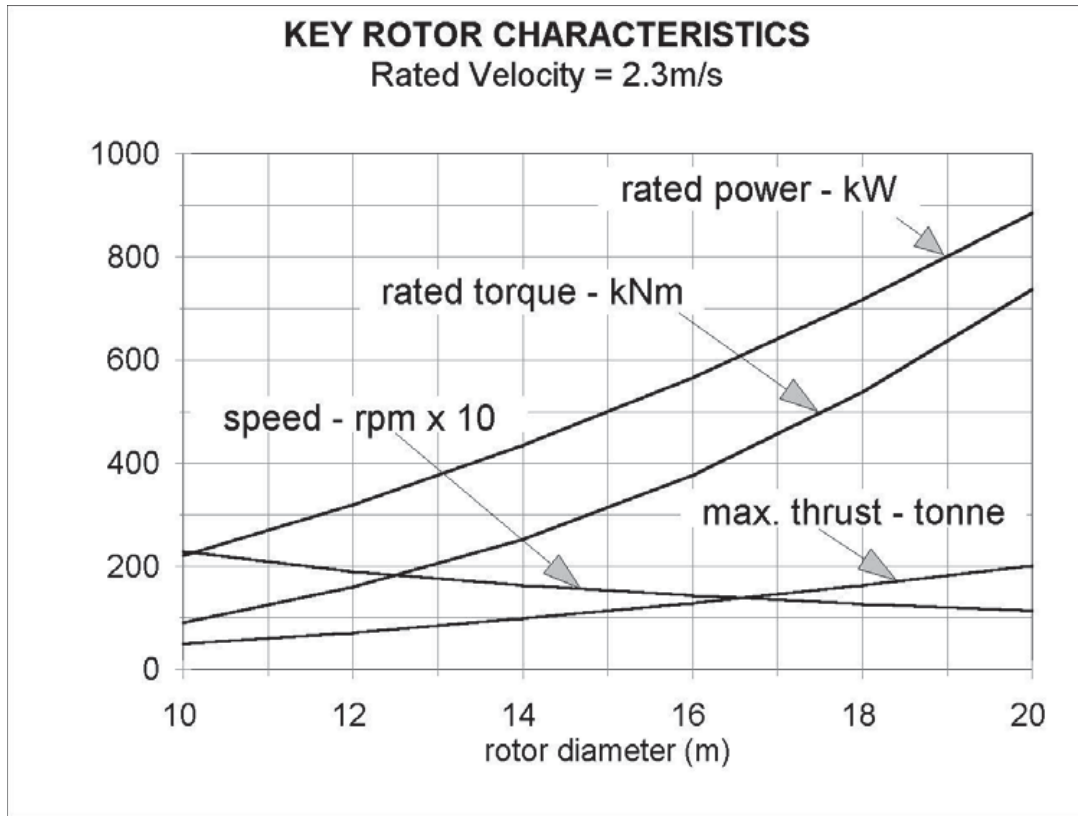


Figure 5.3 - Marine Current Turbine Performance based on Rotor Diameter. (Fraenkel P. P., 2004).

5.4.1 Thrust Analysis

The thrust is the lateral force exerted by the fluid on the turbine rotor blades in the direction perpendicular to the plane of rotation. The simulated thrust is calculated using equation Eqn. (2.5.4) (Harrison, et al., 2009). The axial induction factor, a , is calculated based on the upstream and downstream current velocity. The current velocity downstream is taken from the velocity distribution along the length of the domain at the point past the turbine where the pressure stabilizes. The ideal thrust is calculated using

Equation (2.5.5) using the inflow velocity, V_0 . Figure 5.4 shows the comparison between the ideal thrust (Harrison, et al., 2009) and the simulated values.

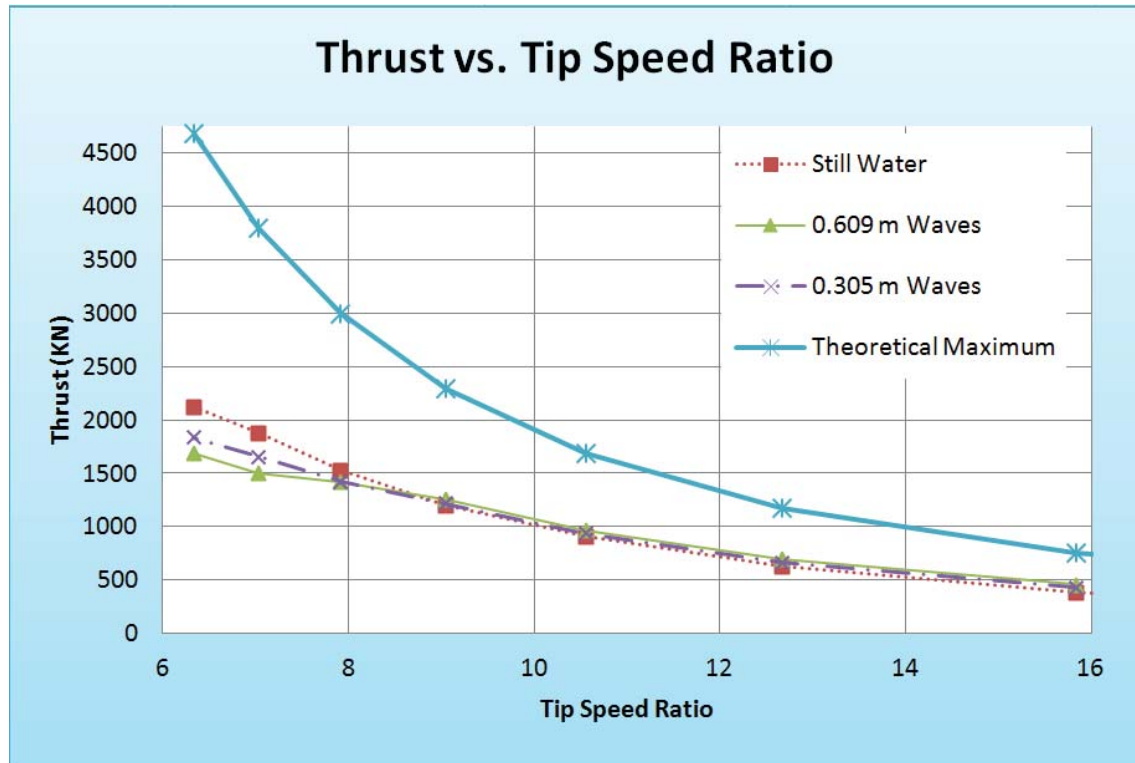


Figure 5.4- Comparison of Simulated Thrust vs. Tip Speed Ratio.

The theoretical values for thrust based on Equation (2.5.5) decreases exponentially as tip speed ratio increases. The thrust in the still water case is about half of the theoretical maximum value. At lower tip speed ratios, it can be seen that the turbine, when subjected to wave conditions, experience lower thrust than the still water case. A 20 percent reduction in thrust is observed when the turbine is subjected to marine current and 0.609 m waves at TSR of 6.33. The thrust values for the still water case and wave models are roughly the same at TSR of 8.5. As the TSR increases, the thrust on the turbine rotor for the still water case is less than that for the wave cases. A wave height of

0.609 m causes a 20 percent increase in thrust at TSR of 15.83. For all the three models, the thrust variations seem to follow the theoretical maximum values.

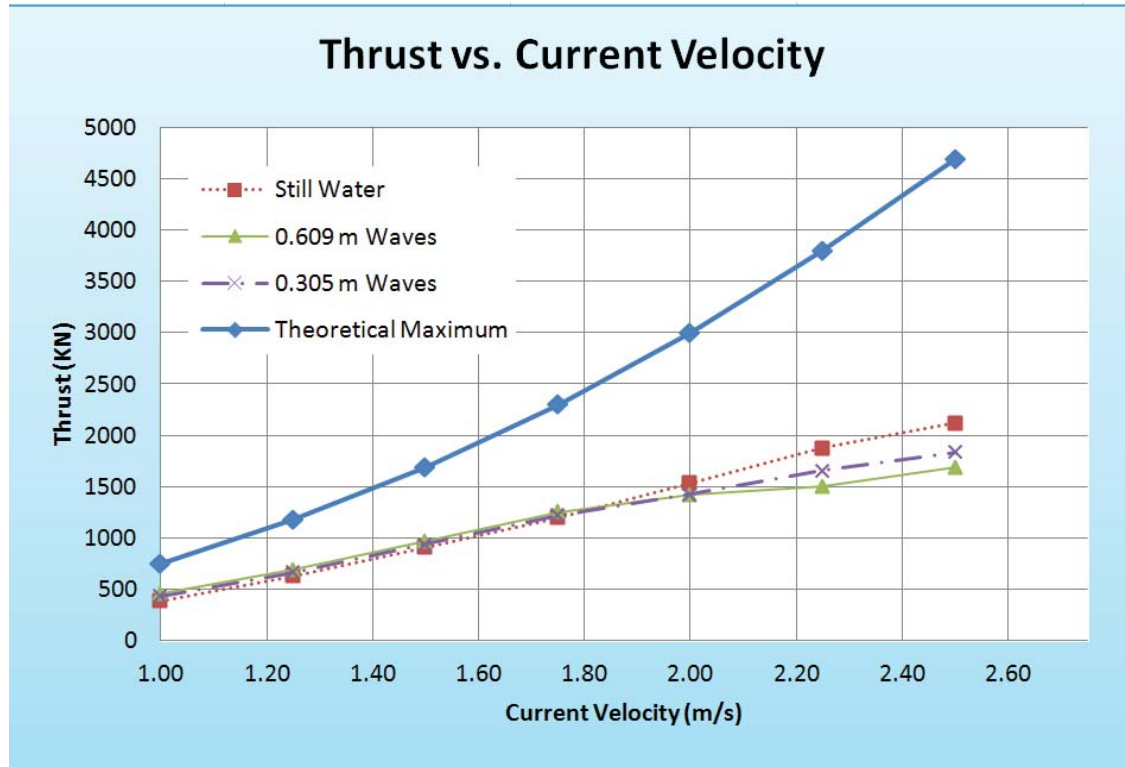


Figure 5.5 - Comparison of Simulated Thrust with Current Velocity.

The theoretical thrust in Figure 5.5 is based on inflow current velocity, V_0 and the rotor swept area, A (Equation 2.5.5). The results from the still water case show a generated thrust of about 50 percent of the theoretical maximum value. As the current velocity increases past 1.80 m/s the thrust in the still water case appears to be linear instead of following the trend of the theoretical curve. At current velocities lower than 1.80 m/s the turbine subjected to waves seems to be experiencing higher thrust than that in still water. At higher current velocities, the thrust values in the wave models are smaller than that in the still water case. At a current velocity of 1.80 m/s the thrust on the

turbine seems to be unaffected by the waves. Figure 5.6 shows the published data on thrust vs. current velocity in still water for a turbine diameter of 0.40 m tested in a tow tank (Barltrop, et al., 2007). Applying the principle of similitude from Equation 3.8.1 yields a similar result. For example, at a current velocity of 1.00 m/s the simulated thrust is 349.9 kN . This compares reasonably with the thrust for the still water case in the present study. For higher current velocities, the thrust values appear to be increasing at a faster rate.

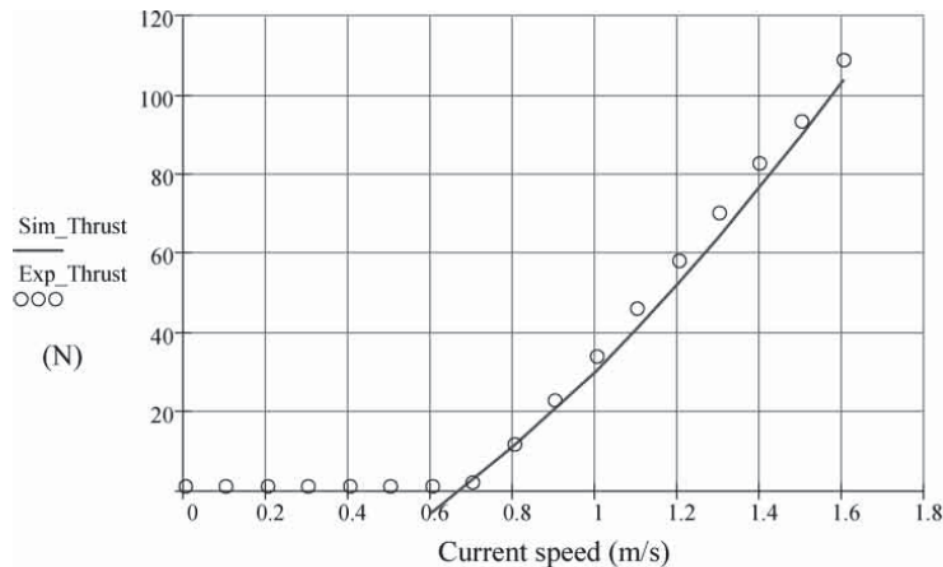


Figure 5.6 - Thrust vs. Current Velocity in Still Water at 200 rpm. (Barltrop, Varyani, Grant, Clelland, & Pham, 2007).

For a current velocity of 1.00 m/s together with a wave height of 0.15 m at a frequency of 0.50 Hz , the generated thrust increases by about 33 percent to an adjusted value of 443.2 kN . The results from the present study shows only a 20 percent increase in thrust from still water case to 0.609 m wave models.

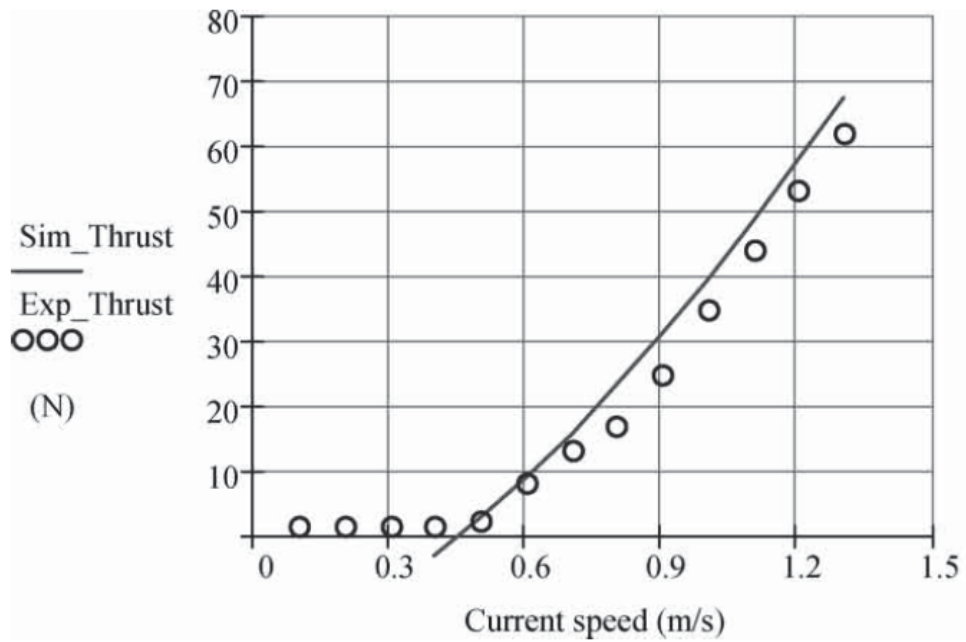


Figure 5.7 - Thrust vs. Current Velocity in $H=0.15\text{m}$, $f=0.50\text{Hz}$, at 150 rpm. (Barltrop, et al., 2007).

The plots of the thrust coefficient with respect to tip speed ratio follows the same trend as the theoretical curve. The still water plot shows a higher thrust coefficient than those for the wave cases for a TSR lower than 8.5. For the tip speed ratio greater than 8.5, the thrust coefficients are higher for the wave cases.

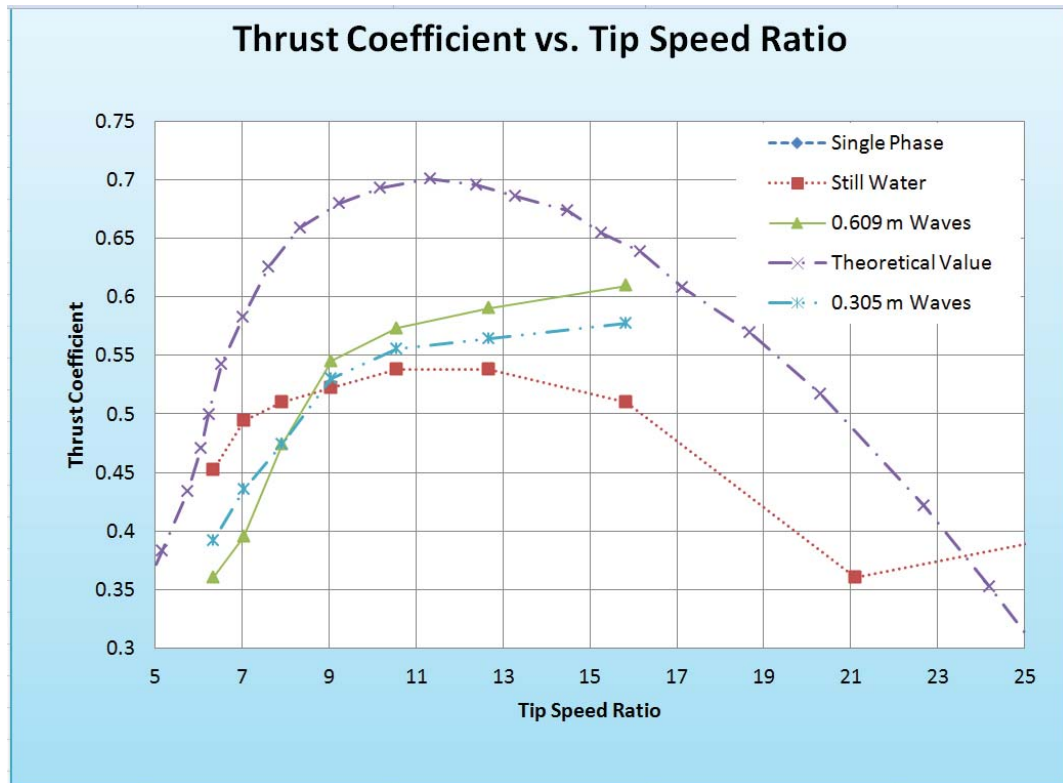


Figure 5.8 - Thrust Coefficient vs. Tip Speed Ratio comparing the Still Water Flow to Flow with Waves.

Figure 5.9 shows the thrust coefficient vs. TSR as reported in literature for a 0.70 m diameter turbine (Maganga, et al., 2009). The turbine is placed in a free surface circulation flume tank where it is tested under current velocities ranging from 0.6 to 1.5 m/s. The results from the present study are similar to the published data.

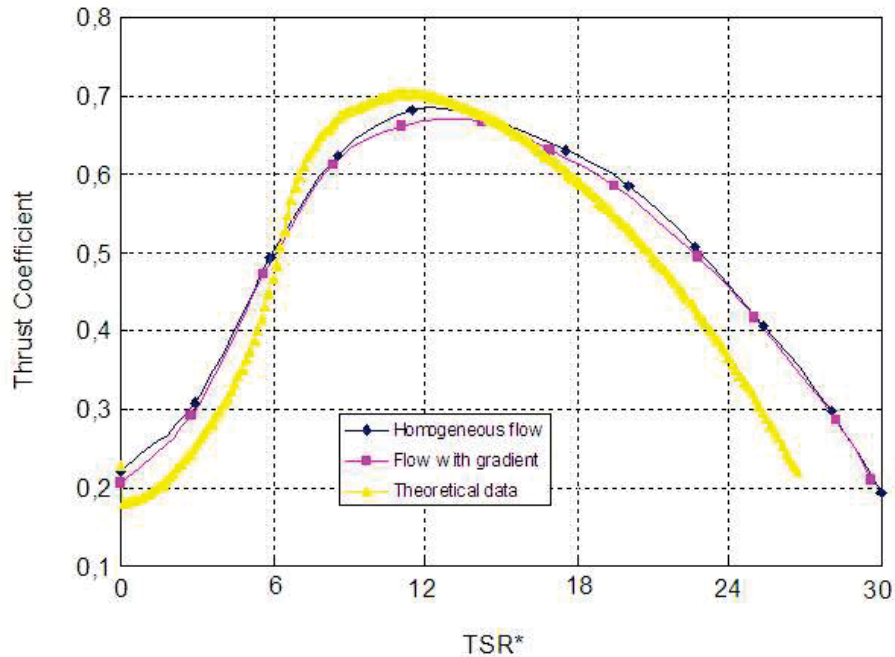


Figure 5.9- Thrust coefficient power moment. (Maganga, et al. , 2009).

5.4.2 Torque

The total torque on the rotor is taken as the resulting bending moment about the axis of rotation. The torque is computed from Equation 2.5.8, which relates the power coefficient and torque. Figure 5.10 shows the generated torque for the still water and wave models with respect to tip speed ratio. As the tip speed ratio increases, the torque decreases exponentially for each model. All three models show a decrease in torque following the same trend. An increase in tip speed ratio would correspond to a decrease in current velocity for a constant blade rotation. For these models, a comparison of torque with current velocity would be more meaningful, since the blade rpm is maintained constant at 7 rpm.

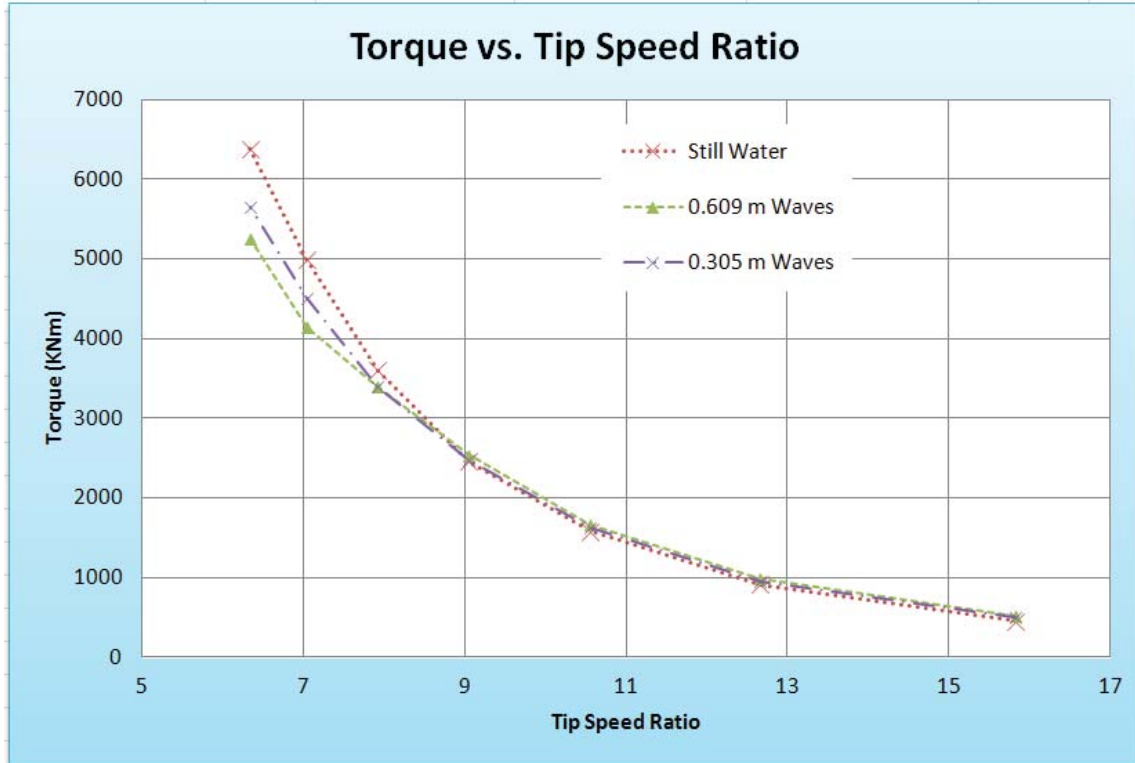


Figure 5.10 - Torque Generated vs. Tip Speed Ratio.

Figure 5.11 shows the torque vs. current velocity. As the current velocity increases, the torque also increases. Both wave plots follow the same trend as that for the still water case. It can be seen from Figure 5.3, that the rated torque is 740 kNm for a rotor diameter of 20 m at a current velocity of 2.3 m/s . The present study considers a rotor blade diameter of 43.2 m and the length scale factor, S_l is 0.46 . Using the principle of similitude, the torque for the rotor blade of 43.2 m is given by $Q_p = \frac{740}{S_l^3} = 7.46 \times 10^6 \text{ Nm}$. However; the generated torque in the present study is estimated to be $5.3 \times 10^6 \text{ Nm}$ Figure 5.11.

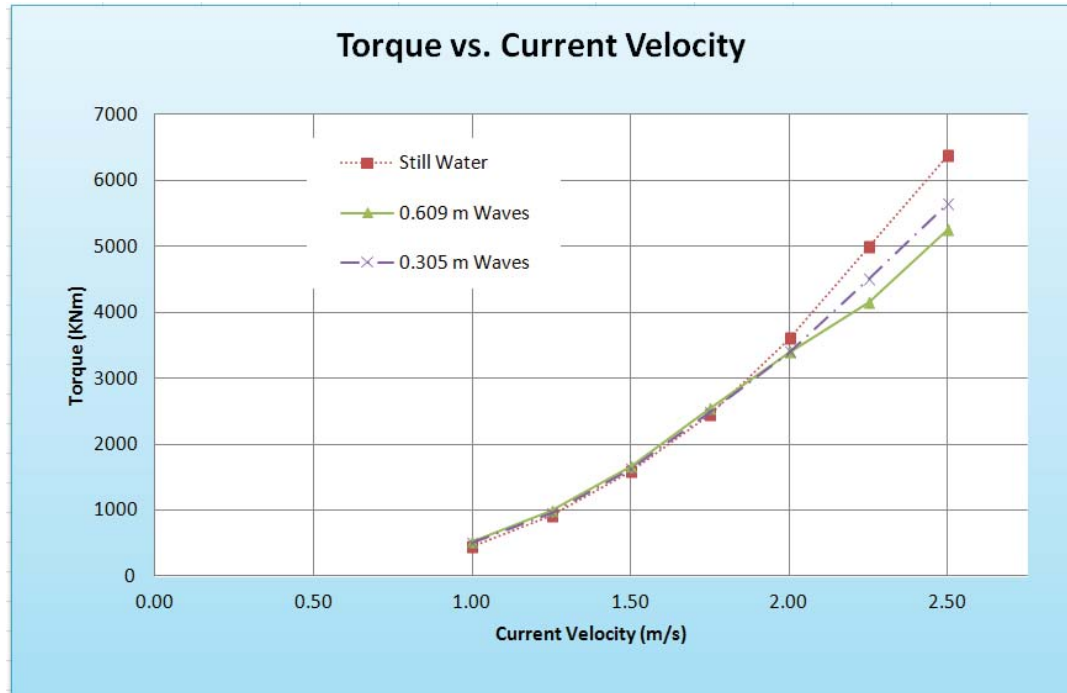


Figure 5.11 - Torque Generated vs. Current Velocity Comparing the Still Water Model to the Models with Waves.

The effect of change in wave height on the torque is shown in Figure 5.12. The results show that the torque remains nearly constant with increase in wave height. This trend is similar to that shown in Figure 5.13 reported by earlier researchers (Barltrop et. al. 2007).

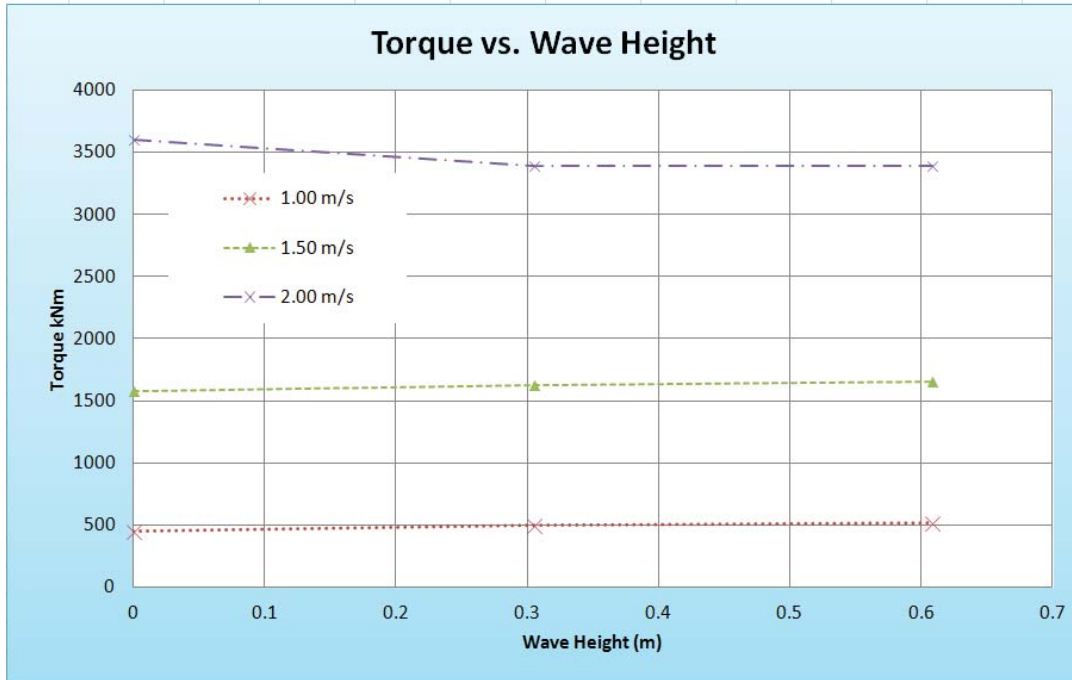


Figure 5.12- Torque vs. Wave Height.

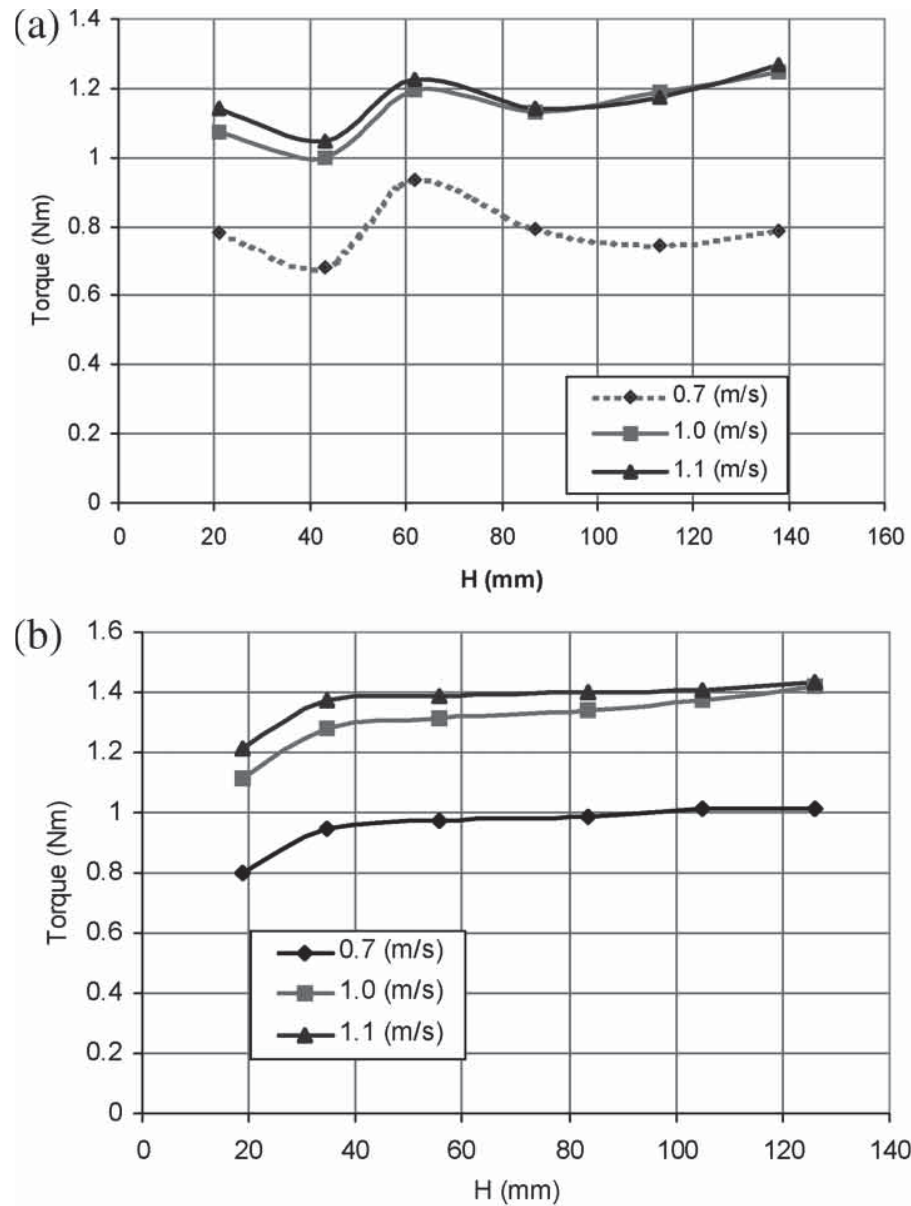


Figure 5.13 - Generated Torque based on Constant Frequency of (a) 0.625 Hz and (b) 0.833 Hz with Varying Wave Height. (Barltrop, et al., 2007).

5.4.3 Power

The power available from a stream of water can be computed from Equation 2.5.1. The rated power for a marine current turbine with a rotor diameter of 20 m and current velocity of 2.3 m/s can be read to be 885 kW (Figure 5.3). For the rotor diameter of 43.2 m used in the present study, the linear scale, S_l is 0.46 . The power generated from a rotor diameter of 43.2 m can be estimated using the principle of similitude to be 4.1 MW . This value compares reasonably well with 4.0 MW obtained from the present study shown in Figure 5.14.

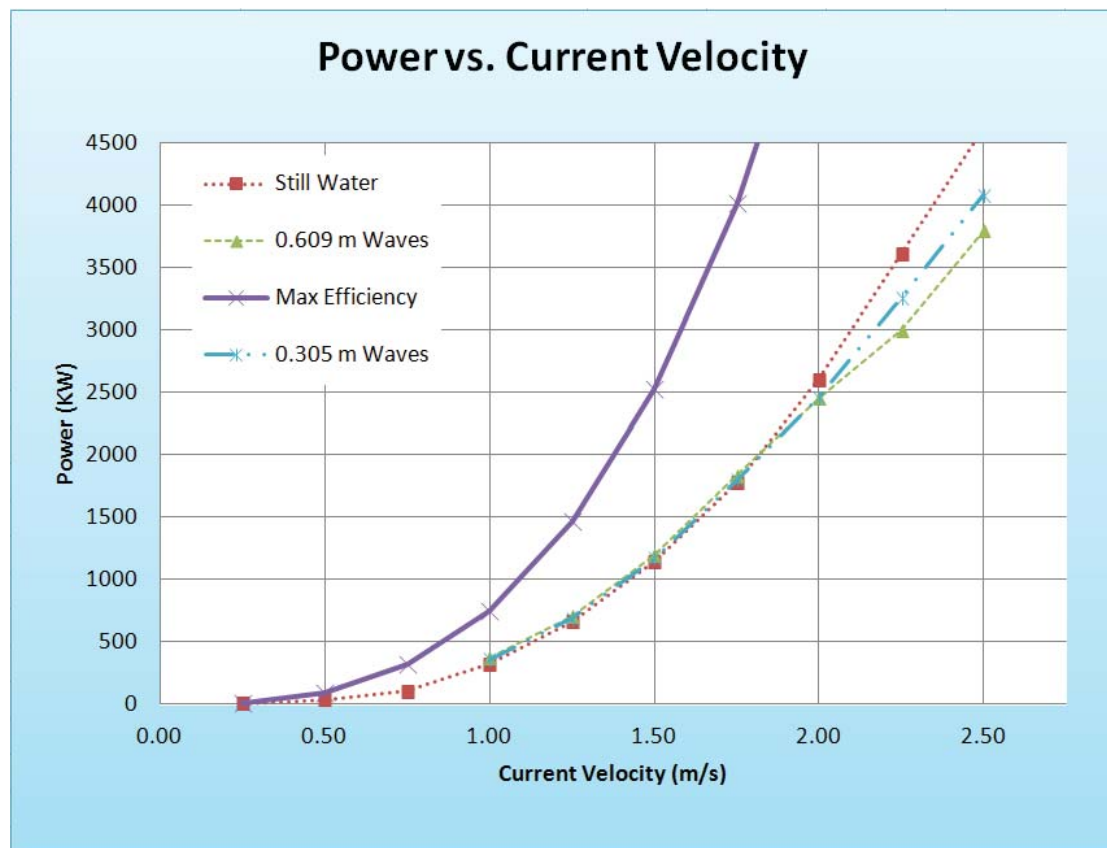


Figure 5.14 - Power vs. Current Velocity Comparing the Maximum Efficiency Values to the Current Model Data.

Table 5.1 shows that the generated power for the wave cases is higher than the still water plots at lower current velocities. The power generated from the still water case is higher than the wave cases at current velocities 2.00 m/s and higher.

Table 5.1- Generated Power vs. Current Velocity.

Current Velocity (m/s)	Generated Power kW		
	Still Water	0.305 m Waves	0.609 m Waves
1.00	325.1	357.3	371.3
1.25	661.4	686.1	709.0
1.50	1142.9	1171.7	1199.1
1.75	1773.9	1794.6	1834.7
2.00	2600.5	2454.4	2454.4
2.25	3612.3	3259.3	2999.4
2.50	4611.5	4083.5	3796.2

The “Maximum Efficiency” values are shown in Figure 5.15 for different tip speed ratios. It can be seen that the generated power decreases exponentially as the tip speed ratio increases. The results from the present study follow the same decrease in trend as the theoretical maximum values. The generated power for the wave plots are lower than those of the still water plot when the turbine is subjected to TSR less than 8.5. As TSR increases, the generated power for the wave plots is higher than that of the still water plot.

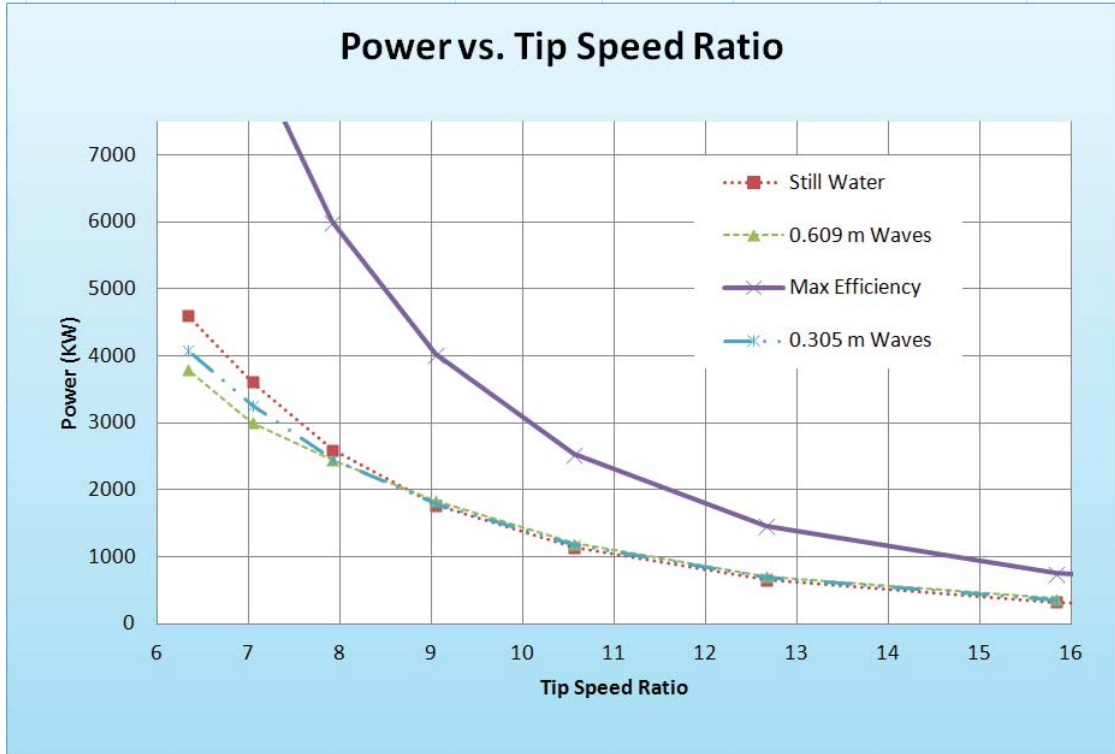


Figure 5.15- Power vs. Tip Speed Ratio showing Results from the Current Model and a Turbine of its Size at Maximum Efficiency.

Table 5.2 shows the lower power output values for the still water case for TSR from 9.0 to 15.8. However, the power output values for the still water case are higher than those for the wave cases for TSR of 6.3 and 7.

Table 5.2- Generated Power vs. TSR.

TSR	Generated Power kW		
	Still Water	0.305 m Waves	0.609 m Waves
15.8	325.1	357.3	371.3
12.7	661.4	686.1	709.0

10.6	1142.9	1171.7	1199.1
9.0	1773.9	1794.6	1834.7
7.9	2600.5	2454.4	2454.4
7.0	3612.3	3259.3	2999.4
6.3	4611.5	4083.5	3796.2

5.4.4 Power Coefficient

Power coefficients show the efficiency of the turbine. The results from the present study for all the three cases seem to follow the theoretical trend fairly closely as seen from Figure 5.16.

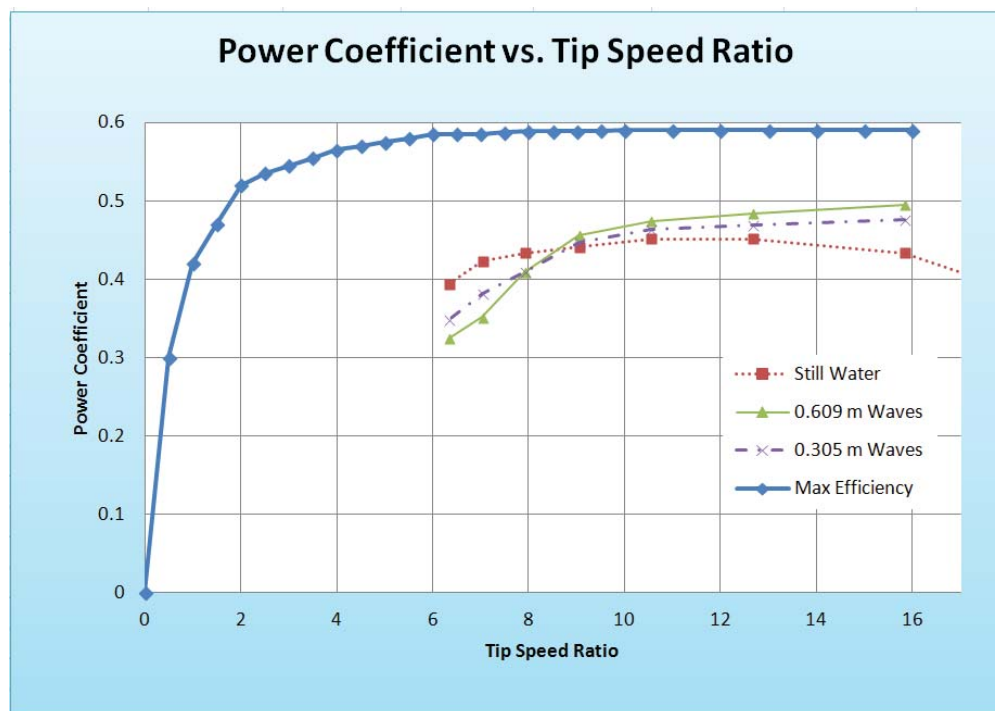


Figure 5.16- Power Coefficient vs. Tip Speed Ratio.

Previous work done by (Lee, et al., 2011) shows a comparison of CFD and experimental results for an 800 mm diameter turbine. The results from the present study show a similar trend to that shown in Figure 5.17. The maximum power coefficient of 0.47 from the CFD results in Figure 5.17 compares to a value of 0.43 in the present study for a TSR of 7.

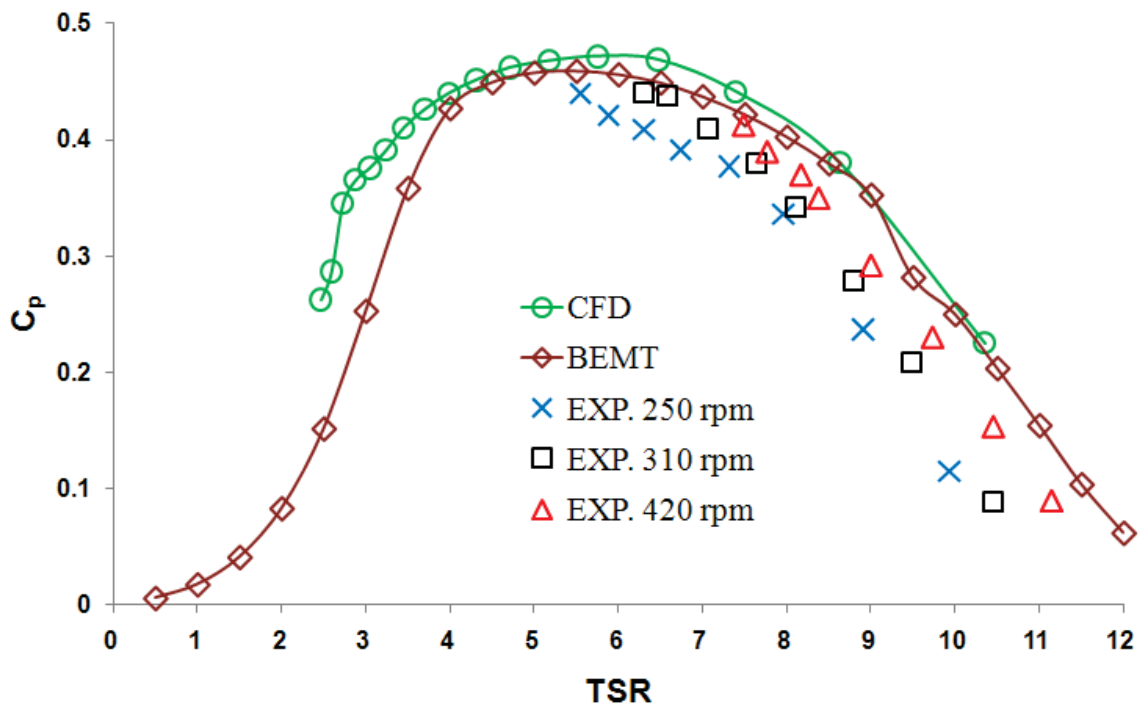


Figure 5.17 - Power Coefficient vs. Tip Speed Ratio. (Lee, et al., 2011).

Figure 5.18 shows the maximum efficiency for the power coefficient vs. tip speed ratio for a wind turbine and the *Betz* limit of 0.593. The results from the present study follow the maximum efficiency plot.

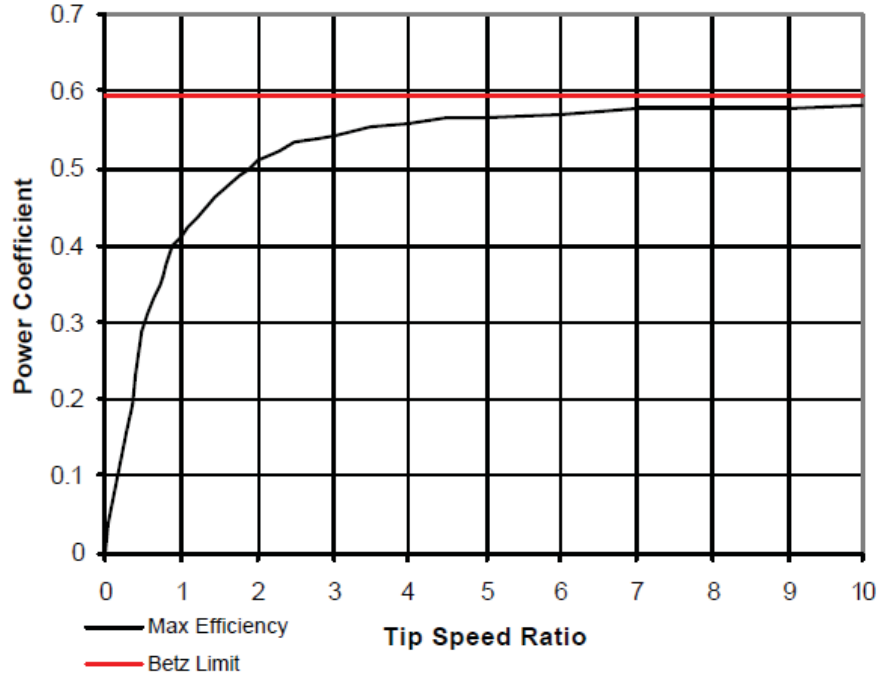


Figure 5.18 - Power Coefficient vs. Tip Speed Ratio. (Hartwanger & Horvat, 3D Modeling of a Wind Turbine Using CFD, 2008)

5.4.5 Cavitation

As a general rule of thumb, rotor speed should be limited to avoid significant cavitation (Fraenkel P. L., 2002). The rotor speed is limited as such to reduce the lift-drag ratio and hence improve the efficiency of the rotor. In a horizontal axis marine current turbine, cavitation occurs at the rotor blade tips where static pressure is least. As a result, blade tip velocity is limited to around $12-15\text{ m/s}$. In the present study the blade rotation is maintained at a constant value, resulting in a blade tip velocity of 15.8 m/s . A way to verify that cavitation is not present in the model is to observe the pressures. Cavitation occurs when the local negative pressure coefficient reaches the cavitation number. The cavitation number can be calculated from Eqn. 2.5.9. This number is compared with the

local pressure coefficient calculated from Eqn. 2.5.10. In the present study, for a current velocity of 2.0 m/s, the static water pressure at the propeller hub is calculated to be 250,891 Pa, the atmospheric pressure is taken to be 101,325 Pa, and the water vapor pressure at 70°F is estimated to be 29,039 Pa. The cavitation number is calculated to be 316 using Eqn. 2.5.9. The static pressure at the turbine interface and free stream static pressure are obtained from the ANSYS model to be 107,325 Pa and 110,825 Pa respectively. These pressures were used to calculate the coefficient of pressure from Eqn. 2.4.10. The pressure coefficient is found to be -3.4. According to (FRANC, 2006), cavitation occurs when the cavitation number is less than the negative of the pressure coefficient. Since the cavitation number, 316 is greater than the negative pressure coefficient of, -(-3.4), thus cavitation is not an issue in the present study.

CHAPTER 6

SUMMARY, CONCLUSIONS AND FUTURE WORK

6.1 Summary

- The mathematical simulation of wave-current interactions in marine current turbine (MCT) rotor blades is performed in the present study. The simulation considers multiphase flow involving open channel flow with wave boundary conditions.
- The present study uses a three dimensional rotor blade created in SolidWorks using cross-sectional data in the form of curves for the blade geometry. The rotor blade geometry is based on preliminary structural design information for composite blades reported by the National Renewable Energy Laboratory (NREL). The turbine has a total rotor diameter of 43.2 m .
- The computational domain is formed in ANSYS ICEM CFD based on a specific current velocity profile and the published data from (Reza, 2010) on the wake effects caused by the blade rotation. Based on this information, the extents of the domain are chosen to be 20 m before and 100 m after the plane of rotation. The domain and the 3D blade are meshed using tetrahedral volume meshing elements.
- The mesh in the blade and computational domain is refined by performing a grid independence study, adjusting the global scale factor to obtain different mesh

densities. Each successful mesh of the model is run to determine the effect on the wave-current interactions. The convergence study was carried out increasing the mesh elements from 650,000 to 2,000,000.

- The Euler-Euler approach is used in the present study, since it has the capability of modeling water flow in an open channel where the ratio of water present at the inlet to that at the outlet can be specified.
- The CFD model is run in ANSYS FLUENT V6 using the multiphase flow regime. Within the Multiphase Flow regime, the present study uses the Volume of Fluid (VOF) model to simulate open channel flow.
- The volume of fluid multiphase flow model is used to model open channel flow with wave boundary conditions. The pressure, velocity, and volume fraction from the CFD analyses are used in the calculation of the power, thrust, and torque for still water and wave cases.
- The results from multiphase flow models simulating still water and two different wave heights are presented along with discussions.
- The still water, *1ft (0.305 m)* wave height, and *2ft (0.609 m)* wave height cases are run in ANSYS FLUENT using the *Standard k- ω* turbulence model for a current velocity in the range of *1 m/s* to *2.5 m/s*. The effect of waves on the thrust, torque, power, are compared with those for the still water model.
- The results from ANSYS FLUENT in the present study are modified based on the principles of similitude and compared with those in the published literature.

6.2 Conclusions

- The present study establishes convergence of initial and final dynamic pressures and thrust with 1.5 million elements in the computational domain. As the current velocity and blade rotation increase, additional modeling would be necessary to establish the domain size.
- Based on the evaluation of the six different turbulence models, the Standard $k-\omega$ model is chosen and used in the present study because of the stability of the pressure and velocity variations upstream and downstream the turbine rotor plane.
- The current velocity distribution increases to a specific value past the plane of rotation decreasing to a steady state value at a distance of 100 m downstream. This distribution follows that given by the classical Actuator Disk Theory.
- At lower tip speed ratios, the turbine, when subjected to wave conditions, experience lower thrust than the still water case. At higher tip speed ratios, the turbine, when subjected to wave conditions, experience higher thrust than the still water case. The thrust variations seem to follow the theoretical maximum values for the still water and the two wave models. At higher current velocities, the thrust values appear to be increasing at a faster rate.
- The thrust coefficient vs the tip speed ratio follows the same trend as the theoretical curve. The thrust coefficients for the still water case are higher than those for the wave cases for TSR lower than 8.5. However, the thrust coefficients for the wave cases are higher than those of the still water case for TSR greater

than 8.5. The results from the present study follow the general trend observed in the published data.

- The torque decreases exponentially with increases in the tip speed ratio for all the three cases. The torque increases with increases in the current velocity. It is observed that the torque remains nearly constant with increase in wave height, and the trend is similar to that reported by earlier researchers.
- The generated power for the wave cases is higher than that for the still water case at lower current velocities, but the power generated from the still water case is higher than those for the wave cases at current velocities of 2.00 m/s and higher.
- The power coefficients from the present study for all the three cases follow the theoretical trend closely.
- For a typical case in the present study, the cavitation number is significantly less than the negative pressure coefficient, thus indicating the absence of cavitation in the rotor blade chosen.

6.3 Future Work

- Further studies on the effects of cavitation in the wave current interactions in marine current turbines can be simulated using ANSYS FLUENT. ANSYS FLUENT has the capability of cavitation modeling based on the *Singhal-et-al Cavitation Model*.
- Parametric studies can be extended to include larger computational domains outside the swept area of the rotor blades.

- The effect of wave frequencies on the torque in a marine current turbine need be simulated.

REFERENCES

- ANSYS, Inc. (2007). *ANSYS ICEM CFD 11.0 Tutorial Manual*. ANSYS, Inc.
- ANSYS, Inc. (2010). *ANSYS FLUENT Theory Guide*. ANSYS, Inc.
- ANSYS, Inc. Proprietary. (2009). *Introduction to CFD*. ANSYS, Inc.
- Assis, A. (2004). The Principle of Physical Properties. *Annales de la Fondation Louis de Broglie*, Volume 29 no 1-2.
- Bartrop, N., Varyani, K. S., Grant, A., Clelland, D., & Pham, X. P. (2006). Investigation into wave-current interactions in marine current turbines. *J. Power and Energy*, 233-242.
- Bartrop, N., Varyani, K. S., Grant, A., Clelland, D., & Pham, X. P. (2007). Investigation into wave-current interactions in marine current turbines. *J. Power and Energy*, 233-242.
- Bergman, J. (2001, August). *Water(The Hydrosphere)*. Retrieved May 2011, from Windows To The Universe:
<http://www.windows2universe.org/earth/Water/density.html>
- Bir, G., & Migliore, P. (2004). *Preliminary Structural Design of Composite Blades for Two- and Three-Blade Rotors*. Golden, Colorado.: National Renewable Energy Laboratory.

Cebeci, T., Shao, J. P., Kafyeke, F., & Laurendeau, E. (2006). *Computational Fluid Dynamics for Engineers*. Long Beach : Springer.

Driscoll, F. R., Alsenas, G. M., Beaujean, P. P., Ravenna, S., Raveling, J., Busold, E., & Slezycski, C. (2009). *A 20KW Open Ocean Current Test Turbine*. Dania Beach: Center for Ocean Energy Technology.

Engineering Toolbox. (2011). Retrieved 2011, from Engineering Toolbox:
www.engineeringtoolbox.com

Fraenkel, P. L. (2002). Power from marine currents. *Proc Instn Mech Engrs Vol 216 Part A: J Power and Energy*.

Fraenkel, P. L. (2002). Power from Marine Currents. *Proc Instn Mech Engrs Vol 216 Part A: J Power and Energy* (pp. 1-14). London: IMechE.

Fraenkel, P. P. (2004). *Marine Current Turbines: an emerging technology*. Glasgow.

FRANC, J.-P. (2006). Physics and COntrol of Cavitation. *Design and Analysis of High Speed Pumps*, 2-1 - 2-36.

Garber, S. (2009, August). *US Centinnial of Flight Comission* . Retrieved May 2011, from NASA:
<http://www.centennialofflight.gov/essay/Dictionary/Compressibility/DI136.htm>

Harris, H. G., & Sabnis, G. M. (1999). *Structural Modeling and Experimental Techniques*. Boca Raton: CRC Press LLC.

- Harrison, M. E., Batten, W. M., Myers, L. E., & Bahaj, A. S. (2009). A comparison between CFD simulations and experiments for predicting the far wake of horizontal axis tidal turbines. *Proceedings of the 8th European Wave and Tidal Energy Conference* (pp. 566-575). Uppsala: Sustainable Energy Research Group.
- Hartwanger, D., & Horvat, A. (2008). 3D Modelling of a Wind Turbine Using CFD. *NAFENS Conference*. United Kingdom.
- Hartwanger, D., & Horvat, D. A. (2008). 3D Modeling of a Wind Turbine Using CFD. *NAFEMS Conference*, (pp. 1-14). United Kingdom.
- Kalkert, C., & Kayser, J. (2006). *Laser Doppler Velocimetry*. San Diego: PHYS173 Biophysics Laboratory.
- Lee, H. J., Kim, H. D., Rhee, H. S., Do, I. R., Shin, B. C., & Kim, M. C. (2011). Computational and Experimental Analysis for Horizontal Axis Marine Current Turbine Design. *Second International Symposium on Marine Propulsors smp'11*. Hamburg.
- Leland, A. E. (2009). *A Resource Assesment of Southeast Florida as related to Ocean Thermal Energy*. Boca Raton: Florida Atlantic University.
- Logan, D. L. (2007). *A First Course in Finite Element Method*. Canada: Cengage Learning.
- Maganga, F., Germain, G., King, J., Pinon, G., & Rivoalen, E. (2009). Experimental study to determine flow characteristic effects on marine current turbine behavior.

8th European Wave and Tidal Energy Conference (pp. 661-667). Uppsala, Sweden: Hydrodynamic & Metaocean Service, IFREMER - French Research Institute for Exploitation of the Sea,; University of Bristol,; Laboratoire Ondes et Milieux Complexes, FRE 3102 CNRS.

Maganga, F., Germain, G., King, J., Pinon, G., & Rivoalen, E. (2009). *Experimental Study to Determine the Flow Characteristic Effects on Marine Current Turbine Behaviour*. Uppsala: Proceedings of the 8th European Wave and Tidal Energy Conference.

Migliore, G. B. (2004). *Preliminary Structural Design of Composite Blades for Two- and Three-Blade Rotors*. Battelle: National Renewable Energy Laboratory.

Morrison, F. A. (2004). Associate Professor of Chemical Engineering. In M. T. University, *Compressible Fluids* (pp. 94-98). Michigan.

Nakayama, Y. (. (1999). *Introduction to Fluid Mechanics*. New York: J. Wiley & Sons.

Reza, Z. (2010). *Dissipation and Eddy Mixing associated with flow past an Underwater Turbine*. Boca Raton: Florida Atlantic University.

Singh, A. J., & Arockiasamy, D. M. (2011). MATHEMATICAL MODELING AND NUMERICAL SIMULATION OF FLUID FLOW EFFECTS ON MARINE CURRENT TURBINES. *Proceedings of the ASME 2011 30th International Conference on Ocean, Offshore and Arctic Engineering*. Rotterdam: OMAE2011.

U.S. Department of the Interior. (2006). *Technology White Paper on Ocean Current Energy Potential on the U.S. Outer Continental Shelf*. Minerals Management Service; Renewable Energy and Alternate Use Program.

Winterstein, S. R., Fitzwater, L. M., Manuel, L., & Veers, P. S. (2001). *Moment-based fatigue load models for wind energy systems*. Sandia National Laboratories U.S.: Swets & Zeitlinger.